Methods for High-Contrast Photoluminescence and Label-Free Surface-Sensitive Detection

Dissertation

der Mathematisch-Naturwissenschaftlichen Fakultät
der Eberhard Karls Universität Tübingen
zur Erlangung des Grades eines
Doktors der Naturwissenschaften
(Dr. rer. nat.)

vorgelegt von
M.Sc. Viktoria Wedler
aus Herrenberg

Tübingen
2022

Gedruckt mit Genehmigung der Mathematisch-Naturwissenschaftlichen Fakultät der Eberhard Karls Universität Tübingen.

Tag der mündlichen Qualifikation:	10.11.2022
Dekan:	Prof. Dr. Thilo Stehle
1. Berichterstatter/-in:	Prof. Dr. Erik Schäffer
2. Berichterstatter/-in:	Prof. Dr. Monika Fleischer

Zusammenfassung

Physikalische Phänomene wie Totalreflexion, Streuung und Interferenz oder Plasmonenresonanzen ermöglichen oberflächensensitive analytische Methoden. Diese Methoden zeichnen sich durch sehr hohe Sensitivitäten aus, welche die Detektion von einzelnen Molekülen – z.B. Proteinen – ermöglichen. Ein Beispiel für Proteine sind Kinesine. Kinesine sind relevant für viele wichtige biologische Prozesse, eingeschlossen Zellteilung und dem zellulären Transport und bewegen sich entlang von Mikrotubuli-Filamenten. Um einzelne Kinesine untersuchen zu können, werden sie typischerweise mit Fluoreszenzfarbstoffen markiert und über Interne Totalreflexionsfluoreszenzmikroskopie visualisiert. Um die Interaktion von Kinesinen mit Mikrotubuli in ihrem nativen Zustand untersuchen zu können, wird eine Marker-freie Detektion benötigt. Da Kinesine sehr große Moleküle sind, ist es wahrscheinlich, dass unmarkierte Kinesine mittels optimierter Interferenzreflexionsmikroskopie (IRM) oder Interferenzstreumikroskopie (iSCAT) detektiert werden können. Möglicherweise können unmarkierte Kinesine alternativ über das hochsensitive, plasmonische Nahfeld detektiert werden. Alle oberflächensensitiven Detektionsmethoden sind jedoch über die Qualität ihrer Oberflächen limitiert. Gerade bei biologischen Experimenten sind die Proben komplex und nicht lange haltbar. Daher müssen hochqualitativ funktionalisierte Proben sehr häufig und reproduzierbar hergestellt werden. Dafür habe ich eine Methode entwickelt, welche hochqualitative Oberflächen reproduzierbar mit minimalem Arbeitsaufwand ermöglicht. Mit dem neuen Protokoll können molekular saubere Oberflächen zuverlässig funktionalisiert und für Mikrofluidikkanäle eingesetzt werden. Diese Proben zeichnen sich durch minimierte Hintergrundsignale und ihre Eignung für Einzelmolekülmessungen aus. Außerdem habe ich für eine zukünftige, Marker-freie Kinesindetektion ein Program geschrieben, welches ermöglicht IRM und iSCAT-Mikroskopie parallel durchzuführen. Dadurch wird aus der ursprünglichen Bildnachbearbeitungsmethode iSCAT eine Echtzeitanwendung. Desweiteren habe ich eine Methode entwickelt, die es ermöglich plasmonische Goldnanoantennen an Mikrotubuli zu binden, ohne dabei das sensitive plasmonische Nahfeld zu blockieren. Messungen zeigten, dass die plasmonischen Nanoantennen als multifunktionale Mikrotubuli-Marker verwendet werden können, die weder blinken noch bleichen. In Zukunft und mit verbesserten Oberflächenfunktionalisierungen und Marker-freien Techniken können Mikrotubuli-gebundene plasmonische Nanoantennen möglicherweise als ultrasensitive Einzelmolekülsensoren genutzt werden, die einzelne Kinesine im Vorbeilaufen detektieren.

Abstract

Physical phenomena such as total internal reflection, scattering and interference, or plasmon resonances enable surface-sensitive detection methods. These methods have high sensitivities that allow the detection of single nanoparticles or single molecules such as proteins. Proteins have interesting physiological functions. One example are kinesins that are a key to essential biological processes such as cell division and cellular transport. Kinesins are motor proteins that move along microtubule "tracks". To study single kinesins, they are conventionally labeled with fluorescent dyes and detected using total internal reflection fluorescence (TIRF) microscopy. However, to improve the understanding of their native interaction with microtubules, a label-free detection is desirable. Due to the large size of the kinesin molecule, label-free detection can be envisioned by optimized interference reflection or interferometric scattering microscopy (IRM and iSCAT). Alternatively, unlabeled kinesins could potentially be detected using the highly sensitive near-field of plasmonic nanoparticles. One limiting factor of all surface-sensitive detection techniques is the requirement of a high quality surface. Especially for biological samples, the assays become complex while exhibiting a short storage life. Therefore, well functionalized surfaces must be prepared frequently. Here, I developed a method to generate reproducibly high quality surfaces for high contrast imaging of microtubules and kinesins with a minimized work effort. With the new protocol, molecularly clean surfaces are obtained that are reliably functionalized and yield low-background microfluidic chambers suited for all further measurements. To enable label-free detection of kinesins in the future, I wrote an image acquisition and analysis program that allows real-time iSCAT imaging with simultaneous IRM detection. Additionally, I developed a method that enabled the binding of gold nanorods to microtubules, without blocking their highly sensitive plasmonic near-field. Measurements suggested that these functionalized plasmonic nanoantennas could serve as multipurpose bleach and blink-free *in vitro* microtubule markers. In the future, with improved surface preparations and label-free techniques, microtubule-bound plasmonic antennas potentially can be used as ultrasensitive single-molecule sensors for molecular machines translocating along microtubules.

Contents

1. Low background microfluidic chambers for high contrast imaging of microtubules and kinesins

1.1. Introduction

The interaction of kinesins with microtubules is highly relevant in biological processes such as cell division and cellular transport [1]. Microtubule-kinesin assays gained popularity in the 1980s with the first single kinesin assay published in 1989 [2–4]. From then until today, a broad variety of assays optimized for single kinesin-microtubule interactions were published showing that there is still an ongoing need for improvement. In general, all types of assays have the same goal: offering ideal imaging and analysis conditions of undisturbed specific interactions between kinesins and microtubules [5–10]. The interaction of kinesin and/or dynein with microtubules can be assessed in either gliding or stepping assays. Gliding assays focus more on the kinesin-driven movement of the microtubule and stepping assays display the mobile kinesins walking along immobilized microtubules [11–14]. In stepping assays, the rigid fixation of microtubules is of importance for an optimal resolution and to avoid artefacts when measuring the kinesin movements [5]. Especially to observe the movement of single kinesin molecules, unspecific interactions between kinesins and the surface and the presence of contaminations need to be minimized [7]. Imaging methods suited for kinesin-microtubule assays are typically very surface-sensitive—such as IRM and TIRF microscopy. Thus the respective surfaces must be of high quality with a minimal amount of contamination and should offer a high signal-to-background ratio (SBR). Typically, surface modification approaches for stepping assays consist of multiple steps and often comprise a modification of the glass surface, the adsorption of different macromolecules for blocking and/or microtubule attachment and sometimes even a further modification of the absorbed macro molecules [5–10, 15]. An assay that has been successfully performed for many years by various researchers around the world is based on a hydrophobic surface, that interacts with microtubule-binding antibodies and the hydrophobic middle part of a blocking agent [15, 16]. To perform this assay, glass surfaces are rendered hydrophobic by spin coating with a hydrophobic polymer or a covalent attachment of hydrophobic surface groups via silanization [15, 17, 18]. While the assay itself has been proven to be functional and reliable, the challenge of this approach occurs with the difficulty to obtain high quality hydrophobic surfaces [6]. Even though silanization of glass surfaces has been used for decades, issues with reproducibility are still addressed repeatedly [6,19–21]. Reproducible surface functionalizations are often achieved by using

silanes that polymerize in the presence of humidity [5]. However, during single-molecule measurements performed in close surface proximity, polymers can potentially interfere with the measurements and are therefore undesirable. Uncontrolled polymerization can be prevented by working under complete humidity exclusion [19, 21] requiring an extensive work effort and equipment rare in typical biology-based laboratories. On the contrary, the usage of monoreactive, non-polymerizing silanes prevents polymer formation but generates unreactive dimers when used in ambient air [22,23]. In 2018, a simple and reproducible silanization protocol performed under ambient air was reported which uses the monoreactive silane trimethylchlorosilane and is suited for microtubule-kinesin assays [6]. However, this protocol used a catalyst during a solvent-based silanization procedure. Solvent-based silanizations, as well as cleaning procedures, were experienced as work intensive, waste-producing, and most importantly, prone to catch contamination in the available laboratory environment. For the preservation of molecularly clean high quality surfaces, vapour phase silanization is expected to be more suited. Molecularly clean and high quality surfaces suited for single-molecule measurements can be reliably achieved by chemical etching or plasma cleaning [5, 24, 25]. Additionally, aqueous chemical treatments and plasma cleaning were reported to improve silanization efficiencies by surface hydroxylation [26–30]. In this chapter, an improved, simple, quick and reproducible silanization protocol to achieve high quality surfaces suited for hydrophobicity-based microtubule-kinesin single-molecule assays was developed. Therefore, glass surfaces were treated with different chemical or plasma cleaning procedures and functionalized with different silanes rendering hydrophobic groups. Then, the water contact angles of the resulting surfaces were measured. Furthermore, an unconventional but effective plasma activation procedure was discovered and the resulting surface was analyzed using x-ray photoelectron spectroscopy (XPS). Then, the functionality of the assay on the surfaces prepared with the new protocol was confirmed. The resulting surfaces were used to systematically investigate the "degree of hydrophobicity" required for a high quality functional assay in TIRF. Finally, to assess whether the IRM contrast could be improved by the choice of the assay, I investigated the IRM SBR of microtubules fixed at different heights from the surface.

1.2. Theoretical Background

This section briefly explains the theoretical background required for the understanding of this chapter.

1.2.1. Silicon-based materials and chemicals

The most important silicon-based materials and chemicals that were used in this chapter (and thesis) are listed below:

Silicon Silicon (Si) is the 14^{th} element of the periodic table. Silicon is a tetravalent metalloid and can form by chemical reaction the materials mentioned below [31].

Silicon dioxide and silica A very common oxidized form of silicon is silicon dioxide (SiO_2). The term SiO_2 names either the molecule only consisting of one Si and two oxygen atoms or any material that consists of the same ratio of silicon and oxygen. Silica names any material consisting of silicon dioxide. It exists in a pure crystal form (e.g. naturally occurring rock crystal) but it also can be amorphous as silica gel, silica glass or silica colloids [31–33].

Glass While the term glass stands for a non-crystalline solid, it often refers to amorphous silica-based materials. In multi component silica glasses, some Si atoms are substituted with alkali or alkaline earth elements such as boron. Due to different valences (tetrahedral silicon vs trihedral boron), the crystal structure changes. Thus, the structure of the glass is rather viewed in terms of small structural units such as boron oxide and silicates. Therefore, a silica based glass will be called e.g. borosilicate glass if there are boron substitutes in it. Typically the silica content of commercial borosilicate glasses can vary from 50% (for substrates) to 80% (for lab ware) [34].

Silicic acids and silicates Silicate anions are the conjugate bases of silicic acids. Silicates can occur in different structures / Si-O ratios, e.g. the nesosilicate SiO_4^-. Silicic acids and silica can be used to synthesize silica such as silica gels or spheres [31].

Silanes The term silanes refers to organosilicon derivatives of the molecule silane (SiH_4). Subclasses of silanes are siloxanes ($R_3Si\text{-}O\text{-}SiR_3$), silazanes ($R_3Si\text{-}N\text{-}SiR_3$), chlorosilanes ($R_xSiCl_y$) and alkoxysilanes ($R_xSiO[CH_2]_yCH_3]$) with R being organic residues and x and y being indices. [35, 36]

Silicone Silicones are polymeric materials that are based on a siloxane backbone and can be synthesized using e.g. silanes [37, 38].

1.2.2. Glass surface modifications

To plan glass surface modifications, it is important to understand the nature and behaviour of glass surfaces. In this context, glass surfaces are usually simplified in the literature as silica surfaces.

1.2.2.1. Cleaning processes

To modify a silica glass surface, it must be exposed. Even the originally cleanest glass surface will be contaminated quickly (e.g. total volatile organic compound concentration of room air: $\approx 1.1\,\mathrm{mg}$ per m^3) by the ambient air and must be cleaned freshly to expose the silica surface for functionalization [39].

Simple sonication and washing Solvent and soap based washing is expected to remove organic contamination and particles by the aid of sonication. The exposure to solvents like ethanol and soap is not expected to have any effect on the surface properties besides

cleaning. In contrast, sonication has been reported to generate radicals and modify surface properties [40–42].

Chemical etching In contrast to mild but limited sonication and solvent based procedures, chemical etching processes quickly decompose high amounts of contaminants and also etch the glass surface. A relatively harmless chemical etching process (compared to hydrofluoric acid or piranha solution) is the potassium hydroxide (KOH)-hydrogenperoxide (H_2O_2) etching process. In this process, the strong oxidant hydrogen peroxide is mixed with an aqueous KOH solution such that the hydrogen peroxides conjugate base, the hydroperoxide anion forms:

$$H_2O_2 + OH^- + K^+ \rightleftharpoons HO_2^- + H_2O + K^+ \tag{1.1}$$

This anion is considered to be a weak oxidant and a weak reductant but a strong nucleophile which attacks contaminants that have electron deficient functional groups [43,44]. KOH-H_2O_2 etching was shown to efficiently remove organic material [45]. At the same time, KOH is silicon and silicon dioxide corrosive and etches the glass surface which involves hydration, hydroxylation and hydrolyzation [46, 47].

Plasma cleaning A user and environmentally friendly alternative cleaning process is plasma cleaning [48, 49]. During plasma cleaning, a gas or gas mixture becomes ionized and decomposes, together with its residual free electrons, materials under a vacuum atmosphere [50]. For instance, carbohydrates can be removed efficiently with oxygen plasma. The plasma-generated reactive oxygen species decompose carbohydrates and form CO_2, CO and H_2O which will be removed by the applied vacuum [51]. In addition to the cleaning process, the surface properties are changed physically and chemically, e.g. the surface groups of the substrate are changed [26, 52, 53].

1.2.2.2. Hydration & hydroxylation

The ratio of siloxane and silanol groups determines the reactivity of a silica surface, as only silanol groups are reactive towards silanes. The increase of the amount of present silanol groups is called hydroxylation [54]. The processes of hydroxylation and dehydroxylation are schematically described by the Zhuravlev model (Fig. 1.1) [30]:
a fully dehydrated and dehydroxylated glass surface (Fig. 1.1A) can become fully hydroxylated (Figure 1.1B-D) upon immersion at 100 °C in water (Arrow 1). The thereby generated surface OH-groups bind to water molecules via hydrogen bonds and even a surface appearing "dry" by eye will be covered by multilayers of water (Fig. 1.1B) [31,34]. These multilayers can be reduced to a water monolayer (Fig. 1.1C) by exposure to vacuum at room temperature (25°C, Arrow 2). Upon exposure to ambient air (Arrow 3), a multilayer of water builds up, again. To fully remove all adsorbed water, a heating of the surface to $T > 190\,°C$ under vacuum (Arrow 4) is required. Even at these temperatures, the hydroxy groups remain intact. To fully dehydroxylate the surface (Arrow

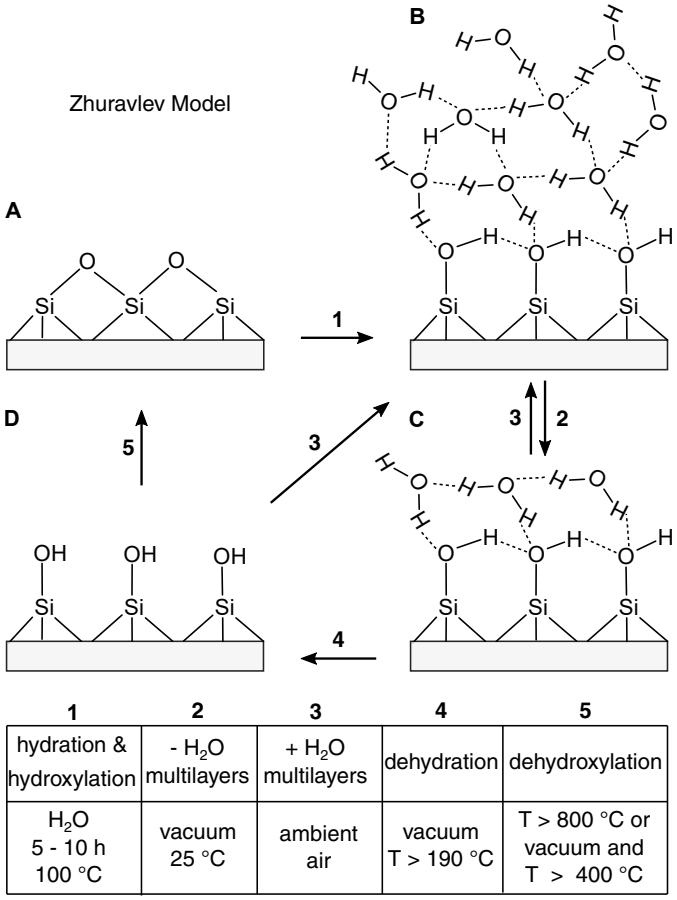

1	2	3	4	5
hydration & hydroxylation	- H_2O multilayers	+ H_2O multilayers	dehydration	dehydroxylation
H_2O 5 - 10 h 100 °C	vacuum 25 °C	ambient air	vacuum T > 190 °C	T > 800 °C or vacuum and T > 400 °C

Figure 1.1.: Zhuravlev model [30]: a dehydrated and dehydroxylated surface (**A**) can be hydrated and hydroxylated by heating in water (Arrow 1). The resulting water multilayer (**B**) can be reduced to a monolayer by exposure to vacuum (Arrow 2 and **C**). A completely dehydrated hydroxylated surface (**D**) can be achieved by heating the surface (Arrow 4). Exposure to ambient air (Arrow 3) allows the build-up of multilayers of adsorbed water. The surface can be dehydroxylated by extensive heating and/or vacuum (Arrow 5). Details on the procedures are listed in the table at the bottom of the figure.

5), temperatures higher than $T > 800\,°C$ are required, or if performed additionally under vacuum, temperatures above 400 °C are sufficient. Therefore, hydroxy groups are rather stable. However, a fully hydroxylated surface (4.6 hydroxy groups per nm^2 for an amorphous silica surface [30, 31, 55]) without adsorbed water layers (Fig. 1.1D) can only be maintained in vacuum, as exposure to ambient air allows the built-up of water multilayers [30, 31].

1.2.2.3. Silanization

A very common approach to modify glass surface properties is the covalent binding of silanes to the surface-silanol-groups rendering the desired surface properties to the substrate. This modification has the advantage over other non-covalent methods that long term storage and chemical stability is reached. The silanes that were used within this work can be divided into three basic subgroups that will be introduced briefly within the next paragraphs.

Chlorosilanes (Mono-) chlorosilanes have three organic residues (R) and one reactive chlorine group (Cl). When a chlorosilane encounters a surface silanol, HCl will be formed and the silane will form a siloxane bond with the surface [22]:

$$R_3SiCl + \equiv SiOH \longrightarrow \equiv SiOSiR_3 + HCl \tag{1.2}$$

Alternatively, the chlorosilane can encounter an adsorbed water molecule and hydrolyse into a silanol molecule, again under the generation of HCl [23]:

$$R_3SiCl + H_2O \longrightarrow R_3SiOH + HCl \tag{1.3}$$

Such molecular silanol can condensate with the surface silanols to form a stable siloxane bond and functionalize the surface [56, 57]:

$$R_3SiOH + \equiv SiOH \longrightarrow \equiv SiOSiR_3 + H_2O \tag{1.4}$$

However, the above described reactions do not only apply to reactions between silanes and surface silanols but also to reactions between the silane molecules themselves. Thus, as soon as molecular silanol is generated, unwanted dimerizations between two molecular silanol molecules or between a molecular silanol and a chlorosilane can occur.

Silazanes can carry the same organic residues (R) as chlorosilanes and generate in principal the same type of surface (Figure 1.2). However, the reaction mechanism is slightly different and involves the decomposition of the disilazane. When encountering a surface silanol, one silyl group will form a stable siloxane bond with the surface while the other groups form an aminosilane [58]:

$$(R_3Si)_2NH + \equiv SiOH \longrightarrow \equiv SiOSiR_3 + R_3SiNH_2 \tag{1.5}$$

In a second step, this aminosilane reacts with another surface silanol under generation of ammonia (NH_3) [58]:

$$R_3SiNH_2 + \equiv SiOH \longrightarrow \equiv SiOSiR_3 + NH_3 \tag{1.6}$$

Alternatively, two aminosilanes can dimerize back into a silazane and start the reaction all over again [58]:

$$2\,R_3SiNH_2 \longrightarrow (R_3Si)_2NH + NH_3 \tag{1.7}$$

Additionally, silazanes can hydrolyse when they encounter adsorbed water. Upon hydrolysis, the silazane decomposes into one molecular silanol and one aminosilane [58]:

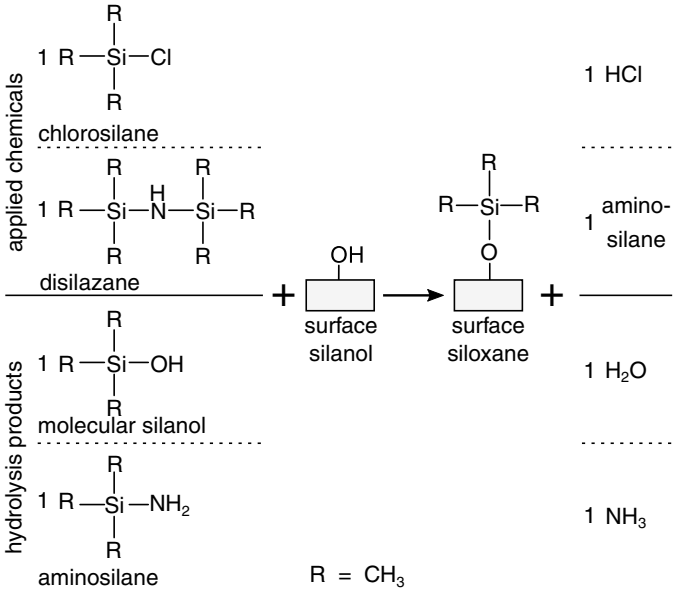

Figure 1.2.: Chlorosilanes, disilazanes and their hydrolysis products molecular silanol and aminosilane can react with surface silanols. When carrying the same residue R (here R=CH_3), all four molecules react under the formation of the same surface siloxane but with different byproducts (HCl, aminosilane, H_2O and NH_3).

$$(R_3Si)_2NH + H_2O \longrightarrow R_3SiOH + R_3SiNH_2 \tag{1.8}$$

These aminosilanes and molecular silanols can react with a surface as described earlier in the text. Overall, chlorosilanes and disilazanes undergo different chemical reactions but the resulting monolayer at the surface is chemically identical. Figure 1.2 summarizes how the applied chemicals chlorosilane and disilazane as well as their potential hydrolysis products (molecular silanol and aminosilane) can react with a surface silanol under the generation of identical surface siloxanes but with different byproducts (HCl, aminosilane, H_2O and NH_3).

Triethoxysilanes (TES) Similar to the above described reactions, TES can directly react with surface silanols under the generation of surface siloxanes and ethanol (Fig. 1.3A, horizontal reaction). Small amounts of water are necessary to replace the remaining ethoxy groups of the surface siloxanes with hydroxy groups to further condensate into fully cross-linked siloxane backbones (Fig. 1.3 right column, vertical reaction).
However, when water is present during the reaction, the ethoxy groups of yet unreacted TES molecules can be replaced with hydroxy groups as well (Fig. 1.3 vertical reaction from A to B). Nevertheless, the resulting molecular silanols can react with the surface silanols to form surface siloxanes (Fig. 1.3B, horizontal reaction). These surface siloxanes can further continue to condensate into the desired fully cross-linked siloxane backbones (Fig. 1.3 right column, vertical reaction). Alternatively, the molecular silanols can condensate into siloxane polymers (Fig. 1.3 vertical reaction from B to C) that subsequently can react with the surface silanols to directly form fully cross-linked surface siloxane backbones (Fig. 1.3C, horizontal reaction) [56, 57, 59]. Note: this is a simplified and schematic description of possible reactions. The condensation reactions

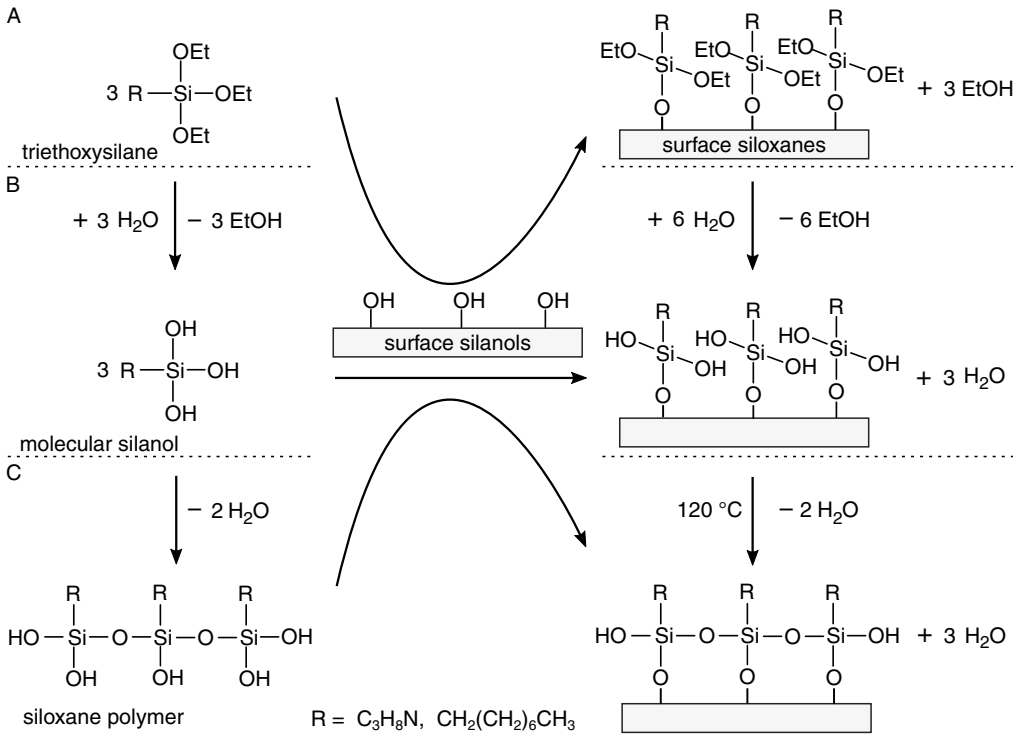

Figure 1.3.: Triethoxysilanes (A) react with surface silanols to surface siloxanes (horizontal reaction). When water is present, the remaining ethoxy groups of the surface siloxanes can be replaced by silanols which then can condensate into fully cross-linked siloxane backbones (reaction favoured at 120°C, vertical reaction). The triethoxyilanes (A) can hydrolyse alternatively into molecular silanols (B). The molecular silanols can either condensate with surface silanols to surface siloxanes (horizontal reaction) or with other molecular silanols to form siloxane polymers (vertical reaction from B to C). Alternatively, siloxane polymers (C) can react with surface silanols to form surface siloxanes (horizontal reaction).

of the silanols can be catalyzed under acidic or basic conditions or by the addition of primary, secondary or tertiary amines [56]. When the TES residue contains a primary amine as in the case of aminopropyl-triethoxysilane (APTES, R=C_3H_8N), the molecule undergoes self-catalysis [56, 57].

1.2.3. Proteins: microtubules and kinesins

Microtubules are part of the cytosceleton where they provide mechanical support and tracks for cellular transport. They are micrometer long and typically 25 nm thick protein tubules that consist of polymerized α-β tubulin subunits (Figure 1.4). Positions along the microtubule are described with the "microtubule lattice" [60,61]. Longitudinally viewed, the tubulins are arranged in a head-to-tail fashion building up polar protofilaments with an exposure of the β tubulin at the so-called "plus end" and the α tubulin at the "minus

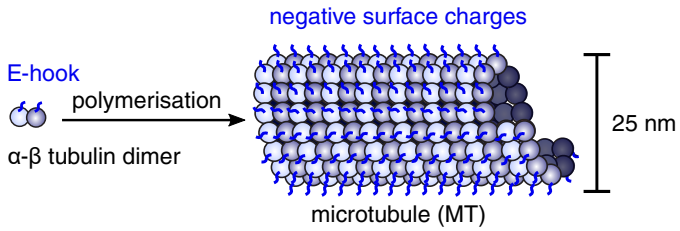

Figure 1.4.: α-β tubulin dimers can polymerize into microtubules. Due to the negatively charged E-hooks, microtubules carry negative surface charges.

end" of the microtubule. This terminology is derived from microtubule polymerization dynamics where the microtubule polarity is reflected: Microtubules grow faster at the "plus end" and only grow slowly at the "minus end" [62, 63]. Microtubule growth is guanosine triphosphate (GTP)/guanosine diphoshpate (GDP) and Mg^{2+} dependent. For polymerization, tubulin with bound GTP and Mg^{2+} is required and the hydrolysis state of the GTP is an important factor in the stability of the polymerized microtubule [62, 64–66]. GTP-tubulin has a different length compared to GDP-tubulin [67]. Thus, the energy released upon GTP hydrolysis is stored as strain between the lateral contacts of the microtubule lattice and finally results in depolymerization and shrinkage [67]. Therefore, microtubules can be stabilized by using the non-hydrolyzable GTP-analogue GMPCPP [68]. Alternatively, microtubule stabilization can be achieved by the usage of drugs such as the anti-cancer drug taxol or microtubule associated proteins (MAPs) [69–71]. Typically, interactions between MAPs and microtubules are based on hydrophobicity or electrostatic charge neutralization [72, 73]. In electrostatic terms, microtubules and their tubulins have very interesting properties. Single tubulin dimers carry a bare (vacuum) charge of -52 e under physiological pH. Out of this charge, $-24\,e$ (46 %) are spread among the tail-like C-termini of the two monomers. These negatively charged C-termini are called E-hooks. The charges of the E-hooks originate from aspartic (Asp or D) and glutamic (Glu or E) acid residues that make 49 % of the C-terminus. If the resulting dipole moment (about 4000 D per monomer) is summed up within a microtubule, their longitudinal components generate a length-dependent net dipole moment for a microtubule [60, 74, 75]. The microtubule surface mainly carries a negative electrostatic potential (about $-1\,\mathrm{kT}/e$) and only small regions with positive potential ($+1\,\mathrm{kT/e}$) are present. Interestingly, the electrostatic potential differs on the two ends of a microtubule: the plus end's electrostatic potential is negative similar to the rest of the microtubules surface while at the minus end the areas with a positive electrostatic potential are increased [76].

Kinesins are microtubule-associated motor proteins that can move processively along a microtubule "track" to perform crucial tasks within cells such as the transport of vesicles, organelles, chromosomes, protein complexes and the regulation of microtubule dynamics [77–79]. This processive motion is driven by adenosine triphosphate (ATP)-binding and hydrolysis induced conformational changes. Thus, ATP is considered to be the "fuel" of the kinesin motor [80–82]. The kinesin superfamily is composed of subfamilies (Kinesins 1-14) with kinesin-1 called conventional kinesin [78, 83].

1.2.4. Principles of microtubule attachment to surfaces

Electrostatic interactions The electrostatic properties of microtubules can be exploited to attach them to surfaces for *in vitro* assays and imaging. As microtubules are negatively charged, surfaces must be rendered positively charged to electrostatically attract the microtubules. Therefore, typically amino groups are introduced by adsorbed layers of polylysine or covalent layers of 3-aminopropyl-triethoxysilane (APTES) [5,84–87]. Upon exposure to water or aqueous buffers with neutral or acidic pH, the amino groups are protonated, become positively charged and are thought to bind the negatively charged microtubules due to electrostatic interactions (Fig. 1.5) [5].

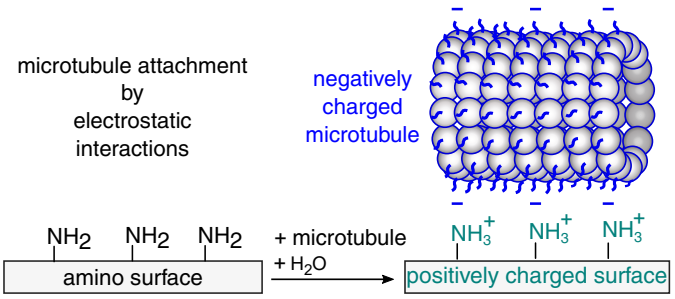

Figure 1.5.: An aminated glass surface becomes protonated and positively charged upon exposure to the aqueous buffer of a microtubule solution. The negatively charged microtubules are thought to bind to the surface via electrostatic interactions [5].

Hydrophobic interactions Alternatively, microtubules can be attached to surfaces exploiting hydrophobic and antigen-antibody interactions (Fig. 1.6). Here, glass surfaces are rendered hydrophobic by either spin coating with a hydrophobic polymer or a covalent attachment of hydrophobic surface groups via silanization [15, 17]. Subsequently, anti-tubulin antibodies are bound to the surface. How antibodies bind to surfaces is not yet fully understood. Some authors consider van der Waals interactions, others assume that upon contact with a hydrophobic surface, the antibody denatures partially and orients such that hydrophobic antibody parts stay attached to the surface avoiding contact with the surrounding aqueous solution [88–90]. This principle of dehydration of the hydrophobic surface is also exploited for the surface passivation of the remaining surface: the hydrophobic middle part of the triblock copolymer Pluronic F-127 orients towards the hydrophobic surface while the hydrophilic polyethylene glycol (PEG) outer

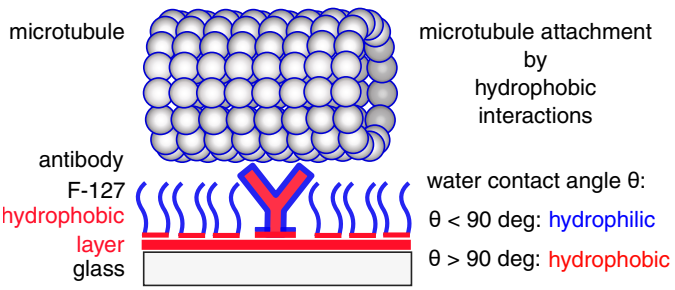

Figure 1.6.: Glass surface functionalized with a hydrophobic layer binds anti-tubulin antibodies and the triblock copolymer Pluronic F-127 through hydrophobic interactions. Microtubules attach specifically to the antibodies while the rest of the surface is passivated by F-127.

parts protrude in the aqueous solution for surface passivation [15, 91]. Hydrophilic microtubules will attach specifically to the respective antibodies [12, 15, 92, 93].

1.2.5. Surface-sensitive microscopy methods

Surface-bound microtubules can be visualized with high SBRs using surface-sensitive microscopy methods such as total internal reflection fluorescence (TIRF, when fluorescently labeled) and interference reflection microscopy (IRM, label-free detection). These methods are described in the following.

1.2.5.1. Total internal reflection fluorescence microscopy

TIRF microscopy exploits the properties of the evanescent field that is created upon total internal reflection of a laser beam at a sample surface. Total internal reflection is achieved by reflecting the excitation laser beam at the interface between cover glass (refractive index n_1) and sample (n_2) under the critical angle $\Theta_{critical} = sin^{-1}(n_1/n_2)$. The thereby generated evanescent field only penetrates the sample by the wavelength λ dependent penetration depth $d_p = \lambda/(4\pi)(n_2^2 sin^2\Theta - n_1^2)^{-1/2}$. The field can excite fluorophores with an intensity decaying exponentially with distance from the surface:

$$I_z = I_0 e^{-z/d_p} \tag{1.9}$$

with I_z being the intensity at the depth z and I_0 the initial intensity [94]. This restriction of the excitation volume to the focal plane improves SBRs compared to epifluorescence microscopy. Close to the critical angle, the intensity of the evanescent field can be up to 5 times greater than the intensity of the incident beam [95].

1.2.5.2. Interference reflection microscopy

IRM is a surface-sensitive, label-free microscopy method in which monochromatic light with the intensity I_0 illuminates a specimen containing glass surface (Fig. 1.7). Light is reflected by the glass surface (I_1) or transmitted into the sample, where the light can then be reflected by the specimen (I_2). Only upon the reflection at an interface with a higher refractive index, a 180° phase shift occurs. Typically the refractive index of glass (borosilicate glass, $n_0 \approx 1.52$ [96]) is higher than the refractive index of the medium (water, $n_1 \approx 1.33$ [97]). Thus, no phase shift occurs upon reflection at the glass-water interface. In the contrary, the refractive index of the specimen (e.g. protein, $1.36 < n_2 < 1.55$ [98]) is typically higher than the refractive index of the medium n_1. Therefore, a 180° phase shift occurs typically upon reflection at the medium-specimen interface. When the specimen is directly located at the glass surface, a fully destructive interference of I_1 and I_2 occurs which results in a black IRM signal I_{IRM}. If the specimen is located at a different height, the effective phase shift between the two interfering waves depends on the optical path difference. The optical path is the product of the physical path of the light and the refractive index of the medium through which the light travels. When all refractive indices (n_0, n_1, n_2) can be considered as constant, the physical path difference

h between glass surface and specimen can be quantified according to the interference patterns resulting from it. Theoretically, the intensity of the IRM image I_{IRM} can be directly related to the height of the specimen above the surface h according to [99, 100]:

$$I_{IRM} = I_1 + I_2 - 2\sqrt{I_1 I_2}\cos\left(\frac{4\pi n_1 h}{\lambda}\right) \tag{1.10}$$

with λ being the illumination wavelength. However, for a realistic understanding of the experiment, Eq. 1.10 requires to be corrected for the objective's point spread function according to [100, 101]:

$$2 \cdot I_{IRM,corrected} = S + D\frac{\sin y}{y}\cos\left(\frac{4\pi n_1 h}{\lambda}(1 - \sin\alpha/2)\right) \tag{1.11}$$

The point spread function is modeled by $y = 2kh\sin(\alpha/2)^2$ were $\alpha = \arcsin(INA/n_1)$ is half the angle of the cone of the illumination numerical aperture (INA). The interference amplitude D scales the function to the intensity values obtained by the setup and camera settings. The factor S corrects the intensity values for a background [99–101]. Figure 1.7B compares the results of Eq. 1.10 (black) and Eq. 1.11 (magenta). Here, absolute intensity values are neglected and only the pattern of the cosine functions $\cos\left(\frac{4\pi n_1 h}{\lambda}\right)$ and $\frac{\sin y}{y}\cos\left(\frac{4\pi n_1 h}{\lambda}(1 - \sin\alpha/2)\right)$ are compared for a wavelength of $\lambda = 450\,\text{nm}$, the refractive index of water $n_1 = 1.33$ [97] and an INA of 1.15. It becomes clear, that considering realistic illumination conditions leads to a noteworthy deviation from the theoretical interference.

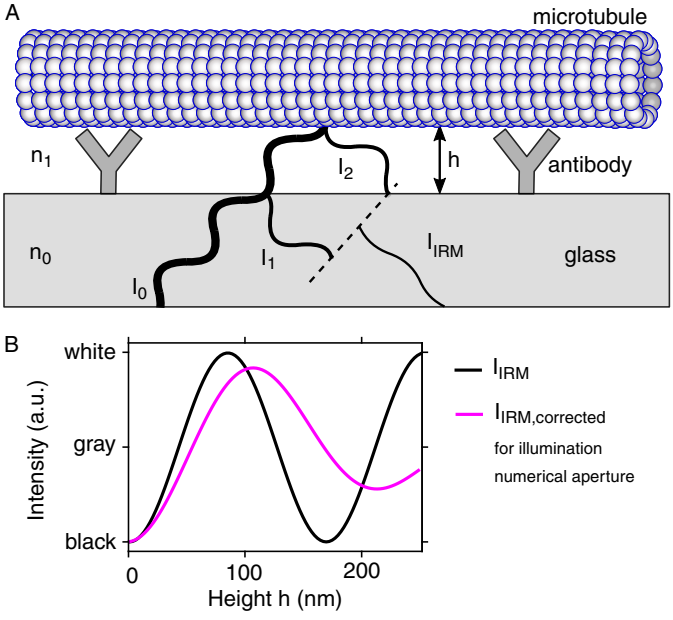

Figure 1.7.: (**A**) The incident light I_0 is reflected at a glass surface (I_1) and by a microtubule (I_2). The height h of the microtubule above the surface determines how (I_1) and (I_2) interfere. In the depicted example, (I_1) and (I_2) interfere destructively and the detected intensity I_{IRM} is reduced. Figure adapted from Ref. [102]. (**B**) Plots of the IRM intensity calculated according to Eq. 1.10 (black) and the IRM intensity corrected for an INA of 1.15 according to Eq. 1.11 (magenta).

1.2.6. X-ray photoelectron spectroscopy

For x-ray photoelectron spectroscopy (XPS), a sample is irradiated with soft x-rays of a known wave length ($h\nu < 6$ keV). At the sample surface, the x-ray energy ($h\nu$) is transferred to a core level electron which is then emitted as a photoelectron (photoelectric effect). The kinetic energy (KE) of the photoelectron is detected and its previous binding energy (BE) calculated according to:

$$BE = h\nu - KE - \Phi_{spec} \tag{1.12}$$

with Φ_{spec} being the spectrometer work function. The emission of the photoelectron generates a core hole that can be filled with an electron from a valence orbital. This relaxation process releases energy either as x-ray fluorescence (not detected) or the emission of an Auger electron. Auger electrons are denoted using the K, L and M nomenclature for atomic orbitals. For instance, the term "KLL" states the following: first, the x-ray radiation ejected an electron from a K orbital. Second, the thereby generated core hole was filled by an electron of the L orbital. Third, the ejected Auger electron originates from an L orbital. The binding energy of both photoelectrons and Auger electrons differs for different elements and further depends on the state of oxidation and the chemical environment of these elements. Therefore, with XPS the chemical composition of a surface can be analyzed [103].

1.3. Materials & Methods

1.3.1. Materials

All chemicals were purchased from Sigma Aldrich and used without further purification unless noted otherwise. Purified Type 1 water was used for all experiments (18.2 MΩ cm, Nanopure System MilliQ reference with Q-POD and Biopak filter). Glass staining jars (BRAND™ Soda Lime Glass Staining Troughs with Lid, Fisherscientific, US) were used to store and treat all cover slides. Teflon (TE) racks (custom-made at the university workshop) were used for glass slide treatments unless noted otherwise. All procedures were performed at room temperature (20–28 °C) unless noted otherwise.

Glass slide specifications For the construction of flow cells, square cover glasses with different thicknesses (d) and surface areas (A) were purchased:

1. 0.08 mm $< d <$ 0.12 mm and A = 18 mm × 18 mm (Thermoscientific #0 Menzel-Gläser, Braunschweig, DE). These cover slides are for the top of the flow cell and thin enough for the final flow cell to fit into a specific setup (called "Aswad" [104]).

2. 0.13 mm $< d <$ 0.16 mm and A = 18 mm × 18 mm (Thermoscientific #1 Menzel-Gläser, Braunschweig, DE). These cover slides are an alternative for the top of the flow cell and thick enough to not float when KOH/H_2O_2 etched.

3. 0.16 mm $< d <$ 0.19 mm and $A = 22\,\text{mm} \times 22\,\text{mm}$ (Corning Square #1.5 cover glasses, Corning, New York, US). These cover slides are the bottom part of the flow cells, fit in all used sample holders and their thickness is optimized for reducing optical aberrations [105]. Additionally, this slide thickness offers a good stability for supporting the flow cell.

All glasses were pure white borosilicate glasses (D263) suited for fluorescence microscopy and of high chemical resistance ("hydrolytische Klasse 1"). For these glasses it is additionally guaranteed that no bubbles or streaks are present [106, 107].

1.3.2. Surface preparations

1.3.2.1. Cleaning and surface activation

Sonication and solvent based cleaning Glass slides were sonicated (Ultrasonic cleaner USC-THD, VWR, US) in 5 % Mucasol (Schülke & Mayr GmbH, Norderstedt, DE) for 3 min and washed with water. Subsequently, they were sonicated for 3 min in acetone and washed again with water. Drying was performed by a combination of blow drying with nitrogen and placement in an 65 °C warm oven (ULM 500, Memmert, Büchenbarch, DE).

Potassium hydroxide / hydrogen peroxide etching Potassium hydroxide / hydrogen peroxide etching [45, 108] was performed as instructed by Ronny Löffler [109] except that cover slide racks were used: TE racks with cover slides were immersed in 0.9 M KOH and slowly heated up to 60 °C while carefully adding 10 % H_2O_2 in water until a molarity of 0.13 M was reached. Heating and H_2O_2 addition needed to be done carefully as an increased gas formation during the etching process needs to be monitored closely, especially to prevent the slides from floating out of the holder. Only glass slides thicker than 13 mm were used during H_2O_2 etching processes as they were heavy enough to not float out of the holder. After 1h of exposure, the solution with the racks was allowed to cool down and the slides were extracted and washed 3 × in deionized water.

HCl-sonication-based cleaning and hydroxylation HCl-sonication-based surface activation was performed as described earlier [18]. Clean glass slides stored in TE racks were sonicated in 75 °C hot 1 M HCl for 1 h. To remove all residual Cl^- ions, the slides were sonicated thrice for 5 min in deionized water.

KOH-sonication-based etching and hydroxylation This surface activation procedure was performed similar as described for the HCl-sonication-based surface activation, except that the slides were immersed in a 1 M aqueous solution of KOH for only 5 min, followed by a sonication-free final washing in water.

Plasma-based cleaning and hydroxylation Sonicated and solvent cleaned slides were plasma activated and cleaned for 5 mins. A TePla plasma cleaner (Plasma system 100E,

PVA TePla AG, Wettenberg, DE) was used to generate O_2 (0.7 mbar process gas pressure, 300 W radio frequency (RF) power) and N_2 (0.5 mbar process gas pressure, 300 W RF power) plasma. Air plasma was generated at the plasma system Zepto (Diener, Ebhausen, DE) with 0.7 mbar process gas pressure and 100 W RF power. For polypropylene (PP)-assisted treatments (see results), glass infused PP holders (Wash-N-Dry coverslip racks WSDR-1000, Diversified Biotech, Doylestown, US) were used instead of TE holders. An increased pressure in the vacuum chamber observed during PP decomposition in oxygen plasma was compensated by reducing the process gas stepwise to maintain the 0.7 mbar process pressure. The closing of the process gas valve after finishing the plasma process was performed within milliseconds to reduce the amount of process gas reacting with the plasma treated surface.

1.3.3. Silanizations

Sonication- and solvent-cleaned glass slides were either KOH / H_2O_2 etched, HCl cooked, KOH etched, or plasma treated for further hydroxylation. Dryed hydroxylated glass slides were silanized according to one of the following procedures.

1.3.3.1. Trimethylchlorosilane (TMCS)

800 μL TMCS was evaporated in a dessicator by alternating intervals of vacuum generation (20 mbar, PC 3004 Vario with CVC 3000 display, Vacuubrand, Wertheim, DE) as described earlier [18].

1.3.3.2. Hexamethyldisilazane (HMDS)

HMDS silanization was performed as described in Ref. [110] except that 4.5 mL HMDS were added to the bottom of glass staining jars containing freshly hydroxylated slides in TE racks. The slides were incubated in the closed staining jars for 48 h at 25 ℃.

1.3.3.3. Octadecyltriethoxysilane (OTES)

OTES treatment was slightly modified from Ref. [111]: Hydroxylated glass slides were submerged within a mixture of 200 mL toluene, 4 mL OTES (abcr, Karlsruhe, DE) and 1 mL *n*-butylamine (nBuNH$_2$) catalyst for 90 min. To remove residual chemicals, the slides were swirled in toluene, sonicated 3 min in acetone and were subsequently swirled in water and dried (dry, filtered and pressured air).

1.3.3.4. Aminopropyl-triethoxysilane (APTES)

Vapour silanization was performed similar as described in Ref. [112]: 500 mL of APTES were filled in a small petri dish located at the bottom of a dessicator containing clean and dry glass slides.

Next, a 15 mbar vacuum was generated within the dessicator (Vacuum pump PC 3004 Vario with CVC 3000 display, Vacuubrand, Wertheim, DE). Then, the dessicator was closed and the slides were incubated in APTES vapour for 30 s.

Liquid silanization was performed as described earlier [5] by immersing cleaned cover slide racks first in acetone, then in a 2% APTES-tolouene solution for 10 s and subsequently in acetone.

To remove adsorbed polymers, APTES functionalized slides were sonicated in ethanol for 10 min and in deionized water for 5 min, respectively. Both sonication steps were repeated. Finally, the glass slides were dried and stored in a vacuum dessicator.

1.3.4. Glass chamber constructions

Four different types of glass chambers were constructed from readily functionalized glass slides (Fig. 1.8). All chambers used the 22 mm glass slide as a bottom slide and a 18 mm glass slide as a top slide but differed in the choice of spacers and sealings:

A Droplet volume is spacer and sample at the same time, sealed with nail polish (Volume gloss, P2).

B Double-sticky tape (Tesa, part of Hexagon AB, Stockholm, Sweden) as spacer, no sealing [5, 18].

C Melted parafilm (Bemis Company Inc., Neenah, US) spacers, no sealing [5, 18].

D Silicone film (thickness d =0.4 mm, SIPZBS0,4UT30C250x250-PSA100, MVQ Silicones GmbH, Weinheim, DE) spacers, ultrathin pipette tips (Microloader, Eppendorf) as channel entries and epoxy (5 min Epoxy Harz und Härter, R & G Faserverbundwerkstoffe GmbH, Waldenbuch, DE) sealing.

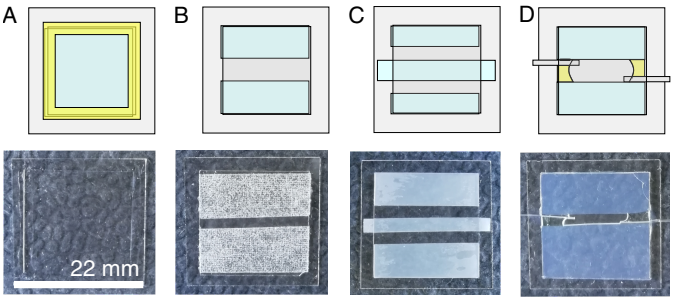

Figure 1.8.: Schematic drawings (top) of different types of flow cells (**A**–**D**, specified in the main text) built from two differently sized coverslides (grey), spacers (light blue) and sealings (yellow). Pictures of the respective flow cells are shown below.

1.3.5. Microtubule polymerization and stabilization

1.3.5.1. Taxol-stabilized microtubules

Porcine tubulin (25 μM) was polymerized in PEM buffer (80 mM PIPES, 1 mM EGTA, 1 mM $MgCl_2$, pH = 6.9) supplemented with 4 mM $MgCl_2$ and 1 mM GTP for 30 min at 37 °C as described previously [113]. Afterwards, the microtubule solution was diluted (1:40 ratio) in PEM-T (PEM buffer with 1% Paclitaxel), centrifuged (Airfuge Beckman Coulter, Brea, CA), and resuspended in 150 µL PEM-T.

1.3.5.2. GMPCPP-stabilized microtubules

Porcine tubulin (2 μM) was polymerized in PEM buffer supplemented with 4 mM $MgCl_2$ and 1 mM GMPCPP for 4 h at 37 °C as described previously [113]. Afterwards, the microtubule solution was diluted (1:40 ratio) in PEM, centrifuged (Airfuge Beckman Coulter, Brea, CA), and resuspended in 150 µL PEM buffer.

1.3.6. Microfluidic chamber treatments

1.3.6.1. Microtubule-kinesin assays

APTES-based microtubule-kinesin assay The channel was washed twice with 20 μL water and once with 20 μL PEM buffer. Then, 10 μL GMPCPP-stabilized microtubules were incubated for 10 s and unbound microtubules were washed out with 20 μL PEM buffer. Finally, 10 μL kinesin-8 (yeast, Kip3-eGFP-His6) was diluted to 5 nM in motility buffer (PEM, 0.08 mg/mL casein, 1 mM ATP, 20 mM D-glucose, 250 nM glucose oxidase, 134 nM catalase, 10 mM dithiotrethiol in PEM buffer) and imaged.

Hydrophobic interaction-based microtubule-kinesin assay Underpressure (Vacuum pump PC 3004 Vario with CVC 3000 display, Vacuubrand, Wertheim, DE) was applied to one end of the hydrophobic flow chamber channel and used for the following washing and treatment steps. Microtubule attachment, surface passivation and kinesin assays were performed as explained previously [113] except that antibodies were directly incubated to a clean surface without previous washing steps and that incubation times of 3 min (antibody) and 10 min (F-127) were sufficient, 10 mM dithiotrethiol was used instead of β-mercaptoethanol. Kinesin-1 (rat, trunkated rk430-eGFP-His6) was the used motor protein.

1.3.7. Analytical Methods

1.3.7.1. Surface-sensitive microscopy

IRM and TIRFM images were measured at room temperature (23 °C) on a setup similar to a previously published setup [104] combining IRM and TIRF. The TIRF excitation wavelength was 488 nm (100 mW LuxX 488-100 Omicron Laser, Rodgau, DE) for the green channel. The green channel was defined by an ET Bandpass 520/40. The image

acquisition time was 200 ms using an Orca Flash 4.0 V2 camera (Hamamatsu Photonics, Hamamatsu City, JP). For IRM illumination, a blue LED (Royal-Blue LUXEON Rebel LED, Lumileds, DE) with an emission wavelength of $\lambda = 450 \pm 20$ nm was operated at 3 V and a current of 0.1 A. IRM imaging was performed with a CCD camera (LU135-M, Lumenera, Canada) at 60 frames per second (fps).

1.3.7.2. SBR determination

IRM images From an image stack containing 20 IRM images, 40 pixel long straight line segments of microtubules were chosen and 40×40 pixel ROIs were generated, centered around these line segments, using a slightly modified "ROIsaveTool" in Fiji, originally written by Steve Simmert. These ROIs were averaged and their SBRs were determined using a Python script written by Steve Simmert [101]. This script generated a median profile perpendicular to the microtubule axis from the ROI and approximated the microtubule profile with a Gaussian fit. Next, the script subtracted the fitted Gaussian from the image to determine the residual image. The noise of the residual image was filtered as described in Ref. [101] to not overestimate noise caused by irregularities, dirt, drift or illumination intensity fluctuations. The intensity distribution of the filtered residuals was fitted to another Gaussian and its standard deviation (SD) was considered as noise. The SBR was determined as the ratio between microtubule profile and noise.

TIRF images To determine the average gray value of the kinesin decorated microtubules, average line profiles perpendicular to the microtubule axis were generated from image stacks containing 100 TIRF images as described in the previous paragraph. The maximum of these average line profiles was used as the "signal" of the kinesin decorated microtubule. Next, the average gray value of the background, originating from kinesins unspecifically interacting with the surface, was determined. Therefore, 100×100 pixel ROIs of microtubule-free regions were taken from the average image of the image stack. The average gray level of these background-containing ROIs was considered as the "background" value. The dark background value of a kinesin-free sample was subtracted from the "signal" and "background" gray levels, respectively. Finally, the ratio of the "signal" (S) divided by the "background" (B) was used as the SBR. The error propagation was calculated according to $\delta SBR = SBR \cdot \sqrt{(\delta S/S)^2 + (\delta B/B)^2}$

1.3.7.3. Kinesin motility parameters

Kymographs were obtained by plotting the microtubule axis horizontally *vs* the time axis through the image stack vertically. Kinesin traces shorter than 4 pixels were excluded from the analysis due to difficulties to clearly identify these events as processive motion. Kinesin traces appearing to be due to the movement of multiple kinesins (clusters, different brightnesses, partial bleaching) were excluded as well.

1.3.7.4. Contact angle measurements

Static contact angle (CA) measurements were performed at a temperature of 23–25 °C using the sessile drop method on the CAM 200 optical angle meter (KSV Instruments LTD). The drop volume was 2 µL and 12 droplets were measured per surface. Three surfaces were measured per sample yielding 36 CAs per sample. Six batches were measured per method on different days yielding 216 droplets per method. As no systematic difference was visible between left and right angles, all measured angles were considered separately yielding 432 CAs per method. Statistical tests were performed according to a one-way ANOVA with Tukey HSD post-hoc test with a confidence level of $\alpha = 0.01$ using the Real Statistics Data Analysis Tool with Excel.

1.3.7.5. Fabrication of methylated surfaces with different CAs

Methylated surfaces with different CAs ranging from 28 to 93 deg were fabricated as stated in Table 1.1.

Table 1.1.: Fabrication of methylated surfaces with different CAs. All surfaces were precleaned as described in Paragraph 1.3.2.1. All processes stated in the table are explained in Sect. 1.3.2 in more detail. TE holders were used.

CA	**Cleaning & Activation**	**Silane**
28	O_2 plasma	TMCS
61	O_2 plasma	HMDS
82	O_2 plasma + heating in H_2O	HMDS
87	O_2 plasma + etching in HCl	HMDS
93	O_2 plasma + etching in HCl	HMDS

1.3.7.6. Fitting of the SBR data

Fitting model According to the Cassie equation, the effective CA of a liquid on a flat surface composed of two different materials can be calculated according to:

$$\cos(CA) = a_1 \cdot \cos(\Theta_1) + a_2 \cdot \cos(\Theta_2). \tag{1.13}$$

Here, the materials are considered as area fractions $a_{1,2}$ characterized by the respective CAs $\Theta_{1,2}$ [114].

Since the experimentally prepared surfaces were initially superhydrophilic after the plasma activation, we used $\Theta_1 = 0$ deg for a_1. We further assumed, that the HMDS silanization added a second hydrophobic area fraction a_2 with a CA of $\Theta_2 = 90$ deg. Inserting Θ_1 deg and Θ_2 deg into Eq. 1.13 related the effective CA directly to the hydrophilic area fraction a_1:

$$\cos(CA) = a_1. \tag{1.14}$$

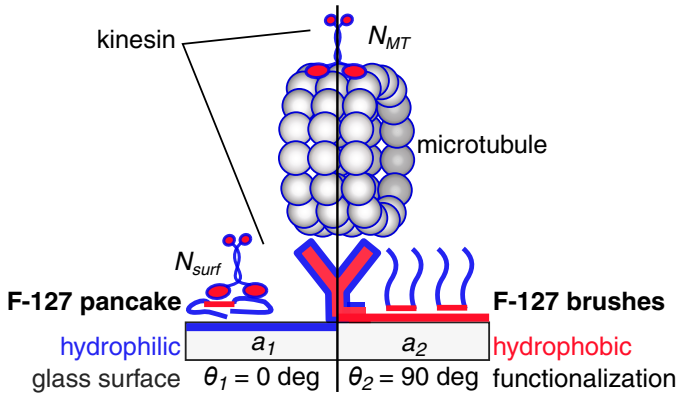

Figure 1.9.: F-127 adsorbs to a hydrophilic surface area a_1 (blue, $\Theta_1 = 0\,\text{deg}$) in a "pancake" configuration and to a hydrophobic surface area a_2 (red, $\Theta_2 = 90\,\text{deg}$) in a brush configuration [115]. The "pancake" configuration may allow nonspecific binding of kinesins to the surface (N_{surf}) in addition to specific microtubule binding (N_{MT}).

The effective CA of a surface was relevant, since the CA was reported to affect the adsorption configuration of the surface passivating agent F-127 [115]. For a hydrophilic surface, F-127 is thought to adsorb in a "pancake" configuration (Fig. 1.9, left). For a surface with a CA above 80 deg, F-127 is expected to adsorb in a brush-like configuration (Fig. 1.9, right) [115]. While F-127 polymer brushes are used to passivate surfaces against unspecific kinesin interactions [15], F-127 in a "pancake" configuration may not operate as a functional passivating agent. The "pancake" configuration may allow kinesins to bind nonspecifically to surfaces (N_{surf}, Fig. 1.9, left). Ideally, kinesins should only specifically interact with microtubules (N_{MT}, Fig. 1.9, middle). The number of microtubule-bound kinesins N_{MT} is proportional to the landing rate that in turn is proportional to the concentration of kinesins in the solution N_{sol}. N_{sol} can be determined by subtracting N_{surf} from the total number of kinesins N_t present in the assay. Using the proportionality constant k to account for the landing rate and other factors, N_{MT} can be calculated according to:

$$N_{MT} = k \cdot N_{sol} = k(N_t - N_{surf}) \tag{1.15}$$

Since the hydrophobic area fraction a_2 is expected to be efficiently blocked by F-127, N_{surf} was expected to scale with the poorly blocked area fraction a_1. For a completely hydrophilic surface ($a_1 = 1$, $a_2 = 0$), the surface passivation is expected to be the least efficient and the number of nonspecifically surface-bound kinesins N_{surf} to be maximal. This maximum amount of N_{surf} is N_S. Therefore, we assumed

$$N_{surf} = N_S \cdot a_1. \tag{1.16}$$

The SBR of an unlabeled microtubule decorated with eGFP-labeled kinesins was expected to be the ratio of N_{MT} and N_{surf} plus a constant, kinesin-independend background:

$$SBR = \frac{N_{MT}}{N_{surf} + Bkg}. \tag{1.17}$$

Inserting Eq. 1.14, Eq. 1.15 and Eq. 1.16 into Eq. 1.17 yields the final equation used for fitting the SBR dependence on the CA:

$$SBR = k\frac{N_t - N_S \cdot \cos(CA)}{N_S \cdot \cos(CA) + Bkg}. \tag{1.18}$$

The model is only valid for CAs $\leq$ 90 deg and does not consider any effects that may lead to a saturation such as denaturation of antibodies or changes in the polymer brush dimensions.

Fitting procedure To fit the SBR data with Eq. 1.18 containing 4 different variables, more data was required. Therefore, the "Signal", "Background" and SBR data was fitted simultaneously with shared variables and the following functions: The SBR data was fitted with with Eq. 1.18, the "Signal" data with $N_{MT} = k(N_T - N_S \cdot \cos(CA))$ and the "Background" data with $N_S \cdot \cos(CA) + Bkg$. Weighed fitting was performed based on the error bars of the data. Since the model is only valid for CAs $\leq$ 90 deg, the last data point at 93 deg was not included in the fit. The resulting fit parameters were $a = 6.7 \pm 3.5$, $N_t = 13.6 \pm 5.9$, $N_S = 8.9 \pm 2.8$ and $Bkg = 1.5 \pm 0.6$.

1.3.7.7. XPS measurements

XPS measurements and analysis were performed in cooperation with Dustin Quinones and Prof. Heiko Peisert of the "Interfaces of Organic Semiconductors" group (University of Tübingen, DE). Measurements were performed using a multi-chamber ultrahigh vacuum system (base pressure 8×10^{-9} mbar) including a Phoibos 100 analyzer, a 1d-Delay Line detector (SPECS, DE) and an X-ray source with a conventional Al/Mg anode (XR-50 m X-ray source). All measurements were performed with Mg Kα radiation ($hv = 1253.6$ eV), a dwell time of 0.2 s and a pass energy of 20 eV. The overview spectra were recorded from −5–1100 eV and a step size of 0.5 eV. The core-level spectra of the individual elements (Si2p, C1s, O1s) were collected with a 0.05 eV step size. The shifts observed due to charging effects of the glass surface were corrected as described earlier [26]. The peak centers were determined using Gaussian fits. To determine the elemental composition and atomic percentages, peak areas were calculated using Python and weighted with Yeh and Landau sensitivity factors [116].

1.4. Results & Discussion

Section 1.4.1 focuses on the optimization of hydrophobicity-based kinesin-microtubule assays. In Sect. 1.4.2, the SBRs of microtubules attached via different methods are compared and correlated to height information.

1.4.1. Coverslide hydrophobization was optimized for kinesin stepping assays

While various approaches to render glass surfaces hydrophobic by silanization exist, the reproducibility of these procedures remains an important issue of ongoing research [6,19]. In this section, different surface modification approaches are compared. I developed a new protocol that yielded high quality, low background surfaces with an optimal water contact angle suited for kinesin assays that are based on hydrophobic interactions.

1.4.1.1. Suited cleaning procedures yielded superhydrophilic surfaces

To demonstrate to what extent insufficient cleaning procedures can affect the reproducibility of a silanization protocol, the desired contact angle (CA) obtained by silanization is compared with the CA of an uncleaned coverslide. For hydrophobicity-based microtubule-kinesin assays, a CA of 90 deg was reported to be required [18]. A dirty coverslide that was solely rinsed with water for the removal of major dust particles already had a CA of 74.7 ± 3.6 deg (mean $\pm$ SD, $N = 98$ CAs, 1 exemplary batch with 3 slides). To remove the majority of hydrophobic dirt, the glass slices were sonicated in acetone, resulting in a reduced CA of 37.2 ± 5.1 deg (mean $\pm$ SD, $N = 343$ CAs, 5 batches with 3 slides). A further cleaning of the acetone sonicated surfaces with either HCl, KOH or KOH-H_2O_2 etching or plasma treatments yielded superhydrophilic surfaces.

As expected, the CA of the acetone sonicated surface was close to the literature value of 33.6 ± 2 deg for an almost fully dehydroxylated surface [117]. This agreement with the literature suggests that the glass surfaces obtained directly from the manufacturer were mainly dehydroxylated. The slightly higher CA of the acetone sonicated surfaces compared to the literature value suggests that not all hydrophobic dirt was fully removed and that a more efficient cleaning was necessary. The superhydrophilic surfaces achieved by chemical etching were partially in agreement with the literature where CAs strongly depended on the chemical etching protocols [27,118]. Comparing literature reports with my results, it seems that superhydrophilic surfaces resulted from less aggressive chemical etching procedures performed in hot aqueous solutions that yielded rather smooth hydroxylated surfaces. Comparably, the literature relates plasma treated, superhydrophilic surfaces to smooth surfaces and higher surface silanol densities [26, 119, 120]. Overall, all suited cleaning procedures yielded superhydrophilic surfaces that required additional surface hydrophobization by silanization.

1.4.1.2. Choice of silane for cover slide hydrophobization

To reliably achieve high-quality hydrophobic surfaces, different types of silanes were further investigated. According to the literature, the CA of a surface suited for assays based on hydrophobic interactions should be 90 deg or above (black solid line in Fig. 1.10A) [18]. To achieve such CAs, two different standard cleaning procedures, O_2 plasma activation and HCl etching [5,18], were used to generate freshly hydroxylated

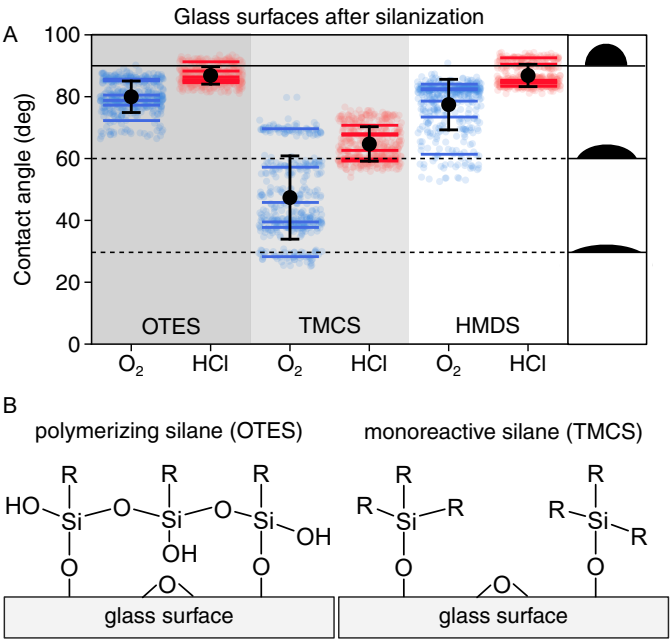

Figure 1.10.: (**A**) CAs obtained for glass surfaces after silanization with OTES, TMCS and HMDS with either O_2 plasma (blue) or HCl etching (red) used for hydroxylation. All steps were performed using TE holders. Single values are displayed as small light colored dots, averages of the distinct batches as colored lines and the total averages as large black dots with SDs as error bars. For reference, horizontal lines are drawn at CAs of 30, 60 and 90 deg with the respective CA silhouettes shown on the right. (**B**) Polymerizing silanes such as OTES can potentially bridge unhydroxylated sites while monoreactive silanes such as TMCS cannot.

glass surfaces. These surfaces were then treated with three different types of silanes: the triethoxysilane representative octadecyltriethoxysilane (OTES), the chlorosilane representative trimethylchlorosilane (TMCS) and the disilazane representative hexamethyldisilazane (HMDS). After the functionalization, their surface hydrophobization potential was investigated by measuring the water CAs (Fig. 1.10A). The hydrophobization potentials are directly comparable, as the exact same batches of activated surfaces were used for all three silanizations at the same time.

Octadecyltriethoxysilane Based on previous experiences with the triethoxysilane APTES [121], the triethoxysilane OTES was expected to efficiently functionalize the surface. As expected [111], CAs approaching 90 deg could be easily reproduced for HCl treated slides having a CA of 86.9 ± 2.8 deg (mean $\pm$ SD, $N = 432$). Interestingly, the O_2 plasma cleaned and OTES silanized surfaces resulted in a lower CA of 80.0 ± 5.1 deg (mean $\pm$ SD, $N = 432$). This suggested that the O_2 plasma activation was less efficient than the HCl activation. Different surface roughnesses causing such differences were expected to be negligible as both HCl and plasma treatments resulted in superhydrophilic surfaces. The high consumption of solvents, the work intensity, the waste production, and proneness to catch contaminations during the frequent liquid exposures were experienced as disadvantages. These issues can potentially be solved by applying OTES via vacuum silanization. However, the main reason to not further pursue OTES silanization,

was the ability of triethoxysilanes to polymerize upon water contamination [56, 59, 122]. A possible interaction of these polymers with later introduced samples (that were close to the surface) was undesirable. The presence of polymers on the surface can already be suspected when comparing the sensitivity of the OTES CA to the activation method with the sensitivity of TMCS. While a monofunctional and monolayer forming silane such as TMCS can only react with hydroxy groups, polymerized OTES can potentially bridge over unhydroxylated surface areas [122] and thereby possibly yield a higher CA than the non-polymerizing TMCS would for the same hydroxy density (Fig. 1.10B).

Trimethylchlorosilane As already mentioned, the TMCS silanization was more sensitive towards the used cleaning procedure than the OTES silanization: O_2 plasma cleaned surfaces had a CA of 47.4 ± 13.5 deg (mean $\pm$ SD, $N = 410$), while HCl activated surfaces had a CA of 64.7 ± 5.6 deg (mean $\pm$ SD, $N = 432$). All CAs were far from approaching the desired 90 deg. This observation was partially contradictory and partially in agreement with the literature: Herzberg *et al.* reported a CA of 85 deg for a highly controlled vacuum silanization procedure and pointed out its sensitivity to air humidity [123]. Skop *et al.* reported CAs of 70 deg for a liquid approach without the use of a catalyst (and 110 deg with the catalyst imidazole) and demonstrated the limitations due to the reactivity of the TMCS [6]. Thus, our low CAs possibly originate from the difficulty to exclude air humidity in our simple lab dessicator and the absence of a catalyst. More reactive chlorosilanes (di- or tri-chlorosilanes) are more sensitive towards air humidity [22,23,124] and did not improve the results.

Hexamethyldisilazane A promising candidate for a reliable and more effective surface methylation under ambient air conditions was HMDS. An increased reactivity towards surface silanol groups compared to mono-chlorosilanes such as TMCS was reported, while being less reactive towards water [22, 125]. Indeed, when HMDS was applied to the same cleaning and activation protocols already used for TMCS (and OTES), a CA of 86.9 ± 3.9 deg (mean $\pm$ SD, $N = 432$) was achieved for the HCl treated slides and a CA of 74.6 ± 11.1 deg (mean $\pm$ SD, $N = 494$) for the O_2 plasma treated slides. Comparable to TMCS, the high SD of 11.1 deg for the O_2 plasma treated slides suggests a high sensitivity towards the surface silanols and the inability to polymerize [22, 125]. For an improved comparison, the results are listed in Table 1.2. Values of the individual batches are shown in Appendix A.2.

Overall, CA approaching 90 deg could be achieved combining HCl treatment and OTES or HMDS silanization. However, as OTES silanes are capable of polymerization, the surface methylating silane HMDS was preferred.

Table 1.2.: Contact angles (CAs) of differently activated (HCl etching or O_2 plasma) glass surfaces after silanization with either OTES, TMCS or HMDS. CAs of N droplets were acquired for six different samples per method. All CAs were about zero before silanization. TE holders were used. Mean ± SD (N).

Treatment	**CA (deg)** HCl etching	**CA (deg)** O_2 plasma
OTES (liquid phase)	86.9 ± 2.8 ($N = 432$)	80.0 ± 5.1 ($N = 432$)
TMCS (vapour phase)	64.7 ± 5.6 ($N = 432$)	47.4 ± 13.5 ($N = 410$)
HMDS (vapour phase)	86.9 ± 3.6 ($N = 432$)	74.6 ± 11.1 ($N = 494$)

1.4.1.3. Further optimization of the surface activation

To find a substitute to the waste producing, work intensive and contamination prone HCl etching activation procedure, I compared different surface activation (hydroxylation) methods.

Liquid phase activation As all cleaning procedures described at the beginning of this section (Sect. 1.4.1.1) yielded superhydrophilic—and therefore most likely hydroxylated—surfaces, they were further investigated in terms of their potential for surface activation. Freshly cleaned surfaces were silanized with HMDS and their CAs were measured. The H_2O_2 / KOH etched surfaces had a CA of 80.2 ± 1.4 deg (mean ± SD, $N = 76$, 1 batch) and were not further considered due to the required work effort, harsh chemicals and poor results. Interestingly, surfaces that were etched in 1 M KOH for 5 min or control samples that were simply cooked in water for 1 h had CAs approaching 90 deg after HMDS treatment: KOH etched surfaces had a CA of 89.6 ± 1.1 deg (mean ± SD, $N = 116$, 1 batch) and water cooked surfaces a CA of 87.4 ± 4.4 deg (mean ± SD, $N = 268$, 3 batches). Therefore, the HCl activation of the original protocol [18] could possibly be replaced by either a time saving 5 min activation in KOH or a mild, environmentally friendly 1 h activation in water. However, all liquid activation procedures had the disadvantage of being prone to catch contaminations during the liquid exposures and were, therefore, not investigated in further detail.

Plasma activation A very promising, alternative approach was plasma activation. This activation is performed in vacuum and almost contamination free. Since the usage of water or hydrogen plasma would have required more complex and expensive devices, easily accessible plasma procedures were investigated. The CAs of HMDS silanized surfaces with different preceding plasma activations are shown in Fig. 1.11. For an improved comparison, a black line is drawn through the control CA value based on HCl etching. An ANOVA with Tukey post-hoc test (N = 432, F = 417, $\alpha = 0.01$) was used to determine the significant differences between the CAs obtained with the different methods.

First, the plasma treatments without a sample holder will be discussed. The O_2 plasma treated surfaces (O_2, violet) had a CA of 78.2 ± 1.7 ($N = 360$). The air plasma treated surfaces (air, green) had a CA of 80.0 ± 2.1 ($N = 432$).

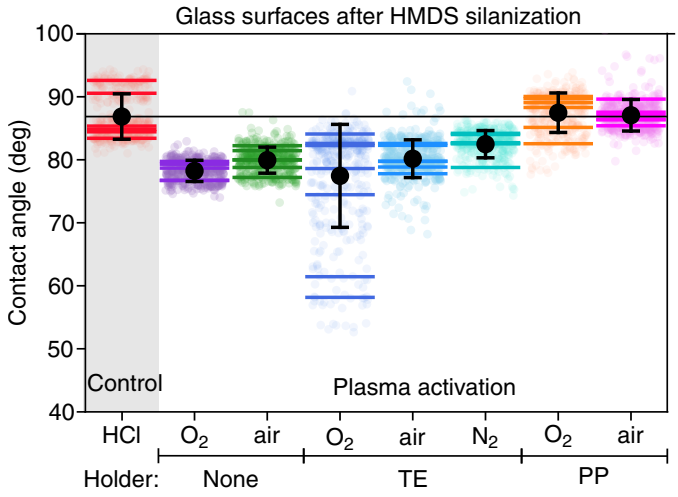

Figure 1.11.: CAs of HCl (red), O_2 (violet), air (green), $O_2 + TE$ (blue), air + TE (light blue), $N_2 + TE$ (cyan), $O_2 + PP$ (orange) or air + PP (magenta) plasma activated surfaces after HMDS silanization. All CAs are plotted as small colored data points. The averages of the batches are drawn as a colored lines. The average of all CAs is displayed as a large black data point with the SD as error bar. A black reference line is drawn through the CA of the HCl control sample.

Both plasma treatments without sample holder were not suited to achieve the desired CA of about 87 deg. The introduction of a TE sample holder to the O_2 plasma treatment ($O_2 + TE$, blue) yielded a significantly reduced CA of 74.6 ± 11.1 ($N = 494$, Tukey post-hoc analysis, $p < 0.001$, 3.60, 99 %-CI[2.41, 4.79]) with a noticeably increased SD. On the contrary, the introduction of a TE holder to the air plasma treatment did not change the CAs significantly compared to the air plasma without sample holder (Tukey post-hoc analysis, $p = 1.00$, 0.23, 99 %-CI[-0.94, 1.40]): the air + TE plasma (light blue) treated surfaces had a CA of 80.2 ± 3.0 deg (mean ± SD, $N = 432$). The $N_2 + TE$ (cyan) plasma treated surfaces had a significantly increased CA of 82.5 ± 2.2 (mean ± SD, $N = 432$) when compared to air + TE treated surfaces (Tukey post-hoc analysis, $p < 0.001$, 2.31, 99 %-CI[1.13, 3.48]).

Interestingly, only the introduction of a PP holder allowed the generation of surfaces with CAs approaching 90 deg. As expected for the plasma decomposition of a solid to gaseous products, the introduction of the PP holder to the $O_2 + TE$ plasma led to an increase in chamber pressure and the plasma flame changed from blue to white. After the HMDS treatment, the $O_2 + PP$ (orange) plasma treated surfaces had a CA of 87.5 ± 3.1 deg (mean ± SD, $N = 432$) that was significantly higher compared to the O_2 and $O_2 + TE$ plasma treated surfaces (Tukey post-hoc analysis, $p < 0.001$, 9.23, 99 %-CI[8.01, 10.46] and $p < 0.001$, 12.83, 99 %-CI[11.70, 13.97]). One disadvantage was the strong decomposition of the PP holders. This decomposition caused a deformation and surface roughening of the PP holders making a frequent reuse (more than three times) difficult. A reduction of the power for a milder plasma and to prevent the holders from damage did not work as it led to an irregular plasma flame at the device used for the generation of N_2 and O_2 plasma.

The device used for air plasma generated a homogenous plasma at lower power. Here, the PP sample holders did not deform visibly. Also, neither a visible change in the plasma color nor an increase in the plasma process pressure was observed apart from the initial outgassing of decomposed dirt in the first seconds. Surprisingly, the air + PP (magenta) treated surfaces had a CA of 87.1 ± 2.5 deg (mean $\pm$ SD, $N = 432$) after HMDS silanization. This CA was significantly higher ($p < 0.001$) compared to air and air + TE plasma activated surfaces according to Tukey post-hoc analysis (7.13, 99 %-CI[5.96, 8.30] and 6.90, 99 %-CI[5.73, 8.07]). Most importantly, this CA approached the desired 90 deg and was not significantly different from the CA of the O_2 + PP treated surfaces (Tukey post-hoc analysis, $p = 0.93$, 0.40, 99 % - CI[-0.77, 1.57]). The SD was further reduced indicating that the air + PP plasma treatment was even more reproducible compared to the O_2 + PP plasma treatment.

Both, the O_2 + PP and air + PP plasma treated samples were not significantly different from the HCl control sample (Tukey post-hoc analysis, $p = 0.60$, 0.61, 99 % - CI[-0.57, 1.78] and $p = 1.00$, 0.21, 99 % - CI[-0.97, 1.38]). For an overview of all significance parameters, see Appendix A.1. An overview over the CAs achieved with the different plasma treatments is shown in Table 1.3 and more detailed in Appendix A.2.

Overall, the observation that the plasma activation was more efficient with an increase in N_2 content in the plasma (O_2 < air < N_2) was not unexpected since literature reports suggested that N_2 plasma treatments generated higher amounts of surface silanols compared to O_2 plasma [26]. However, in these reports, no TE was used. Since O_2 and N_2 plasma both do not contain hydrogen species suited to hydroxylate surfaces, it is assumed, that the exposure of the plasma treated, reactive surface to the ambient air after treatment causes silanol formation [26].

Initially, I suspected that the increased activation potential introduced by the PP holders was due to the introduction of hydrocarbons. During plasma decomposition of hydrocarbons a variety of hydrogen containing reactive species are generated [126, 127].
These species could potentially donate hydrogen or hydroxy groups for an improved surface activation. However, I could not achieve the same improved results using inexpensive or recycled PP labware or pure PP plates. Comparing the appearance of the O_2 plasma treated PP holder and random PP parts, the glass infused PP holder became visibly and increasingly porous, most likely due to the infused glass, while the surface of the random PP parts remained smooth. Possibly, the increased PP surface due to the surface roughening of the sample holder played a key role in creating enough hydroxylating species. Another possibility could be that the PP holder contained unknown supplements that were benefitial for the surface activation.

Table 1.3.: Contact angles (CAs) of differently plasma-activated glass surfaces after HMDS silanization. CAs of N droplets were acquired for 5–7 different batches per method. All CAs were zero before HMDS treatment. Mean ± SD (N).

Plasma	**CA (deg)**	No. of Batches
HCl	86.9 ± 3.6 (432)	6
O_2	78.2 ± 1.7 (360)	5
air	80.0 ± 2.1 (432)	6
O_2 + TE	74.6 ± 11.1 (494)	7
air + TE	80.2 ± 3.0 (432)	6
N_2 + TE	82.5 ± 2.2 (432)	6
O_2 + PP	87.5 ± 3.1 (432)	6
air + PP	87.1 ± 2.5 (432)	6

Overall, the surface activation with conventional plasma treatments was not sufficient to achieve CAs approaching 90 deg after HMDS silanization. However, significantly improved CAs approaching 90 deg could be reliably achieved after HMDS silanization using glass infused PP holders during either O_2 or air plasma activations.

1.4.1.4. XPS spectra showed the chemical composition of the activated surfaces

To gain insight into the chemical composition of the surface before and after the air + PP plasma treatment, we performed x-ray photoelectron spectroscopy (XPS) measurements (Fig. 1.12). A control measurement of the cleaned glass surface without any plasma treatment (black) gave insight into the chemical composition of the glass. The composition remained almost unchanged upon treatment with air + TE plasma (cyan) or air + PP plasma (magenta, all superimposed for highlighting the similarities and differences in Fig. 1.12B). The main peaks visible are from left to right the Si 2s, Si 2p, Na KLL, C 1s, K 2p, Ti 2p, O 1s, F KLL, F 1s, O KLL, Zn 2p and Na 1s peaks. The binding energy of these elements reflects their chemical environment. The binding energies appeared to be almost unaffected by the plasma treatments.

The Si 2p and O 1s peaks of the air + TE and air + PP plasma activated surfaces appeared slightly shifted compared to the untreated sample (Fig. 1.12B left and middle). Such changes of the Si 2p and O 1s peak position may indicate a change in siloxane/silanol ratios. For a surface hydroxylation, positive shifts of up to 0.6 eV can be expected [128]. To investigate these peaks, detailed spectra were recorded (Fig. 1.12B left and middle) and the peak center was determined using Gaussian fits (see Appendix A.3). The location of the Si 2p and O 1s peaks of the untreated glass surface was at 102.5 ± 0.1 eV and 532.0 ± 0.1 eV (mean ± SD of the fit), respectively. In comparison, the peak center shifted by 0.2 eV for both plasma treated surfaces. As charging effects of the glass surfaces were corrected by normalizing the spectrum to the Si 2p and C 1s peaks and since the shift was small, it may not be significant. A possible explanation for the small shift could be that the untreated surfaces were already more hydroxylated than expected due to cleaning

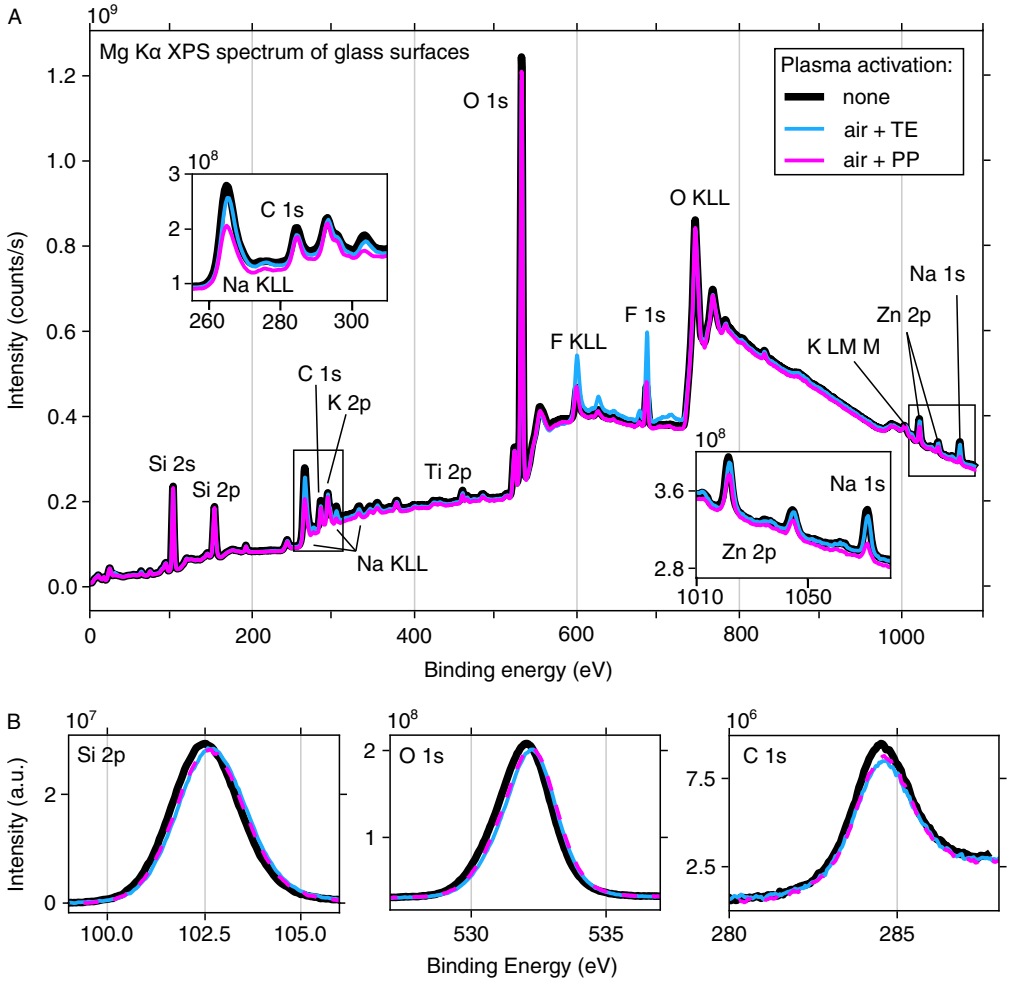

Figure 1.12.: (**A**) XPS spectra of an untreated (thick black line), air + TE plasma (light blue line) and an air + PP plasma treated (magenta line) glass surface. The elements attributed to the respective main peaks are noted. Enlarged plots are shown for the areas outlined with a black box. (**B**) Separately recorded spectra of the Si 2p peak (left), the O 1s peak (middle) and the C 1s peak (right).

by sonication in aqueous solutions. Sonication in water has been shown to affect the hydroxylation/oxidation state of titanium dioxide and iron oxide surfaces [40, 41]. This effect is attributed to the generation of OH radicals upon sonication in pure water [41, 42] and may also affect glass surfaces. An explanation for the absence of shifted binding energies in general may be that the surface activation induced by the air + PP treated surfaces is a short-lived effect. Due to the incubation of the samples in the vacuum system overnight prior to the measurements, the effect could not be measured directly after the activation but was measured more than 12 h later.

Table 1.4.: Elemental composition of the plasma activated glass surfaces. Noticeably different values are highlighted with bold text. The analyzed peaks were O 1s, Si 2p, C 1s, F 1s, K 2s, Na 1s, Ti 2p, Zn 2p, respectively.

	Elemental composition (%)							
Plasma	**O**	**Si**	**C**	**F**	**K**	**Na**	**Ti**	**Zn**
none	53.8	31.7	7.4	3.5	2.0	0.7	0.4	0.5
air + TE	49.7	31.6	6.6	**8.5**	2.1	0.6	0.4	0.4
air + PP	52.5	33.0	6.9	4.6	2.0	**0.2**	0.3	0.3

To determine the elemental composition, the O 1s, Si 2p, C 1s, F 1s, K 2s, Na 1s, Ti 2p and Zn 2p peaks were integrated and weighed according to their sensitivities. The resulting atomic percentages are listed in Table 1.4. For a borosilicate glass, a high boron content was expected [129] but not observed. The presence of low amounts of carbon in all three samples can be attributed to the air exposure before introduction to the XPS chambers [120]. The carbon amount remained low for the slides exposed to air plasma decomposed PP (Fig. 1.12B, right) suggesting that no incompletely degraded PP polymers were deposited on the surface. Only two noticeable changes in the chemical composition were observed (Table 1.4): first, the air + TE plasma treated surface had an increased fluorine content of 8.5 %, compared to the untreated and air + PP plasma treated surfaces with 3.5 % and 4.6 %, respectively. This increase was most likely due to the TE sample holder used during the air plasma treatment. Note that the different fluorine contents did not influence the contact angles noticeably as all surfaces were superhydrophilic after these plasma treatments. Second, the sodium content was reduced threefold when using the PP holder. Possibly, sodium enclosed in the glass network is extracted by the plasma.

Overall, the chemical composition of the glass surfaces barely changed upon the different treatments. Short-lived effects could not be measured. Interestingly, the air + PP plasma treatment seemed to cause a decreased sodium content. Possibly, the removal of sodium from the surface with the air + PP plasma activation made more chemical bonds accessible for surface functionalization. Alternatively, the usage of TE holders may not be optimal. In principle, the presence of hydrophobic fluorine groups at the surface may be beneficial to create a hydrophobic surface. However, since single fluorine atoms are sterically smaller than methyl groups [130], the may be too short to come in contact with the water surface. While the reason for an improved surface activation with air + PP plasma remains unclear, the measurements were excellent controls suggesting that this treatment did not cause major unexpected chemical modifications.

1.4.1.5. Plasma activated surfaces were suitable for kinesin stepping assays

To test whether the air + PP plasma activated surfaces affected kinesin assays, I measured kinesin motility parameters. Therefore, I analyzed the speed and run length for individual kinesin-1 molecules using a TIRF stepping assay performed on the air + PP

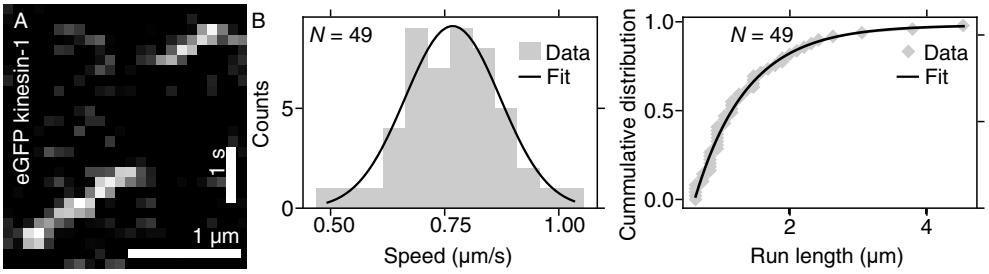

Figure 1.13.: (**A**) Kymograph showing the eGFP signal of single kinesin-1 molecules. (**B**) Multiple kymographs were analyzed to generate a histogram of the speed (left) and the cummulative distribution function of the run length (right). The data (gray) was fitted (black curves) with a Gaussian for the speed and an exponential for the run length.

plasma activated and HMDS functionalized surfaces. From recorded time series, kymographs showing the kinesin-1 translocation along a microtubule (horizontal) over time (vertical) were generated (Fig. 1.13A).

Based on the kymographs, speeds and run lengths were analyzed and represented in the histograms of Fig. 1.13B. The speed of kinesin-1 followed a Gaussian distribution and a fit yielded $y = Ae^{-(\frac{x-\mu}{2\sigma})^2} = 9.1e^{-(\frac{x-0.8}{2\cdot 0.1})^2}$. This fit suggested that the kinesin-1 speed was $0.8 \pm 0.1\,\mu$m/s (mean $\pm$ SD, $N = 49$). The cummulative distribution of the run lengths followed an exponential distribution that could be fitted with $y = -Ae^{-bx} + C = 2.2e^{-1.3x} + 1.0$. The run length was $1.4 \pm 0.8\,\mu$m (mean $\pm$ SD, $N = 49$) in average and $0.8\,\mu$m according to the fit of the cummulative distribution function. Both, speed and run length, were in good agreement with literature values [4, 131]. Thus, the air + PP plasma activated surfaces did not affect the kinesin's motility and were suited for kinesin stepping assays.

1.4.1.6. Hydrophobic surfaces with contact angles above 90 deg are not necessary or ideal for hydrophobic-interaction-based kinesin stepping assays

Having confirmed the chemical composition, quality and functionality of the surfaces prepared with plasma treatments, I investigated the influence of the CA on the performance of the hydrophobicity-based kinesin stepping assays. According to the literature, CAs above 90 deg are required for hydrophobicity-based single-molecule assays on microtubules [6, 18]. This requirement has not been systematically investigated or experimentally confirmed. To assess the "degree of hydrophobicity" required for a high-quality single-molecule assay, the assay was performed on surfaces with different CAs ranging from 28 to 93 deg using IRM and TIRF microscopy (Fig. 1.14 and 1.15).

First, I investigated the microtubule attachment without kinesins using IRM. For the same assay performed on surfaces with different CAs, I could not observe a difference visible by eye. To determine the SBR of the microtubules, 40×40 pixel ROIs (black

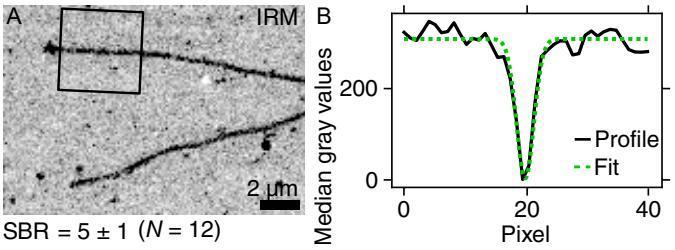

Figure 1.14.: IRM image of microtubules (**A**). Gray values (**B**) obtained by medianing the area marked as a black rectangle in **A** along the microtubule axis. Exemplary image of a surface with CA = 30 deg. SBR is stated as mean ± SD.

rectangle in Fig. 1.14A) containing straight microtubule segments were chosen and converted to median gray value line profiles perpendicular to the microtubule (Fig. 1.14B). A Gaussian fit of the line profile was used to extract the microtubule signal and determine the residual noise (Fig. 1.14B, see Methods Sect. 1.3.7.2). Without kinesins, the SBR of the microtubules was unaffected by the "degree of hydrophobicity". Stably attached microtubules with the same SBR of 5 ± 1 deg (mean ± SD, $N_{seg} = 16$ and $N_{seg} = 12$ for CAs of 30 deg and 90 deg, respectively) were observed irrespective of the CA. Note that a CA of 30 deg is comparable to the that of an unfunctionalized glass slide but was obtained by an inefficient TMCS silanization procedure.

In contrast, when kinesin in its motility buffer was added, surfaces with a higher CA performed better (Fig. 1.15). With lower CAs, microtubules loosened and unspecific interactions between kinesins and the surface increased. Microtubule loosening, unspecific kinesin interactions with the surface and specific interactions with microtubules were observed by imaging the enhanced green fluorescent protein (eGFP) tags of the kinesin-1 molecules using TIRFM (Fig. 1.15A). Nonspecific kinesin-surface interactions were investigated by calculating the mean pixel intensity of the microtubule-free background and will further be referred to as "background". Specific kinesin-microtubule interactions were quantified by determining the maximum intensity of an average line profile calculated from microtubule segments and will further be referred to as "signal". The SBR was calculated as the ratio of the "signal" and the "background". Ideally, kinesins should specifically interact with the microtubules and not with the surface, resulting in a high SBR. The number of straight microtubules segments N_{seg} and background areas N_{bkg} used for the SBR analysis are not related to the total number of microtubule ends N_{end} observed within a sample to assess the microtubule attachment. Microtubules with attached ends but loose middle parts were included in the calculations by counting the loose middle parts as loose ends. All kinesin assays were performed on the same day with exactly the same buffer and kinesin dilution (5 nM).

For the lowest CA of 28 deg, frequent unspecific interactions of the kinesins with the surface were observed, resulting in a high background of 14.0 ± 3.0 (mean ± SD, $N_{bkg} = 16$). Kinesins colocalized with the microtubules, resulting in a signal of 47.9 ± 7.1 (mean ± SD, $N_{seg} = 7$). Despite the resulting low SBR of 3.5 ± 0.9, the microtubules were still visi-

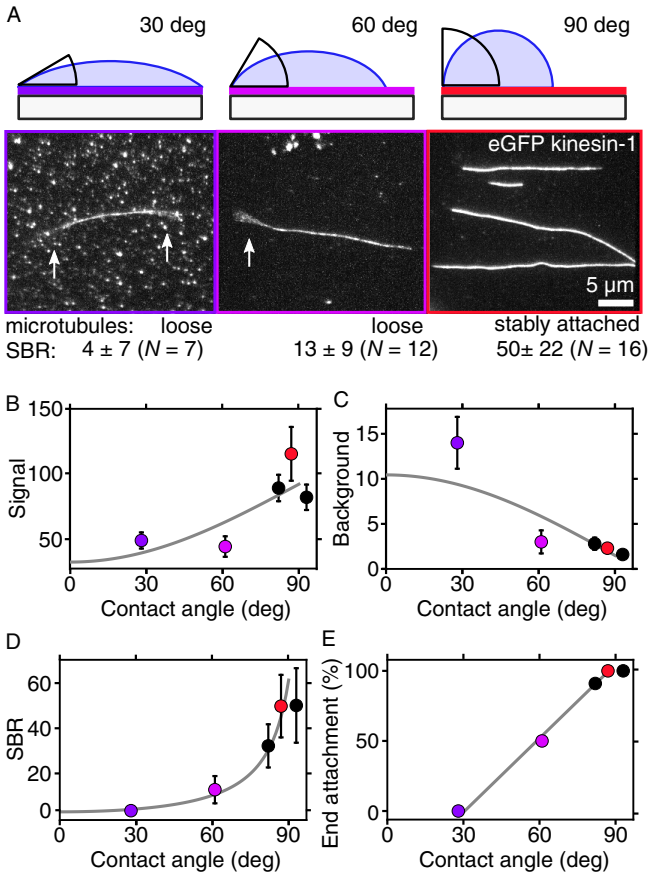

Figure 1.15.: (**A**) Maximum intensity projections (time series of 100 images per projection) of kinesin-1 decorated microtubules in TIRF. These assays were performed using surfaces with water CAs of 30 (violet), 60 (pink) and 90 (red) deg. White arrows indicate loose microtubule ends. SBRs are stated as mean ± SD. Data points indicate the signal of kinesin-decorated microtubules (**B**), the background decorated with unspecifically interacting kinesins (**C**), the resulting SBR (**D**) and end attachment percentages (**E**) as a function of the CA. Fits (gray lines) are either based on the model underlying Eq. **??** (**B**-**D**) or linear (**E**). The color scheme specified in **A** applies to the data points. Black data points are additional measurements not shown in **A**.

ble (Fig. 1.15A-D). Furthermore, microtubules were not attached stably anymore. All microtubule ends were loose ($N_{end} = 10$), resulting in a microtubule end attachment of 0 % (Fig. 1.15E). Loose ends are indicated with white arrows in Fig. 1.15A. For CAs of 61 deg, 50 % of the microtubule ends were attached ($N_{ends} = 18$). While the microtubule signal remained comparable to the previous sample (signal of 43.2 ± 8.8, mean ± SD, $N_{seg} = 12$), there was a visible reduction in unspecific interactions between kinesins and the surface (background of 3.0 ± 1.4, mean ± SD, $N_{bkg} = 16$). Accordingly, the SBR increased to 12.8 ± 6.5.

Interestingly, the transition to a high-quality assay was observed between 80 deg and 90 deg and not above 90 deg as suggested previously [6, 18]. Therefore, these CAs were investigated in more detail. Assays performed on surfaces with a CA of 82 deg had an increased microtubule signal of 88.6 ± 11.1 (mean ± SD, $N_{seg} = 16$) and a background of 2.8 ± 0.8 (mean ± SD, $N_{bkg} = 16$). The resulting SBR of 32.2 ± 10.0 was further increased. With 90 % ($N_{ends} = 56$), most of the microtubule ends were attached. For CAs of 87 deg, the signal was maximal with 115.1 ± 21.7 (mean ± SD, $N_{seg} = 16$) while the background

decreased to 2.3 ± 0.5 (mean $\pm$ SD, $N_{bkg} = 16$). Accordingly, the SBR further increased to 49.8 ± 14.3. Additionally, all microtubule ends were attached (100 %, $N_{ends} = 46$). For a CA of 93 deg, a reduced microtubule signal of 81.4 ± 10.7 (mean $\pm$ SD, $N_{seg} = 16$) was observed. The background further decreased to 1.6 ± 0.5 (mean $\pm$ SD, $N_{bkg} = 16$). Interestingly, the resulting SBR of 50.1 ± 17.0 was not significantly different ($t(30) = 1.7$, $p = 0.1$, $\alpha = 0.05$) from the SBR of the 87 deg sample. Furthermore, the microtubule end attachment of 100 % ($N_{ends} = 40$) was achieved as well. An overview of the signal, background, SBR and end attachment data is shown in Table 1.5.

The "signal", "background" and SBR data was simultaneously fitted with shared variables (gray line in Fig. 1.15B-D) with the functions underlying the model described in Sect. 1.3.7.6. According to this fit, a F-127 passivated surface with a CA of about 0 deg would offer a minimal SBR of about 3.0 and 65 % of the total amount of kinesins available in the assay would bind to the surface. Since the underlying model is just a rough simplification, the exact numbers should be considered with care and the gray slopes in Fig. 1.15B-D should rather be considered as guides to the eye. However, this rough calculation may illustrate and reinforce the importance of the CA for passivation of the surface against unspecific kinesin binding.

Interestingly, the microtubule end attachment alone was not influenced by the CAs (Fig. 1.14), but the addition of the kinesin motility assay induced a linear dependence ($y = mx + c$ with $m = 1.76 \pm 0.03$ and $c = -53.62 \pm 2.38$) of the microtubule attachment on the CA (Fig. 1.15C). One explanation may be that the Pluronic F-127 polymer brush is only formed on surfaces with CAs above 80 deg [115]. A proper F-127 polymer brush may be required to protect antibody-surface attachment sites from other proteins that compete for the surface attachment with the antibody. Furthermore, the F-127 brush thickness was reported to increase with the CA at least up to 9 nm at ≈ 100 deg [115]. Thus, the polymer brush has a dimension comparable to the size of antibodies used to attach the microtubules [90, 132]. Accordingly, a polymer brush with an increased thickness may prevent kinesins from binding to the lower side of the microtubule and potentially even push the microtubule further away from the surface. Less densely decorated microtubules or kinesins that are further away from the TIRF field may explain the decreased microtubule signal observed at 93 deg. An improved passivation property

Table 1.5.: Average gray values of the signal of kinesin decorated microtubules (S), background fluorescence (B) caused by kinesins nonspecifically interacting with the surface and the resulting SBR in dependence on the CA. Means $\pm$ SD (N). The end-attachment percentages (EA) are shown below.

CA	**28**	**61**	**82**	**87**	**93**
S	47.9 ± 7.1 (7)	43.2 ± 8.8 (12)	88.6 ± 11.1 (16)	115.1 ± 21.7 (16)	81.4 ± 10.7 (16)
B	14.0 ± 3.0 (16)	3.0 ± 1.4 (16)	2.8 ± 0.8 (16)	2.3 ± 0.5 (16)	1.6 ± 0.5 (16)
SBR	3.5 ± 0.9	12.8 ± 6.5	32.2 ± 10.0	49.8 ± 14.3	50.1 ± 17.0
EA	0 % (10)	50 % (18)	90 % (56)	100 % (46)	100 % (40)

of the thicker (and denser) polymer brushes may explain the decreased background. While the exact numbers may be considered with caution due to the low statistics, the observed SBRs and microtubules attachments clearly show that CAs above 90 deg are not required to obtain high-quality single-molecule assays. Potentially, the surfaces at 87 deg may be even optimal due to showing the highest microtubule signal.

1.4.2. Improved label-free IRM contrast can partially be achieved for APTES-based microtubule assays

To investigate, whether the SBR of microtubules visualized in IRM can be further improved by the choice of the assay, I compared the hydrophobic interaction-based microtubule attachment with electrostatic microtubule attachment. The relevant difference between these two methods is the expected height of the microtubule above the glass surface. This height difference is expected to affect the IRM contrast of a microtubule (see Theory Sect. 1.2.5.2). The highest contrast results if microtubules are in direct contact with the surface [101]. Using the glass surface as a reference ($d_{glass} = 0$, Fig. 1.16A), the height of the negatively charged microtubule above a the negatively charged glass surface should, among other effects, depend on the electrostatic screening of the buffer. With a Debye length λ_D of about 1 nm [133], a high contrast is expected.

A comparable or smaller distance to the surface and thus similar or higher contrast would be expected for a microtubule attached to a monolayer of silane ($d_S \ll 1$ nm based on the chemical structure). A reduced contrast would be expected for a microtubule attached to the surface via an antibody (vertically oriented antibody $d_{ABv} \approx 15$ nm , horizontally oriented antibody $d_{ABv} \approx 7$ nm based on the crystallographic structure [90, 132], Fig. 1.16A). To test how the microtubule contrast depended on the immobilization procedure, microtubules attached via different methods were imaged with IRM and their SBRs were measured. Microtubules were either attached directly to a plasma cleaned glass surface (Fig. 1.16B), a positively charged surface generated by APTES silanization (Fig. 1.16C) or attached indirectly via antibodies to a hydrophobic surface (Fig. 1.16D) generated by the protocol optimized in Sect. 1.4.1.

Interestingly, microtubules attached by antibodies had the highest SBR of 4.6 ± 0.6 (mean $\pm$ SD, $N = 16$). In contrast, microtubules attached to an APTES surface had a SBR of 3.7 ± 1.4 (mean $\pm$ SD, $N = 18$). The corresponding IRM images showed that microtubules were rigidly attached to the APTES surface, but some microtubule parts were located at different heights. This height variation resulted in the high SD and lower average value. Therefore, the microtubule parts were assigned to three different subgroups: microtubules that were located (1) close to the surface (attached, black), (2) about 40 nm above the surface (not attached, gray) or (3) about 80 nm above the surface (not attached, white).

Next, the SBR analysis was applied to all subgroups separately. Thereby, it became apparent that the microtubule parts of groups (2) and (3) contributed to the low average

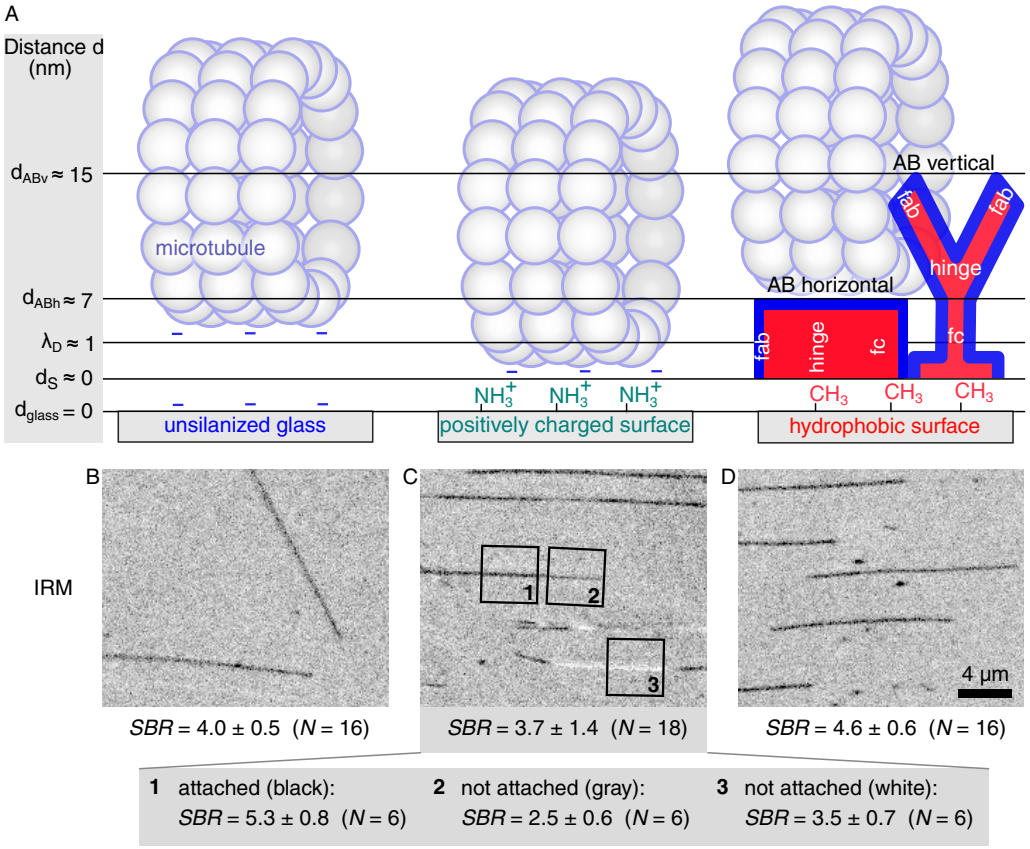

Figure 1.16.: (**A**) Schematic of expected distances from the glass surface introduced by the different surface modifications (umodified, APTES functionalized and HMDS functionalized with an antibody and F127 passivation. The antibody (AB) could potentially be oriented horizontally or vertically oriented and contains a fragment antigen binding (fab) region, sterically variable hinge region and a fragment crystallizable (fc) region. Figure is not drawn to scale. IRM images of microtubules bound to unmodified (**B**), APTES functionalized (**C**) or HMDS functionalized and antibody and F127 treated glass surfaces. The respective SBRs are indicated below as mean ± SD.

SBR value with SBRs of 2.5 ± 0.6 (mean ± SD, $N = 6$) and 3.5 ± 0.7 (mean ± SD, $N = 6$, Fig. 1.16 grey box at the bottom), respectively. Microtubule parts of group (1) showed a SBR of 5.3 ± 0.8 (mean ± SD, $N = 6$) that was significantly higher compared to the antibody-based assay (students unpaired t-test, $t(20) = 2.2299$, $p = 0.0374$).

To correlate the SBRs with the height of the microtubule above the surface, several assumptions were made: First, the microtubule was considered as the sum of multiple tubulins at different heights, resulting in an IRM signal that corresponded approximately to the central axis of the microtubule. Therefore, it was assumed that the highest SBR of microtubules directly attached to an APTES surface of $5.3 + 0.8 = 6.1$(mean + SD)

effectively corresponded to the height h_c of the radius of the microtubule above the surface at $h_c = 12.5\,\text{nm}$. Thus, this height was used to numerically calculate the amplitude A according to [101]:

$$SBR_{corrected} = A \times \frac{\sin\left(2kh\sin^2\left(\alpha/2\right)\right)}{2kh\sin^2\left(\alpha/2\right)} \cos\left(\frac{4\pi n_1 h}{\lambda}(1-\sin\alpha/2)\right) \tag{1.19}$$

Using $\alpha = \arcsin\left(INA/n_1\right)$, $k = 2\pi n_1/\lambda$, $\lambda = 450\,\text{nm}$, $INA = 1.15$ and $n_1 = 1.33$ [101], an amplitude of $A \approx 6.5$ was calculated. This amplitude was used to determine all further heights h (Fig. 1.17A). To determine the error propagation, upper and lower limits were calculated by adding or subtracting the SDs from the mean SBRs, respectively. For these upper and lower limits of the SBR values, the heights were calculated and assigned to error intervals. The calculated heights corresponded to the distance between the glass surface and the microtubule center. To obtain the distances between glass surface and microtubule surface as in Fig. 1.16, the microtubule radius was subtracted. The resulting heights of the microtubule above the glass surfaces are shown in Fig. 1.17B. Accordingly, the microtubules were located above the surface at a height h of $9.3\,^{+6.7}_{-9.3}\,\text{nm}$ (mean $\pm$ SD, $N = 6$) when attached to APTES, $15.3\,^{+4.3}_{-5.1}\,\text{nm}$ (mean $\pm$ SD, $N = 6$) when attached via antibodies and $19.6\,^{+3.4}_{-3.6}\,\text{nm}$ (mean $\pm$ SD, $N = 6$) when located at a bare glass surface. The large errors of these values suggested the presence of bent microtubules located at different heights above the surface. Especially for the APTES-bound microtubules, which appeared to vary in heights in the IRM images and therefore were categorized in groups (1)-(3), this vertical bending appeared very likely. Interestingly, the height of the antibody-attached microtubules was with 15.3 nm as expected from theory for a vertically oriented antibody (Fig. 1.16A, [90,132]). Considering the corresponding errors, it appeared likely that the majority of the microtubule-bound antibodies was oriented vertically while some were oriented horizontally. Additionally, the sterically variable hinge region of the antibody (Fig. 1.16A) most likely contributed to height variations. The attachment of the microtubule to antibodies at different heights potentially caused a microtubule bending and the observed errors. Above average antibody heights and microtubule bending may be responsible for microtubule heights above the average value. The low SBR of the microtubules located at a bare glass surface did correspond to a height of about 20 nm above the surface. This distance was unexpectedly high, as the Debye length calculated for PEM buffer was $\lambda_D = 1\,\text{nm}$ [133]. However, the Debye length is only valid for small surface potentials below 20 mV [134]. The zeta potential of a conventional glass surface is 60 mV at neutral pH [135] and surface charges are expected to be about $2000\,\text{e}/\mu m^2$ [136]. For microtubule surfaces (covered by the negatively charged E-hooks), charge densities between 280 and $32{,}000\,\text{e}/\mu m$ have been reported [137]. Therefore, the electrostatic interaction between the two highly negatively charged surfaces may not be predictable with the Debye length and a longer range of the electrostatic repulsion between microtubule and glass surface may be expected. An additional effect that most likely contributed to all of the measured data and error bars could have been a limited precision in the focus positions. Overall, microtubules had a high and homogeneous contrast when attached via antibodies. On the contrary, the contrast and SBR was less homogeneous but partially increased for APTES-attached microtubules.

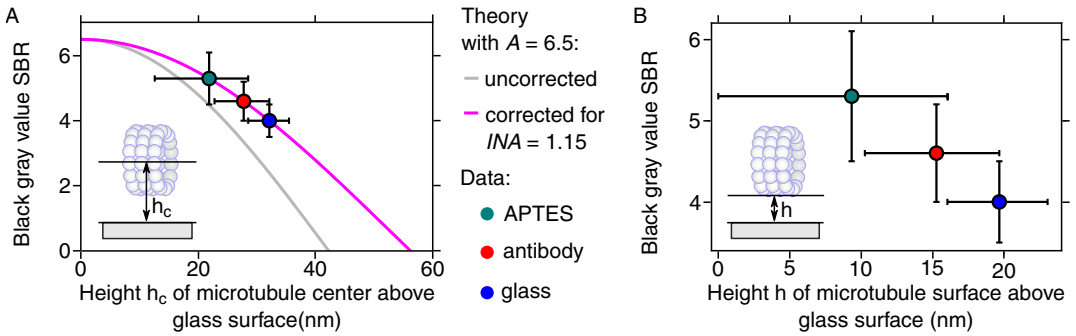

Figure 1.17.: (**A**) Signal-to-background ratio *vs* height. The INA corrected (magenta) heights were assumed to correspond to the distance between glass surface and microtubule center. (**B**) Distances between glass and microtubule surfaces obtained from (**A**). Microtubules were either attached via APTES (cyan), antibodies (red) or loosely located at a bare glass (blue).

A correlation of the SBR with height suggested that the microtubule-surface distance was partially reduced for microtubules attached via APTES compared to antibody-attachment. Thus, electrostatic microtubule attachment via APTES surfaces might be suitable for measurements requiring higher SBR ratios.

1.5. Conclusion & Outlook

To achieve a more reproducible surface hydrophobization procedure, cleaning and surface hydroxylation methods were investigated and different silanes were compared. A combination of a vapour-phase hexamethyldisilazane treatment with a new plasma-based activation procedure using PP holders performed best. While O_2, air, $O_2 + TE$, $N_2 + TE$ and air + TE plasma treatments did not activate the surfaces sufficiently, the introduction of the glass infused polypropylene holder into O_2 or air plasma improved the activation significantly. After HMDS silanizations, $O_2 + PP$ or air + PP activated surfaces had the desired CAs approaching 90 deg. XPS control measurements showed that no unexpected surface modification occurred due to the air + PP treatment. Since XPS measurements could not be performed immediately after the activation procedure, it remains an open question whether to us unknown short-lived effects occured and improved the activation efficiency. In the future, it would be interesting to further investigate the mechanisms of plasma activation in general to create a better understanding of the processes and the activated surface. It would be interesting to understand what components of the PP holder improved the results significantly. An analysis of the chemical composition of the PP holder would be required to confirm if it is composed of glass and polypropylene as specified. Kinesin-single-molecule analysis further confirmed that the functionality of the kinesin remained intact when moving on the optimized surfaces. Furthermore, TIRF analysis of kinesin stepping assays performed on surfaces with various CAs showed that the SBR and the microtubule attachment depended on the CA. Interestingly, hydropho-

bic surfaces with a CA above 90 deg were not required as stated in the literature [18]. CAs of about 87 deg were not only sufficient but possibly also optimal due to a high signal combined with a high SBR. Importantly, the presented methods enable the preparation of optimal and reliable surfaces while additionally reducing chemical consumption, waste production and work effort to a minimum. Compared to the original protocol requiring almost a full day of active work, surfaces can now be prepared more reliably, with higher quality, and require only 30 minutes of active work. The incubation with HMDS over the weekend can most likely be replaced by a vacuum silanization procedure which would require an additional active work time of several minutes up to 30 min. However, with adequate planning of experiments, this extra work effort is not necessary. Furthermore, the IRM signal of microtubules attached via different methods to glass surfaces was investigated and correlated to surface-microtubule distances. While the expected SBR dependence on height was not observed for average values, a closer look at the black microtubule areas of APTES attached microtubules showed that these areas were partially located closer at the surface compared to antibody-attached microtubules. Nevertheless, the data analysis suggested an average microtubule-surface distance of 10 nm for the black microtubule areas on APTES surfaces, suggesting that microtubules were also bent upwards at areas visually appearing "attached". In contrast, antibody-attached microtubules showed a more homogeneous average SBR that corresponded to a height of 15 nm. This height was in agreement with the size of an antibody and suggested, that antibodies attached mainly in a vertical orientation to the hydrophobic surfaces. Overall, the antibody-based microtubule assay was optimized and appeared—in its optimized form—more suited for kinesin single-molecule assays in TIRF and IRM. Nevertheless, the IRM contrast of a microtubule could be partially enhanced using APTES surfaces. Such a high contrast might be beneficial especially for highly sensitive iSCAT measurements in the future.

2. A custom-written camera program for real-time iSCAT imaging and simultaneous IRM detection

2.1. Introduction

For optimized IRM, the contrast is sufficient to monitor microtubule dynamics label-free, in real-time with an end tracking length precision of about 20 nm [102]. Tracking the shrinkage and growth of microtubules can be used to indirectly study the behaviour of kinesins [18, 138, 139]. However, to directly observe single kinesins in IRM, a labeling with strong scattering nanoparticles is currently required [140]. Alternatively, IRM can be combined with TIRFM to study fluorescently labeled kinesins [141]. All labeling techniques have the common disadvantage, that the proteins cannot be studied in their native state. A relatively new microscopy approach first reported in 2004 [142, 143] that enables the label-free optical detection of single proteins as small as 19 kDa is interferometric scattering (iSCAT) microscopy, also called mass photometry [144]. The technique is essentially the same as IRM but uses a different light source and image processing. In principle using iSCAT, the translocation of single kinesins (100 kDa [145]) can potentially be monitored label-free and in real-time in the near future. However, so far only the tracking of nanoparticles coupled to single kinesins in iSCAT has been reported [146]. iSCAT illumination is based on laser light. The field of view is typically a few micron small or if larger, requires laser scanning [143]. The reflected and interfering light is collected by a camera comparable to IRM. iSCAT images achieve their highly improved iSCAT contrast by the higher photon flux and further data postprocessing [147]. While the individual postprocessing procedures differ, the main principle of iSCAT processing is to remove any static background. In this manner, only dynamic signals are visualized [144, 147, 148], for example moving samples or binding and desorption events. As the images are postprocessed after the measurement, experiments are often performed "blindly". The contrast of small absorbing proteins may not stand out from the roughness of the glass surface or other sample features while the raw data is collected. To enable the direct observation with iSCAT contrast in real-time, I included the iSCAT post-processing in a custom-written and high-speed-optimized imaging program enabling the simultaneous usage of IRM and iSCAT.

2.2. Materials & Methods

2.2.1. Optical setup

The optical design of the microscope was realized within three separate master's theses [149–151]. The overall design of the microscope was developed by Steve Simmert, Anita Jannasch and Erik Schäffer. All optical components were purchased from Qioptiq (Göttingen, DE) unless noted otherwise. Instead of the laser illumination conventionally used for iSCAT, a superluminescent light emitting diode (sLED, EXS210014-01, EXALOS AG, Schlieren, CH) with a wavelength of $\lambda = 450 \pm 15\,\mathrm{nm}$ was implemented (Fig. 2.1). The sLED light was collected with lens L_1 and focused through an aperture iris AI. Lens L_3 parallelized the beam and enabled the placement of a half-wave plate ($\frac{\lambda}{2}$, WPH05M-445, Thorlabs, US) and a field iris FI. The beam was redirected by two mirrors M_1 and M_2 and the lens L_4 focused the beam in the back focal plane (BFP) of the objective (CFI S Fluor 100x oil, Nikon, JP), while passing a polarizing beamsplitter (PBS, CCM1-PBS251/M, Thorlabs, US), a quarter-wave plate ($\frac{\lambda}{4}$, WPQ10M-445, Thorlabs, US) and mirror M_3. In this manner, Köhler illumination was achieved. The wave plates were oriented such, that transmission and reflection by the PBS were maximized. The light reflected by the sample was redirected by mirror M_3 through the quarter-wave plate and the PBS to mirror M_4. M_4 directed the transmitted light through lenses L_5-L_7. These lenses magnified the image onto the CMOS camera (MV1-D1024E-160-CL, Photonfocus AG, Lachen, CH). The optical setup was mounted on an optical table

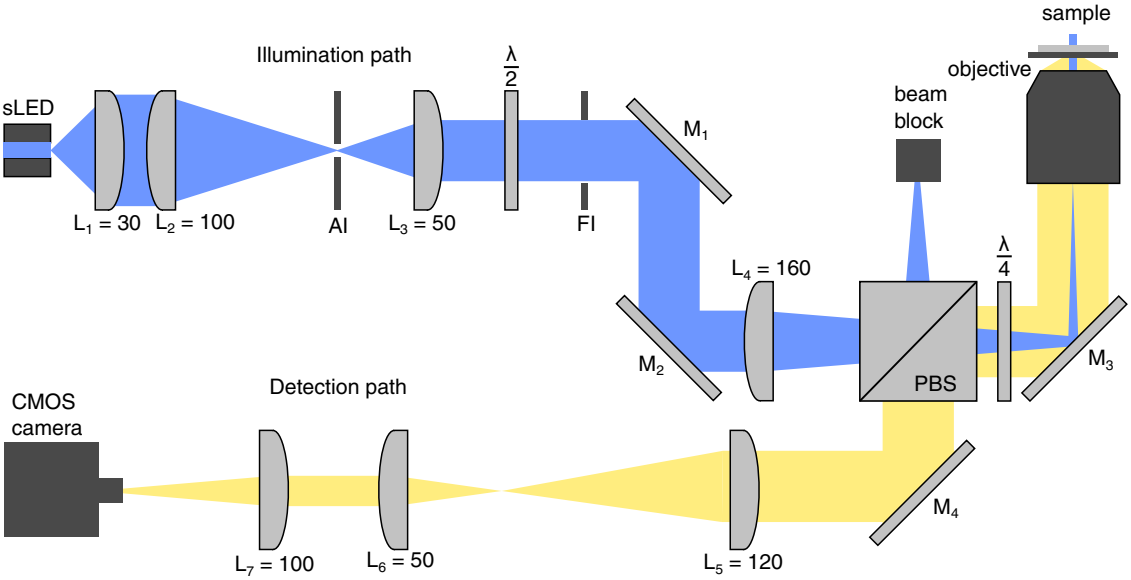

Figure 2.1.: Optical setup of the iSCAT capable IRM microscope. An sLED is used for Köhler illumination of the sample. The reflected light is focused on a CMOS camera for detection. Lenses L_i are stated with focal distances in mm. Distances are not drawn to scale.

(Opto-mechanics table 1HB, Standa Ltd., Vilnius, LT) isolated from vibrations by a custom-built damping system similar to the one described in [152].

2.2.2. System control

The high-speed CMOS camera was connected via a camera link base to a NI PXIe 1435 frame grabber. The frame grabber was compatible with a NI PXI 1073 box that was connected via PCIe to the PC. The software PFRemote, provided by the manufacturer, was used to connect to the NI frame grabber and control the camera interface. With the NI driver IMAQdx, data acquisition was performed in the custom-written camera program (camera.vi) in Labview 2017. For an improved background image creation, the stage translocation upon image collection was automated. The camera.vi was able to interact with another custom-written program that generated random steps and communicated the step information via VISA drivers over a COM port to the Mechonics stage control. To control the power of the USB connected light source, DAQmx drivers were used to change the power within a Labview program (LED.vi). All further steps were performed within a master's thesis by Tom Stumpp [149] and are therefore written with gray text in Fig. 2.2. The sLED was connected to an EXALOS driver board (EBD 7000, EXALOS AG, Schlieren, Switzerland). The EXALOS driver obtained power from a DC power supply (E3648A, Agilent, Santa Clara, US) and was connected to a Labview-controllable USB module (Multi-channel data acquisition module USB-621, National Instruments, US). For an improved heat dissipation, the sLED was mounted on a heat sink (SK46, Fischer Elektronik, Lüdenscheidt, DE) and for additional active cooling, a thermo-electric cooler (TEC, TECD2S, Thorlabs, US) was added. The PID temperature feedback control of the TEC element was mediated by a micro controller board (Arduino Uno Rev 3, Arduino, US) and a corresponding Arduino 1.8.13 software written by Ganesh Sanal.

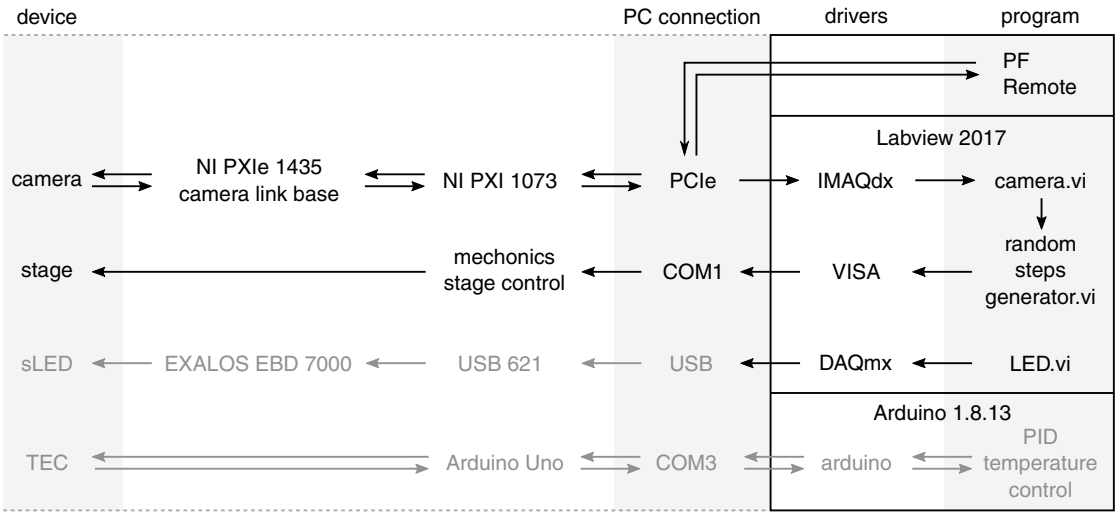

Figure 2.2.: Schematic overview of the hardware-software control.

2.2.3. IRM processing

To account for inhomogenous illumination, a median background image Med_{Back} was generated. To prevent static sample features from being considered as background, the sample was moved automatically with the stage while raw image frames $f_{raw,1}$ - $f_{raw,L}$ were collected (Fig. 2.3).

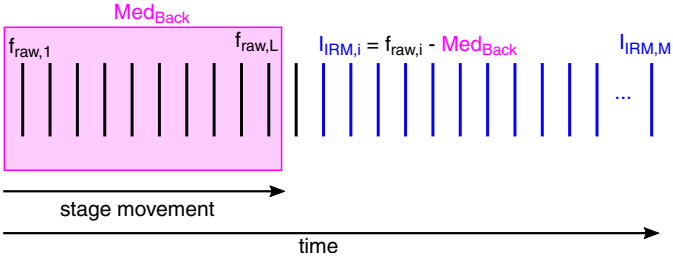

Figure 2.3.: For IRM processing, raw image frames $f_{raw,1} - f_{raw,L}$ (black) were collected while the stage was moved. From these frames, a median background image Med_{Back} (magenta) was generated. Afterwards, IRM images $I_{IRM,i}$ (blue) were obtained by subtracting the background from the raw image frames.

The background image was created once in advance to imaging. During imaging, Med_{Back} was subtracted from every raw image frame $f_{raw,i}$ to generate the processed IRM image $I_{IRM,i}$:

$$I_{IRM,i} = f_{raw,i} - Med_{Back} \tag{2.1}$$

2.2.4. iSCAT processing

While the IRM image processing was based on an experimentally motivated, simple background subtraction, iSCAT processing was motivated by Eq. 2.2 [148]

$$I_{det} = |E_{inc}|^2(r^2 + |s|^2 + 2r|s|\cos\phi), \tag{2.2}$$

with the incident electric field E_{inc}, the reflectivity of the sample or interface r^2, the scattering amplitude of the object s and the phase difference between scattered and reflected light ϕ. Since $|s|^2$ is negligible for weak scatterers, Eq. 2.3 can be rewritten to

$$\frac{I_{det}}{I_{bkg}} = 1 + \frac{2|s|\cos\phi}{r}, \tag{2.3}$$

with $|E_{inc}|^2 \cdot r^2$ as the background intensity I_{bkg}. Eq. 2.3 defines the iSCAT contrast according to Ref. [148]. Such a ratiometric calculation of the iSCAT contrast can be realized in a static or dynamic fashion. Since iSCAT imaging resolves the roughness of the samples's glass surface, even small changes in the sample position require to be corrected. Therefore, the removal of static sample features with a background image created in advance is not sufficient. A dynamic approach using a constantly updated background image is favourable [142, 144, 148].

The dynamic iSCAT contrast was realized as described in Ref. [148]. There, the median image Med_{Back} used for the static background correction of the IRM image was also used for iSCAT imaging. The raw image frames $f_{raw,i}$ were divided by Med_{Back} to generate the frames entering the iSCAT processing $f_{iSCAT,i}$:

$$f_{iSCAT,i} = \frac{f_{raw,i}}{Med_{Back}} \tag{2.4}$$

The resulting frames $f_{iSCAT,i}$ were then used to generate two running averages Av_k and Av_{k+1}. To account for fluctuations in the illumination intensity, each of the running averages was normalized to its average pixel intensity I_{AvPx}:

$$Av_k = \frac{1}{I_{AvPx,k}(Z+1)} \sum_{i}^{i+Z} f_{iSCAT,i} \tag{2.5}$$

$$Av_{k+1} = \frac{1}{I_{AvPx,k+1}(Z+1)} \sum_{i+1+Z}^{i+1+2Z} f_{iSCAT,i} \tag{2.6}$$

These running averages move with the index i through the image stack $f_{iSCAT,1} - f_{iSCAT,M}$ collected over time (Fig. 2.4A) and are combined through division for the generation of a ratiometric iSCAT image $I_{iSCAT,k}$:

$$I_{iSCAT,k+1} = \frac{Av_{k+1}}{Av_k} \tag{2.7}$$

Upon generation of the ratiometric image, the median background image accounted for in Eq. 2.4 cancels out. Eq. 2.4 thus did not affect the image quality and could be omitted. The computational performance was not measurably affected by inclusion or exclusion of this step of calculation. The amount of images $(Z+1)$ used for one separate running average Av_k or Av_{k+1} will be further referred to as "running average size".

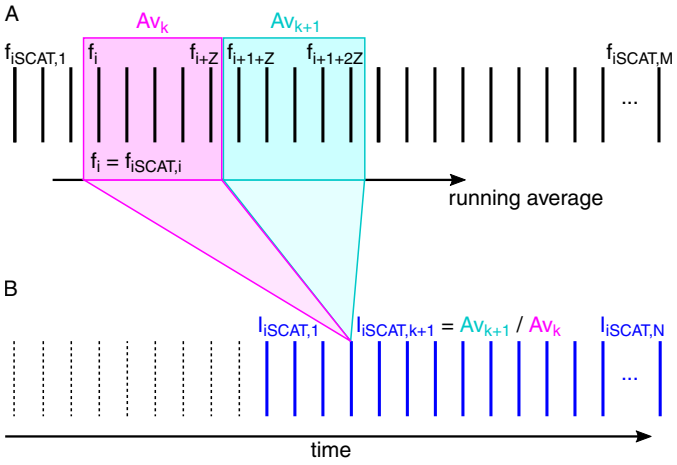

Figure 2.4.: For iSCAT processing, two running averages normalized to their respective mean pixel intensities are generated (Av_k in magenta and Av_{k+1} in cyan) and divided by each other. These running averages move through background corrected frames $f_{iSCAT,i}$ (black) over time to generate the iSCAT images ($I_{iSCAT,k}$, blue)

Implementation in Labview The realization of the IRM and iSCAT processing was realized in Labview 2017. The data acquisition was done using the IMAQdx drivers of the additional NI Vision Acquisition software package. Furthermore, basic image processing such as median or average creation or background subtraction was done using the NI Vision Utilities and Image Processing tools palette. For iSCAT processing, images were converted into arrays that prevented the loss of information stored in decimal places. To convert the decimal places to pixel values or an iSCAT contrast, a user specified factor called "iSCAT contrast" was multiplied with the resulting integer iSCAT image array. After multiplying the iSCAT image array with the as iSCAT contrast specified factor, the array was converted into unsigned 16-bit integer (U16) and reconverted into the NI Vision and Motion image format for displaying and saving the data.

2.2.5. Performance tests

To investige the performance of the camera program, four different image dimensions specified by the region of interest (ROI) sizes were chosen. The reduction of the ROI enabled faster camera frame rates. Using a ROI of 400×400 pixels, a maximal frame rate (FR_{max}) of 948 fps could be achieved, that was close to a typical iSCAT image acquisition rate of 1000 fps [144]. However, a ROI of 300×300 pixels was sufficient to image the whole field of view that was illuminated by the sLED and enabled a FR_{max} of 1648 fps. Due to illumination inhomogenities, typically ROI sizes of 200×200 or 100×100 pixels were used for imaging that enabled even faster imaging frame rates. These two smaller ROIs were operated at 2115 fps. ROI and frame rate were set to the respective dimension using the PFRemote software. The central processing unit (CPU) usage of Labview was estimated using the Windows computer system's task manager. The random access memory (RAM) usage could be monitored precisely using the Labview profile tool. While monitoring these performance parameters, different features of the program were activated consecutively. First, the acquisition loop was activated. Second, the raw image was displayed via the IRM image. Third, the IRM image was corrected by subtracting the background from the raw image and displayed via the IRM display. Fourth, the data was decimated by averaging three images. Fifth, the iSCAT mode was activated with a running average size of 6, which included data decimation and the iSCAT image display. The data decimation was adjusted to the minimal amount of decimation, at which the program still ran stably. A stably performing program could be identified monitoring the data acquisition and processing queues displayed at the user interface: queues that were constantly close to zero indicated a stably running program, while queues that grew indicated performance issues. Then, the running average size was increased to 24, 50, 100 and 200. The effective iSCAT imaging rates were calculated by dividing the acquisition frame rate of the camera by the amount of data decimation.

2.2.6. Sample preparation

For imaging loose microtubules, GMPCPP-stabilized microtubules (Sect. 1.3.5.2) were flushed into microfluidic chambers of type B (Sect. 1.3.4) built of month-old APTES-functionalized surfaces (see Sect. 1.3.3.4) that did not bind microtubles anymore.

2.2.7. Imaging using the IRM and iSCAT mode in parallel

The camera was used with PFRemote standard settings (free running, 0 strobe delay, strobe pulse width 1 ms, 12 bit resolution, 1x digital gain, 0 skimming, no simultaneous readout) except that no hardware pixel correction was performed. Imaging was performed at 948 fps within a 200×200 pixel region of interest (ROI). One pixel corresponded to a distance of 84.8 ± 0.1 nm (mean $\pm$ SEM, $N = 54$) within the sample [149]. 3 images were averaged for decimation. A median background image was created using the automated background subtraction feature (80 random 1 μm steps with 10 ms waiting time in between the steps) to translocate the stage randomly while collecting 1000 images. For the iSCAT mode, a running average number of 24 was chosen and an iSCAT contrast of 2550. The sLED was operated at 12.5 mW power at 20 °C. For the pseudocolor overlay, image grey values were inverted. IRM images were displayed in green and iSCAT images in magenta.

2.2.8. RAD52 detection

The binding of protein multimers was investigated using the DNA repair protein RAD52 [153, 154]. Truncated RAD52 in TRIS buffer (25 mM tris(hydroxymethyl)aminomethan, 50 mM NaCl, pH 7.5) was prepared by Maria Kharlamova. Sandro Münch performed the experiments. 1 μM truncated RAD52 was flushed into a flow cell (type B, Sect. 1.3.4 of air plasma cleaned glass). The sLED was operated at 0.5 mW at 20 °C. The camera was operated at 100 fps and standard settings. The iSCAT contrast was set to 55 000.

2.3. Results & Discussion: Camera program with IRM and iSCAT mode

To achieve an efficient and high speed optimized camera program, I wrote the new camera program combining IRM and iSCAT mode from scratch. Using the NI PXIe 1435 frame grabber, the Labview IMAQ-dx drivers could be used to obtain the data from the camera in Labview. To keep the overall loop speed high and identify performance issues quickly, all independent processes were performed in separate loops working in parallel. To prevent data loss, data transfer between the loops was performed by enqueuing elements in the data-producing loops and dequeuing elements in the data-consuming loops. A growing queue size indicated that the performance of a consumer loop was not sufficient to keep up with the producer loop. Thus, the queues should be monitored in the user interface when settings are modified (Fig. 2.5).

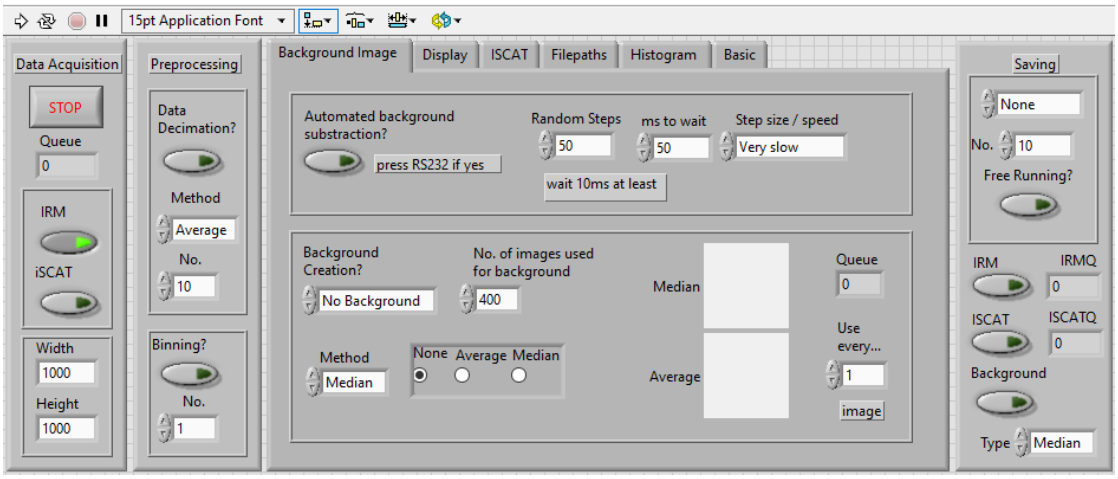

Figure 2.5.: Camera program user interface

2.3.1. User Interface

The user interface is structured in four different blocks: first the “Data Acquisition” block enables the user to stop the program, monitor the data acquisition queue, (de)activate the IRM and/or iSCAT data generation loops and adjust the image size. The “Preprocessing” block enables the optional decimation of the raw data by generating average or median images from a specified number or by binning a specified amount of pixels. This preprocessing affects the data that will be displayed and saved. The next block comprises multiple tab windows. The “Background Image” tab enables the automated background subtraction with a specified number of random steps, the time to wait at each position before a new step is performed and the size of the steps determining the speed of the movement. When the “Background creation?” button is activated, the stage performs the specified movement. Then, the program collects a specified number of images to create either a median or an average image depending on the user settings. The last created background image of each method is displayed at the user interface and can be selected or deactivated. The “Display” tab contains options to adjust the display windows of both IRM and iSCAT. To keep the overall performance of the program while generating data at high speed, the displayed data can be decimated and binned separately without influencing the saved data. Furthermore, the position and zoom of the windows can be modified and the brightness and contrast can be adjusted separately. In the “iSCAT” tab, the type of background image used for iSCAT can be chosen and the size of the running average can be set. Furthermore, the iSCAT contrast can be modified. The tab “Filepaths” contains the file paths for data saving. A histogram of the unprocessed raw data can be activated and monitored in the “Histogram” tab and the minimal, maximal and mean pixel values of the unprocessed IRM image and the iSCAT image are displayed upon activation. In the “Basic” tab, required settings to initialize the camera are displayed. The “Saving” box enables the activation of two different saving methods: if the “Free Running?” button is activated, saving can be

performed as long as the user switches back from “Saving” to “None”. If the “Free Running?” button is deactivated, only a specified amount of images is saved upon switching the saving button from “None” to “Saving”. This feature is, for example, useful for high speed imaging where only one image is desired to be saved but many images would be recorded within the response time of the user. To enable the parallel saving of IRM and iSCAT images, one or both imaging modes can be activated below before the saving is started. Additionally, the background image can be saved.

2.3.2. Program structure

The program structure underlying the user interface is schematically shown in Fig. 2.6. In the acquisition loop (Fig. 2.6, **1**), the raw data is transferred to a histogram (Fig. 2.6, **2**) and a preprocessing and data distribution (Fig. 2.6, **3**) queue. The histogram queue generates histograms and displays them. The preprocessing and data distribution queue comprises multiple features. First, incoming raw data can be binned or decimated by creating average or median images. Second, the preprocessed data can be enqueued to three different queues for either the creation of a background image (Fig. 2.6, **4**), IRM (Fig. 2.6, **5**), or iSCAT processing (Fig. 2.6, **6**). While the IRM processing only comprises the optional subtraction of a background image (median or average), the iSCAT processing comprises multiple steps as described in Sect. 2.2.4. As the IRM and iSCAT modes can require different saving and display options, two separate display (Fig. 2.6, **7** and **10**) and saving loops (Fig. 2.6, **8** and **9**) are used.

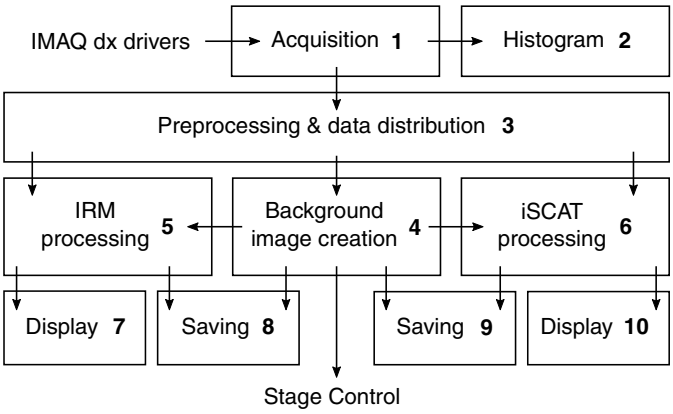

Figure 2.6.: Schematic overview of the internal structure of the camera program. Loops running in parallel are shown as frames. The data flow is shown as arrows. The data transfer between two loops is implemented by queues.

2.3.3. Performance

To test whether the performance of the program was sufficient for typical iSCAT experiments, the parameters CPU and RAM were monitored for different ROIs and frame rates (Fig. 2.7). The RAM usage (Fig. 2.7A) remained relatively constant during the usage of the IRM mode but increased upon increasing the iSCAT running average size. This increase was due to the presence of large image stacks in the memory that were required for data processing. Using a ROI of 400x400 pixels and a frame rate of 948 (cyan),

the RAM usage increased up to 2.1 GB for a running average size of 200. Here, 2×200 images of 400×400 pixels were required to be in the memory for data processing. For the lower ROI sizes of 300×300, 200×200 and 100×100 pixels (black, blue, magenta), this RAM usage was reduced to about 1.2, 0.5 and 0.1 GB, respectively. In contrast, the CPU (Intel® Core™ i5-4590 CPU at 3.30 GHz) used by Labview already increased noticeably already using the IRM mode only (Fig. 2.7B). Depending on the frame rate and ROI size, Labview required already half of the available CPU (42–53 %) to acquire the data through the frame grabber. Additionally displaying the acquired IRM images at a rate of 25 fps caused an overall CPU usage of 47–64 %. Constantly subtracting a background image increased the CPU usage to 57–86 %. Additionally decimating the data by 3, 5 or 10 increased the CPU usage to 82–88 %. Further activating the iSCAT mode (data processing and display) increased the CPU usage to 88–96 % which remained constant independent of the running average sizes. The data decimation required for stable iSCAT imaging (Fig. 2.7C) at the respective frame rate and ROI size resulted in an effective iSCAT imaging rate (Fig. 2.7D). For comparison, an effective iSCAT imaging rate of 100 fps (1000 fps data acquisition and data decimation by a factor of 10) was reported [144] and is drawn as a black dashed line in Fig. 2.7D. Overall, effective iSCAT rates above 100 fps could be achieved for all ROI sizes.

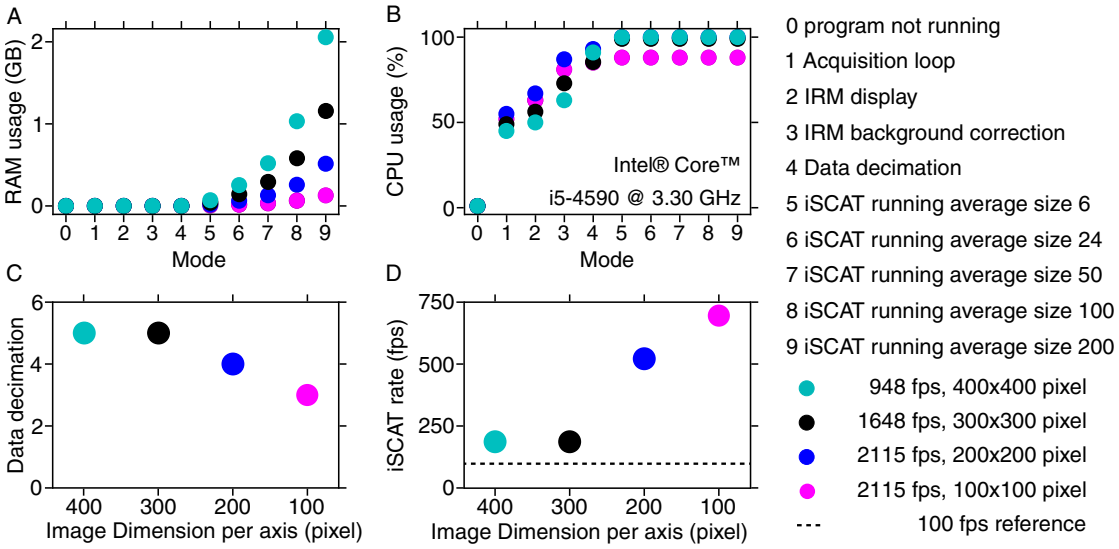

Figure 2.7.: RAM (**A**) and CPU (**B**) usage of the program with different features (0–4) activated consecutively. The activation of the iSCAT feature with different running average size (5–9) required data decimation (**C**) that reduced the effective iSCAT image processing rate (**D**). A literature reported effective iSCAT processing rate of 100 fps [144] is marked with a black dashed line. The parameters depended on the acquisition frame rate and the ROI and were exemplarily measured for 400×400 pixels at FR_{max} of 948 fps (cyan), 300×300 pixels at FR_{max} of 1648 fps (black), 200×200 (blue) and 100×100 pixels (magenta) at 2115 fps.

2.3.4. Simultaneous IRM and iSCAT imaging

The difference between IRM and iSCAT imaging is demonstrated at the example of microtubules that were loosely attached to a glass surface (Fig. 2.8). While the IRM image displayed all sample features, the iSCAT images only visualized dynamic features. In Fig. 2.8, microtubules are barely moving at time t_1 and the stage is kept constant. Thus, the removal of the static sample features generated an almost blank iSCAT image. At time t_2, the stage was moved manually. This stage movement caused all sample features to appear as dynamic features in the iSCAT image with a high contrast (Fig. 2.8B). A microtubule that appeared black in an IRM image appeared black in iSCAT as well. The position where the microtubule was located before the movement appeared white in the iSCAT image. Therefore, the translation direction of the stage (black arrow) could be identified by the resulting characteristic black-and-white pattern in iSCAT. At time t_3, the stage was kept constant and the microtubules moved strongly compared to time t_1. The corresponding iSCAT image is presented with optimized contrast settings (Fig. 2.8C). In this image, the static background is removed and the moving microtubule parts stand out. Again, the black-and-white pattern provided information about the

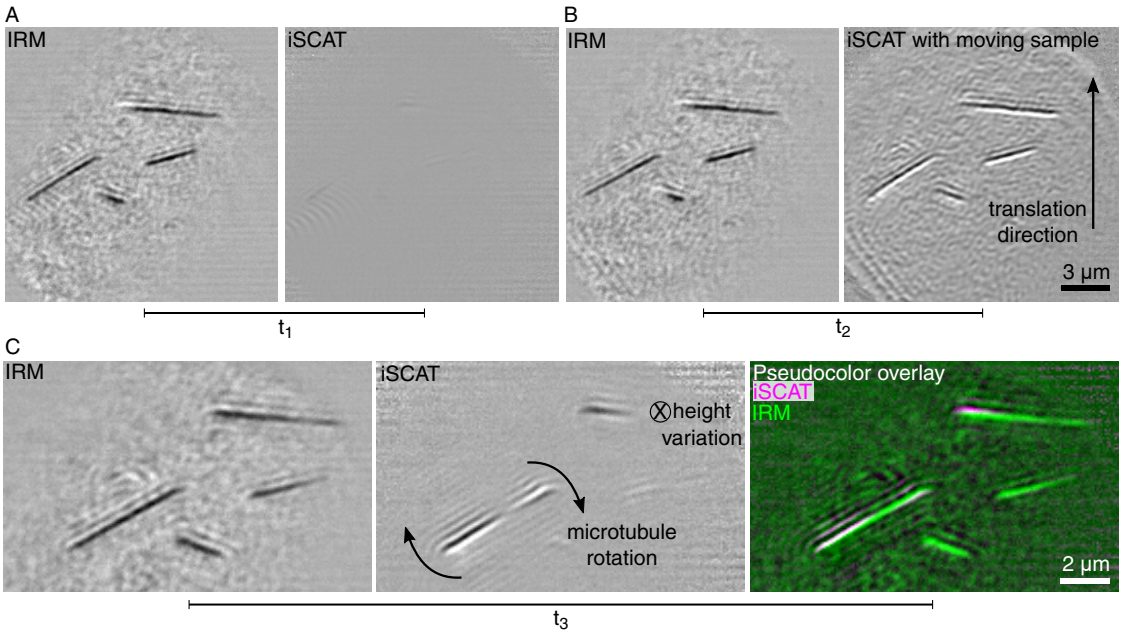

Figure 2.8.: IRM (left) and iSCAT (right) image simultaneously recorded at time t_1 (**A**) and t_2 (**B**). At t_1 microtubules barely move and the stage is kept constant. At t_2, the stage is moved manually and all sample features appear in iSCAT. At time t_3 (**C**), the stage is kept constant but the microtubules move strongly and are presented at optimized contrast settings. Black arrows indicate lateral movement and a circle with cross indicates vertical movement. A pseudocolor overlay of the IRM and iSCAT image visualizes the static (green, IRM) together with the dynamic sample parts (magenta, iSCAT, overlay resulting in white color).

movement direction. The black arrows in Fig. 2.8C indicate the direction of the rotational movement of the microtubule. A microtubule part moving at different heights is indicated by a black circle with a cross. Combining the IRM and iSCAT information in a pseudocolor overlay (Fig. 2.8C, right) allowed the identification of static and moving sample features without the necessity of recording a time series. In this overlay image, the IRM image is shown in green while the iSCAT image is shown in magenta. Overlapping signals are displayed in white and indicate moving sample features. Overall, simultaneous IRM and real-time iSCAT imaging allowed to record the information of the static features, moving features and movement direction at a single time point without the necessity of recording image sequences, and removed the static background.

2.3.5. Detection of RAD52 multimers using the iSCAT mode

Typically, iSCAT is used to detect the binding of single molecules or multimers. To demonstrate such a measurement, a protein forming multimeric rings called RAD52 [153, 154] has been investigated. RAD52 monomers were most likely not yet visible. Nevertheless, the binding of single RAD52 11mers with a molecular weight of about 270 kDa [154] could be observed (Fig. 2.9). The magenta arrow in Fig. 2.9 highlights the binding of a large, pronounced RAD52 multimer. The contrast of this multimer increases over time until a maximum is reached and then gradually decreases over time again. In iSCAT imaging, the signal of a single binding event becomes first more pronounced when the protein is present in more and more image frames contributing to the running average Av_{k+1}. After reaching the maximum, the signal contrast reduces gradually when the protein is additionally present in more and more images of the second running average Av_k used for ratiometric image correction. Therefore, the amount of images in which the signal was present was $2 \times$ the running average size.

At the beginning of the time series ($t = 0\,\mathrm{s}$), only interference signals of the binding proteins are visible. However, at the end of the time series ($t = 1.6\,\mathrm{s}$) an irregular background structure is visible. This structure may indicate, that drift or other sample fluctuations are present. Alternatively, the already bound proteins are not attached stably to the surface and contribute with small fluctuations at the surface to an increasing background. Using the iSCAT mode in real-time during the experiment enables the user to identify and improve such issues before the actual data acquisition. Overall, the real-time iSCAT mode proved to be suitable for typical protein binding experiments and the optimization of the experimental conditions. A calibrated setup can further be used to determine the molecular mass of the binding protein multimers based on the contrast.

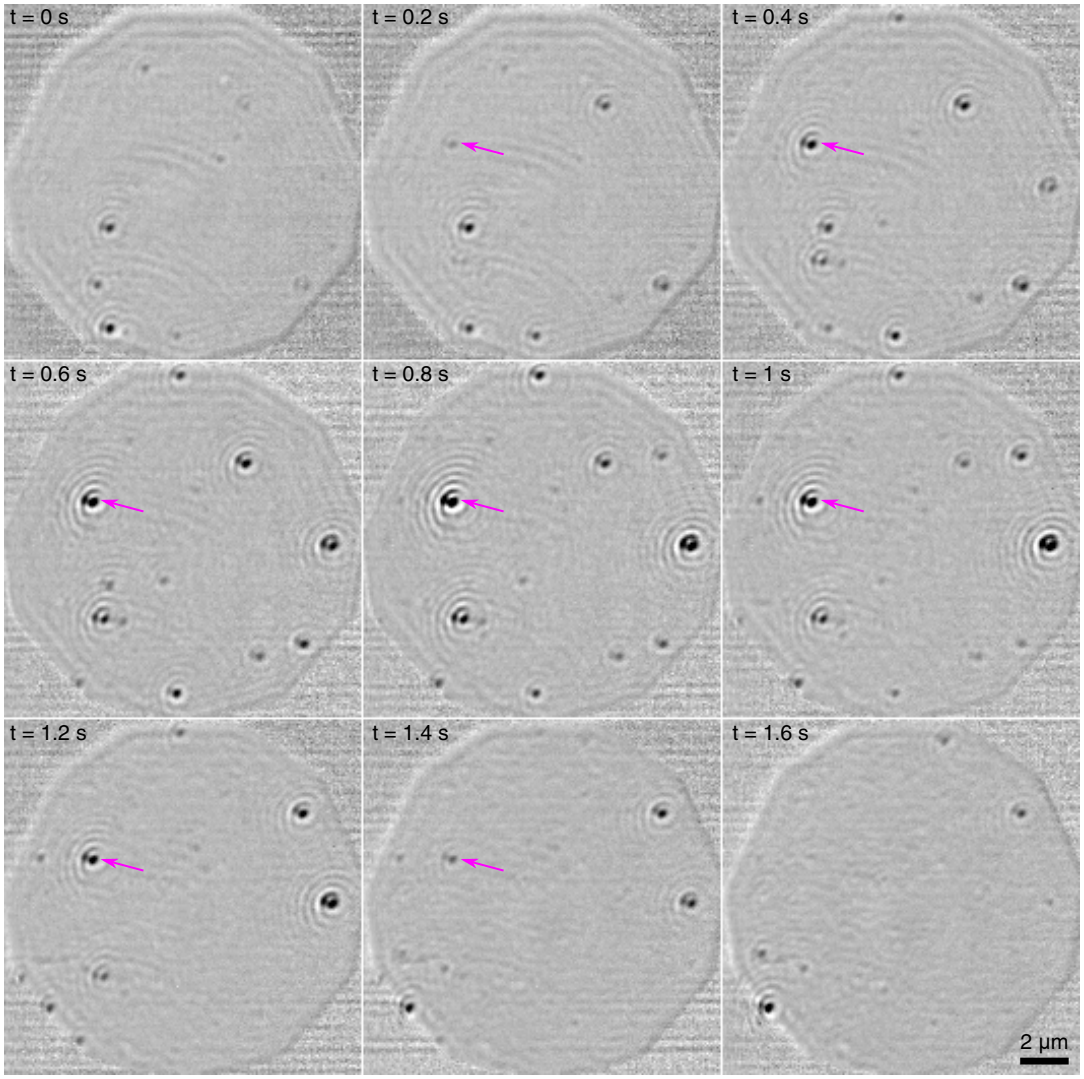

Figure 2.9.: Time series of iSCAT images showing the binding of RAD52 multimers to the surface. One exemplary multimer is highlighted with a magenta arrow.

2.4. Conclusion & Outlook

In summary, I wrote a functional imaging program combining IRM and iSCAT data processing. Both modes could be used separately and in parallel. The internal structure of the program was optimized for imaging at high speeds by separating image processing in parallel operating loops. Furthermore, the stage movement upon background subtraction was automated and could be adjusted for different imaging speeds. This feature will be relevant when imaging is performed at high speeds. Here, an automated quick movement of the stage is required to move the sample continuously during the collection of images for the background generation. In this manner, image artifacts

are prevented. Microscope images demonstrated the effective reduction of background artifacts during iSCAT imaging. Furthermore, iSCAT imaging successfully visualized only the moving parts of the sample. The movement direction could be identified based on a characteristic black-and-white pattern. The binding of RAD52 protein multimers was successfully detected. Performance tests showed that the program was operating efficiently at low memory usage unless iSCAT imaging was performed at high running average numbers. At speeds of about 1000 or 2000 fps, the CPU of the current system approached the limit for iSCAT processing requiring a decimation. This data decimation reduced the effective iSCAT imaging rate. Nevertheless, iSCAT real-time imaging at literature reported effective iSCAT imaging rates of 100 fps [144] or faster was possible. At this frame rate and with the implemented ratiometric imaging, the detection of small streptavidin molecules of about 19 kDa has been reported [144]. Therefore, the performance of the imaging program is most likely sufficient to detect the about 100 kDa large [145] single kinesin molecules. For a faster performance and additional features, the computer hardware would have to be improved. An interesting additional feature would be to detect and analyze the protein mass in real-time. However, for the analysis of protein masses, a calibrated setup is necessary. An experimentally limiting factor is the available photon flux for detection. Higher frame rates require a higher photon flux. While conventional iSCAT is performed using laser illumination, the present setup employs an sLED with different illumination characteristics such as light density and coherence length. It remains an open question, whether the sLED illumination performs comparable to or better than laser illumination. When the expected sensitivities can be achieved or exceeded with the new iSCAT setup, the detection of single kinesin molecules translocating along microtubules adds additional challenges. The microtubule "tracks" possess a high molecular mass compared to a single kinesin. A stably bound microtubule is expected to be invisible in the iSCAT mode where only the moving kinesins would appear. Therefore, microtubules require to be well attached as any microtubule movement would cause iSCAT image artifacts. Such a stable microtubule attachment may be achieved using the HMDS or APTES-silanized surfaces discussed in Chapter 1.

3. Polycationic gold nanorods as multipurpose *in vitro* microtubule markers

3.1. Introduction

The localized surface plasmon resonance (LSPR) of gold nanoparticles leads to fascinating phenomena such as electric field enhancements, plasmonic luminescence and refractive index dependend absorption and scattering. These phenomena allow the usage of gold nanoparticles as plasmonic nano antennas, non-blinking and nonbleaching luminescent probes, refractive index sensitive sensors and many more [155–161]. These plasmonic resonances depend on the shape of the particle. Different geometrical axes will translate into different plasmon modes that can be selectively excited using polarized light [162–164]. One example are gold nanorods (AuNRs). Their simple geometry yields two plasmon modes. Due to their increased aspect ratio, strong field enhancements exist at the AuNR tip [162–164]. This tip enhancement of the AuNRs can boost the emission of fluorophores or strongly enhance sensor signals and fields [158, 159]. Therefore, AuNRs can be used as nanoantennas in combination with other sensory devices and further extend their limits. For instance, combining resonators such as whispering-gallery modes with AuNR nanoantennas allows a nanosecond time resolution sensitive enough to detect single ions [159–161]. The binding and decomposition of single ions and molecules such as adenosine triphosphate (ATP) is highly relevant in biological processes such as conformational changes of molecular motors [78, 165, 166]. These motors are necessary for various cellular processes such as cell division and cellular transport [1]. Nevertheless, important molecular details on how the conformational changes relate with ATP binding and hydrolysis are still speculative, as tools for a simultaneous detection of both processes are missing. The ATP-driven conformational changes of kinesins enable an 8 nm step per hydrolysis cycle, divided into two 4 nm substeps, along microtubule "tracks" while rotating in a hand-over-hand mechanism [167, 168]. The translocation of kinesins can be monitored by imaging gliding or stepping assays. In these assays, either surface-attached kinesins transport microtubules (gliding assay) or surface-attached microtubules serve as "tracks" for kinesin movement (stepping assay), respectively. Imaging techniques are typically differential interference contrast (DIC), total internal reflection fluorescence (TIRF) and interference reflection microscopy (IRM). These techniques are often used in combination with optical tweezers to gain detailed information about the performance of single kinesins [101, 113, 169–175]. Furthermore, these techniques can be combined with plasmonics. By tracking kinesins via the resonance-enhanced scattering

of gold nanoparticles, it was possible to resolve conformational changes and intermediate steps within an ATP hydrolysis cycle [173, 174]. Microtubule-bound AuNRs were used to determine the translational or rotational motion of microtubules during gliding assays via DIC microscopy [169–171]. However, established techniques can only resolve the trajectories of motion. Yet, AuNR nanoantenna based techniques have the required spatiotemporal resolution that might allow the correlation of chemical and conformational changes in the future. To achieve this challenging goal, the first step was to bind AuNRs to microtubules such that the plasmonic near-field of the AuNR could potentially sense kinesins that walk past them. So far, irregularly shaped gold nanoparticles were directly synthesized onto microtubule templates or presynthesized gold nanoparticles were functionalized with NeutrAvidin or anti-biotin antibodies and attached to biotinylated microtubules [169–171, 176–178]. NeutrAvidin and antibodies have diameters of about 5 nm [179] and 10 nm [180], respectively. The resulting protein coatings block the most sensitive region of the plasmonic sensor. However, the most sensitive plasmonic near-field within the first few nanometers close to the surface is required to keep the spatiotemporal resolution high [158, 181–183]. Another disadvantage of antibody coatings is, that an additional surface passivation to prevent aggregation of the particles is required [5]. The aggregation of synthesized AuNRs is typically prevented by adsorbed bilayers of charge-stabilizing cetyltrimethylammonium bromide (CTAB). These bilayers have a thickness of several nanometers and block the plasmonic near field as well [160,182,184]. Other disadvantages of CTAB-coated AuNRs are cytotoxicity and a specific concentration of CTAB required to stabilize the colloid. If the CTAB concentration is too high or too low, particles aggregate [185–187]. To reduce the cytotoxicity and to be independent of CTAB concentrations, AuNRs were charge-stabilized using (11-mercaptoundecyl)-N,N,N-trimethylammonium bromide (MUTAB) [188, 189]. The thin, covalently bound cationic MUTAB monolayer was able to electrostatically interact with the negatively charged microtubule surface. The CTAB and MUTAB AuNRs were compared in terms of their coating thickness and sensing functionality. Transmission electron microscopy (TEM) was used to confirm AuNR binding to microtubules and investigate their orientation relative to the microtubule axis. To rule out that binding to microtubules was an artifact of TEM sample preparation, various *in vitro* assays were performed using IRM and TIRF. To detect the AuNRs in TIRF, AuNRs were either fluorescently labeled or the plasmonic luminescence of the AuNR was excited. To have an optimized coupling of AuNR and whispering-gallery mode in potential future measurements, different methods to bind AuNRs and microtubules in close surface proximity were investigated.

3.2. Theoretical background

3.2.1. Localized surface plasmon resonance

Plasmons are the quantized oscillation of free electron gas density relative to fixed cationic metal cores [190]. Plasmonic oscillations are typically induced in metals by electromagetic (EM) radiation. While propagating surface plasmon resonances require

the excitation with an evanescent field parallel to the metal surface, the localized surface plasmon resonance can be induced by excitation from various angles. A surface plasmon resonance is localized, when the dimension of the metal is smaller than the wavelength of the EM radiation, e.g. a nanoparticle. Here, the electromagnetic field in the nanoparticle can be considered as static and causes a dislocation of the free electron gas relative to the cationic atomic cores (Fig. 3.1) [191]. The generated surface charges lead to a restoring force which excites an oscillation of the free electron gas with an eigenfrequency. The restoring force and thus the eigenfrequency depend on the polarizability of the surrounding medium and on the distance between the surface charges (size and aspect ratio of the particle). When the exciting EM radiation matches the eigenfrequency of the electron oscillation, a localized surface plasmon resonance (LSPR) is generated and leads to high field enhancements [190]. Besides the generation of strong plasmonic fields, the electron oscillations can emit EM radiation with the same wavelength as their oscillation frequency. This radiative decay is termed plasmonic scattering. During a nonradiative decay that is called absorption, energy is lost due to dampening of the oscillations in the material. When the light transmittance of plasmonic nanoparticles is measured, both processes—scattering and absorption—contribute to the measured transmittance or extinction [192–196]. Irrespective of the exact contribution of the two decay processes, the extinction spectra shows at which frequency the LSPR is excited. Using Mie theory [191, 197], the extinction spectrum of a metal sphere can be calculated according to

$$E(\lambda) = \frac{24\pi^2 N_p r^3 \epsilon_{out}^{3/2}}{\lambda \ln(10)} \left[\frac{\epsilon_i(\lambda)}{(\epsilon_r(\lambda) + \chi\epsilon_{out})^2 + \epsilon_i(\lambda)^2} \right] \tag{3.1}$$

with the size r of the particle, the amount of polarizable elements N_p within the particle, the wavelength λ of the exciting EM radiation, the external dielectric constant ϵ_{out} and the real and imaginary components of the dielectric function of the metal ϵ_r and ϵ_i, respectively. The shape factor χ is 2 in the case of a sphere. It can only be solved analytically for spheroids and requires extensive numerical calculations for other geometries. Nevertheless, Eq. 3.1 shows how the extinction spectra of the LSPR scale with the particle size, shape and refractive index of the particle and surrounding medium [191]. For a particle of a given size and shape, changes in the extinction spectra can be correlated

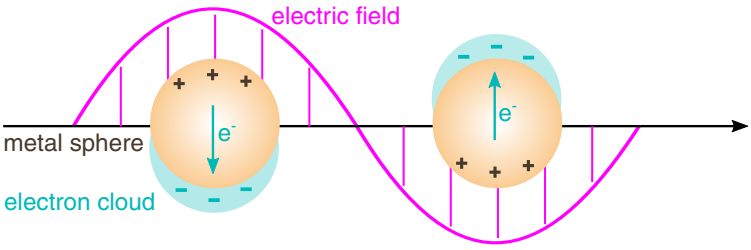

Figure 3.1.: Gold nanoparticles (yellow) exposed to electric radiation (magenta): free electrons (cyan) oscillate opposite to an electromagnetic field around the positive atomic cores of the particle.

with a change in the refractive index at the nanoparticle surface. Typically, the wavelength with a maximal extinction is considered as the position of the LSPR peak (λ_{max}) and a shift in λ_{max} ($\Delta\lambda_{max}$) can be used to gain information about the environment of a plasmonic particle according to

$$\Delta\lambda_{max} = m\Delta n\,[1 - \exp(-2d_a/l_d)] \tag{3.2}$$

with the response of the nanoparticles to a change in the refractive index m (obtained by calibration), the change in the refractive index Δn (induced by the adsorbate), the adsorbate layer thickness d_a and the characteristic decay length of the EM-field l_d [191, 198].

Photoluminescence When excited with a laser, plasmonic nanoparticles can emit light. Compared to bulk metal or surfaces, plasmonic nanoparticles show a photoluminescence that is enhanced up to a factor of 10^6 [199]. The reason for this enhanced photoluminescence efficiency is still discussed [200]. When the photoluminescence spectrum of a plasmonic nanoparticle deviates from the plasmonic scattering and absorption spectrum, it is determined by the band structure i.e. the orientation of the gold crystals. Here, the LSPR is thought to enhance the radiative electron-hole recombination [157, 201–204]. However, the photoluminescence spectra of plasmonic nanoparticles are often observed at the same energy as the plasmonic scattering and absorption spectra. Therefore, they are assumed to be directly related to plasmons. One explanation is that the plasmons directly decay radiatively [199, 205, 206]. Alternatively, the electron-hole pairs created by absorption may produce plasmons upon recombination and decay radiatively [199]. A combination of all three explanations did describe certain experiments best [207].

Plasmonic coupling When particles are close enough to each other such that their plasmonic near-fields can interact, plasmonic coupling occurs and the particles behave as one coupled system. This system can be described by the plasmon hybridization model. Here, the individual plasmonic states are described with dipole moments that can be oriented differently to each other, and thus lead to different possible energy levels. Considering a symmetric homodimer, the plasmons can be excited such that the dipole moments are oscillating in-phase. The in-phase configuration leads to an enhancement and a bright plasmon mode. Depending on the orientation of the light polarization to the geometrical axis of the dimer, an in-phase bonding (for polarization along the axis) or antibonding (polarization perpendicular to the axis) configuration is possible. Compared to the individual plasmonic modes, the energy of the coupled state is higher for an antibonding and lower for a bonding configuration. Comparably, antibonding and bonding out-of-phase configurations can be excited. Out-of-phase configurations cause an extinction of the dipole moments and are therefore spectrally dark plasmon modes [208–210].

Plasmon-fluorophore interactions When fluorophores are located within the near field of a plasmonic nanoparticle, the LSPR field enhancement can increase the light intensity

incident on the fluorophore and thereby enhance the fluorescent emission [211]. Additionally, the plasmonic field can modify the radiative and nonradiative decay rates of the fluorophore, leading to either fluorescent enhancement or quenching depending on the distance between the fluorophore and the nanoparticle [155, 199, 211–213]. Overall, the interaction between plasmon resonances and fluorophores is not yet understood and subject of current research [211]. Phenomenologically, it was reported that the plasmon resonance energy transfer can change the rate, intensity, direction, polarization and spectral shape of the spontaneous fluorophore emission [214–216]. Therefore, a plasmonic particle and a fluorophore are often considered combined as a plasmophore [215, 217, 218]. The plasmophore resonance energy transfer between plasmon and fluorophore exciton is determined by the plasmonic near-field, the overlap between absorption and emission spectra and the distance between the plasmonic particle and the fluorophore [216, 219–221].

Plasmonic properties of gold nanorods The different geometrical axes of a plasmonic particle are associated with independent plasmon modes. In gold nanorods, the width axis is associated with the transverse LSPR mode (T-LSPR) and the length axis with the longitudinal LSPR mode (L-LSPR). Relative to the T-LSPR mode, the longitudinal mode is red shifted. For a constant width, this red shift scales with the length of the rod [191, 222]. Thereby, plasmonic particles can be generated that have L-LSPRs at spectral regions where the plasmon damping is very small and where huge electric field enhancements can be generated [156]. Additionally, the increased curvature at the high-aspect-ratio-rod tip causes a concentration of the electric field lines and thereby leads to an additional nonresonant amplification [223]. When polarized light is used for excitation, the orientation of the mode axis relative to the light polarization determines the excitation efficiency [224].

3.2.2. Whispering-gallery-mode sensors

The whispering-gallery mode (WGM) has first been observed as a traveling acoustic wave guided around the closed concave surface of the whispering gallery of the St. Paul's Cathedral by Lord Rayleigh [225]. Especially light waves can travel inside a closed concave surface efficiently via total internal reflection and resonate at geometry dependent wavelengths. Due to radiative, scattering and material losses the guided wave decays over time and requires a constant excitation at the resonance frequency to generate strong and stable resonances. The damping of the resonance due to such losses can be characterized by determining the full width half maximum (FWHM) of the resonance peak. Dividing the energy by the energy loss or in other words the resonance frequency ω by the FWHM yields the dimensionless quality (Q) factor:

$$Q = \omega / FWHM. \tag{3.3}$$

Q factors for WGM resonators are typically high and can be in the range of 10^6-10^8 [160, 226]. Due to the total internal reflection of the traveling light wave at the resonator surface, an evanescent field around the cavity is excited. This evanescent field can be

used to excite the fluorescence of fluorophores or the LSPR of plasmonic nanoparticles [160, 227, 228]. The penetration depth of the evanescent field depends among others on the refractive index contrast at the surface. Larger refractive index contrasts at the resonator surface help to minimize radiative losses via a stronger confinement of the WGM to the resonator [228]. In contrast, a higher penetration depth of the evanescent field due to a smaller refractive index contrast at the resonator surface increases the resonator's sensitivity towards refractive index changes of the surrounding medium. The work required to polarize the surrounding medium is associated with a shift in the resonance frequency and coupling losses. These coupling losses lead to a further mode broadening. Both effects—mode shift and broadening—can be used as quantities for WGM sensing [228]. Figure 3.2A shows schematically, how laser light with an initial intensity I_0 (magenta arrow) is coupled into a spherical resonator (grey sphere) and excites a WGM (magenta wave). Analytes (cyan dots) can only be detected in the equatorial area where the WGM resonates. The transmitted laser light I_T shows a dip at the resonance wavelength where most energy is transmitted to the resonator (black line, Fig. 3.2B). Upon the binding of analytes, the mode shifts to the red (dashed cyan line, $\Delta\lambda$) and broadens (ΔFWHM). Both quantities are measured over time (cyan line, Fig. 3.2C). The mode shift and broadening increase step-wise (black circles, zoom-in) for the binding of single analytes. The increase saturates, when the surface is fully covered with analytes [229].

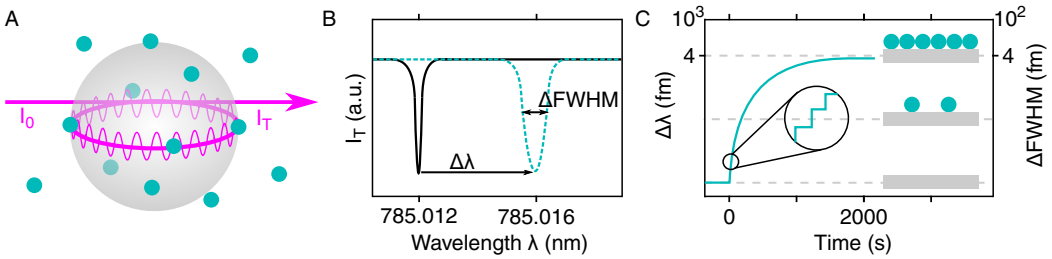

Figure 3.2.: (**A**) A laser with intensity I_0 (magenta arrow) excites a WGM (magenta wave) propagating along the equatorial area of a spherical resonator (gray sphere). Analytes (cyan dots) that bind within the equatorial area can be detected. (**B**) The resonance dip in the spectrum of the transmitted laser light I_T (black line) shifts ($\Delta\lambda$) and broadens (ΔFWHM) upon the binding of analytes (dashed cyan line). (**C**) $\Delta\lambda$ and ΔFWHM (cyan line) increase step-wise upon the binding of single analytes (circular insets). The gray dashed lines refer to the schematics to the right symbolizing a surface (grey rectangle) that is either uncovered, partially covered or fully covered with analytes (cyan dots). Figure partially adapted from [229].

3.3. Materials & Methods

For all experiments, Type 1 water (18.2 MΩ cm, Nanopure System MilliQ reference with Q-POD and Biopak filter) was used. All chemicals were purchased from Sigma Aldrich

and used without further purification, unless noted otherwise. All methods and reactions were performed at room temperature (20–28 °C) unless noted otherwise.

3.3.1. Polycationic gold nanorods

Experiments were performed with different types of AuNRs that were either purchased or synthesized.

Purchased AuNRs For photoluminescence measurements, AuNRs (0.38 nM, A12-25-550-CTAB-DIH-1-25) were purchased from Nanopartz Inc. (Loveland, US). These CTAB stabilized AuNRs with an aspect ratio of 1.6 (25 nm width and 40 nm length) had a nominal plasmon resonance of 550 nm (two combined peaks at 525 nm and 570 nm). For whispering-gallery-mode measurements, we used higher aspect ratio AuNRs (0.39 nM, A12-10-780-CTAB-DIH-1-25, Nanopartz Inc., Loveland, US). These AuNRs had an aspect ratio of 3.8, a length of 38 nm, a width of 10 nm and a L-LSPR at 780 nm compatible with the whispering-gallery-mode setup described in Sect. 3.3.4.

3.3.1.1. Synthesis

AuNRs were synthesized according to a conventional seeding growth method [230]. Firstly, gold seeds were prepared and secondly, these seeds were grown into a rod shape with the help of the structure directing silver nitrate. Gold seeds were synthesized in a yellow colored solution containing 3.75 mL 0.1 M CTAB surfactant and 125 µL of 0.01 M $HAuCl_4$ by quickly adding 300 µL 0.01 M ice cold $NaBH_4$ while stirring vigorously. After the addition of the reducing agent $NaBH_4$ the solution was stirred for 2 min at the same speed. Then, the seed solution was left undisturbed in the dark for 2 h. The growth solution was prepared in 42.75 mL of the 0.1 M CTAB solution under a constant gentle stirring. Firstly, 1.8 mL of 0.01 M $HAuCl_4$ were added and the resulting yellow solution is stirred for 1 min. Secondly, 270 µL of the structure directing aqueous 0.01 M $AgNO_3$ solution were added quickly. Immediately afterwards, the addition of 288 µL of an aqueous 0.1 M ascorbic acid solution turned the solution colorless. This indicated the reduction of the aurochloric acid ($HAuCl_4$). After stirring the colorless growth solution for 20 s, 189 µL of the seed solution were added to the growth solution and stirred for 60 s. A color change of the solution to purple after 30 min indicated a successful growth of the seeds. The solution was stored undisturbed and in the dark for further growth over night (12 h). The final dark red AuNR solution was washed and concentrated by a 30 min ultra-centrifugation at 30,000 g followed by a redispersion of the AuNRs in 4 mL of water. Assuming a theoretical yield of 100 %, the AuNR concentration of the final samples was calculated to be at most 12 nM.

3.3.1.2. Functionalization

CTAB was replaced by MUTAB by following a procedure similar to the one described in [189]. To achieve a clean product ready for functionalization, two additional washing steps composed of a 15 min centrifugation at 11,000 g and a redispersion in water were

performed. During the final washing, AuNRs were concentrated by redispersion in 1 mL water. 80 mg MUTAB (weighed/stored under nitrogen) was dispersed in 3.7 mL of pure water under vigorous stirring. For an optional fluorescent labeling, 0.3 mL of a 14.7 mM rhodamine-3.4 k-PEG-thiol solution (Biochempeg Scientific Inc., Watertown, US) were mixed with the MUTAB solution. Subsequently, AuNRs were added and stirred in the dark for 2 days. Finally, the MUTAB or MUTAB-rhodamine functionalized AuNRs were washed 5× by a combination of 15 min centrifugation at 11,000 g and redispersion of the sample in pure water.

The purchased AuNRs were functionalized by dissolving 20 mg MUTAB in 250 µL water and mixing 250 µL of the 0.38 nM CTAB AuNR colloid to the solution under constant stirring in the dark for 2 days. The functionalized AuNRs were washed as described above but concentrated to 0.7 nM during the last washing step.

3.3.1.3. Characterization

Extinction spectra were recorded with a Peqlab (Erlangen, DE) Nanodrop ND-1000 spectrofluorometer (UV/Vis function). Hydrodynamic radius and surface potentials were determined using a Malvern (Worcestershire, United Kingdom) Zetasizer Nano ZS. For dynamic-light-scattering (DLS) and zeta-potential measurements, the used parameters for the dispersant (water) were a viscosity of 0.8872 cP, a Henry's function of 1.5, a dielectric constant of 78.5 and a refractive index of 1.33. All samples were equilibrated to 25 °C for 30 s. Zeta-potential measurements were performed in a zeta cell (DTS1070, Malvern Instruments) and measured at an applied voltage of ± 150 V. Dynamic-light-scattering measurements were performed in Sarstedt Disposable Cuvettes DTS0012 and measured with the integrated 633-nm He-Ne laser operating at an angle of 173°. Three automated runs of 70 s duration were performed per sample. The intensity size distributions were calculated by the device associated program from the autocorrelation function using the "multiple narrow mode".

3.3.2. Microtubule-gold-nanorod assays

GMPCPP-stabilized microtubules were polymerized and stabilized as described in Sect. 1.3.5.

3.3.2.1. Transmission electron microscopy (TEM)

Electron microscopy exploits the short wavelength of electrons to achieve high resolutions compared to light microscopy. Instead of optical lenses, magnetic lenses are used to manipulate the electron beam. For TEM, the electrons transmitted by a thin (below 100 nm) sample are recorded as a 2 D image [231]. For the used JEOL 120 kV 1400plus microscope, the resolution was specified by the manifacturer to be 0.38 nm point-to-point resolution when operated at 120 kV [232]. However, the negative staining of biological samples with uranylacetate allows only resolutions of about 2 nm due to the grain size of the stain [233]. All images displayed in the thesis were recorded by York Stierhof

with a Tietz TemCam F-416 CMOS camera. A small portion of undisplayed images used for data analysis was recorded by myself. TEM samples were prepared by the drop application method [234]. First, AuNR-microtubule binding was induced by mixing 5 µL of microtubule solution with 9 µL MUTAB AuNR solution (0.1–1 nM assuming a 12 nM CTAB solution and losses up to a factor of 10 during MUTAB functionalization) for 10 min with a AuNRs solution. Afterwards, pioloform and carbon-coated copper TEM grids were incubated for 3 min with 5 µL droplets of this AuNR-microtubule mixture. Excess sample was washed off by incubating the grid with a clean 20 µL PEM (80 mM PIPES, 1 mM EGTA, 1 mM $MgCl_2$, pH = 6.9) droplet for 1 min. The sample was fixed with 2.5 % glutaraldehyde for 5 min. Excess glutaraldehyde was removed by incubating the TEM grids 5× with 20 µL of nanopure water for 10 s. Finally, the TEM grids were stained for 30 s with 1 % aqueous uranyl acetate. Excess uranyl acetate was removed with a dry filter paper and the sample was left to dry.

3.3.2.2. Microfluidic assay for IRM & TIRF

Flow cell preparation Coverslides were rendered hydrophobic via TMCS silanization or functionalized with APTES as described in Sect. 1.3.3.1 and 1.3.3.4. Parafilm based flow cells (Sect. 1.3.4) were constructed in a clean room environment. For hydrophobic flow cells, microtubule attachment and surface passivation was performed as explained in Sect. 1.3.6.1. APTES flow cells were directly incubated with microtubules for 5 min. All subsequent steps were equally performed for both flow cell types: residual microtubules were washed out with diluted PEM (10% in water, PEM10). To minimize the overall salt concentration but prevent microtubule depolymerization upon AuNR addtion, PEM buffer was added to the functionalized the AuNRs such that a PEM concentration of 10% was achieved. Then, the AuNR-PEM solution was flushed in the microfluidic channel and incubated for 5 min. Unbound AuNRs were washed out with either diluted PEM or an anti-fading mix (0.02 m/mL glucose oxidase, 20 mM D-glucose and 0.008 mg/mL catalase), depending on the type of AuNRs used. AuNRs without rhodamine label, that were plasmonically active at the used excitation wavelength of 561 nm, were flushed out with PEM10. AuNRs with rhodamine label but plasmonically inactive were washed out with anti-fading mix to increase the fluorescence lifetimes of the dyes. For Fig. 3.12, 0.5 nM Kip3 (yeast, Kip3-eGFP-His6 [138,235]) was first incubated to the APTES-bound microtubules and afterwards, rhodamine-labeled AuNRs were added.

Imaging Imaging was performed on a temperature-stabilized setup with millikelvin precision and the temperature set to 29.000 °C [104]. The setup combined IRM and TIRF similar to a previously published setup [101]. TIRF excitation was performed with two different wavelengths using a 488 nm (100 mW LuxX 488-100 Omicron Laserage, Rodgau, DE) and a 561 nm (100 mW OBIS 561CS-100, Coherent, Santa Clara, CA, US) laser, respectively. A HC-Beamsplitter BS 560 separated the excited signal into the two distinct channels using a custom-made color splitter [101]. An ET Bandpass 520/40 defined the green channel and an ET Bandpass 605/70 defined the red channel. 5 mW output power of the 561-nm laser was used to excite rhodamine and the AuNRs' intrinsic

Table 3.1.: Used exposure times (Exp), laser intensities (I_{561} and I_{488}), and imaging intervals that were used to record the data of the respective figures.

Figure	**Exp (ms)**	**I_{561} (%)**	**I_{488} (%)**	**Interval (s)**
3.9B	200	5	-	-
3.9C	200	50	-	-
3.9D blue line	5000	5	-	2
3.9D black line	200	5	-	5
3.10	200	5	-	-
3.11	200	5	-	-
3.12	200	5	5	1

luminescence. The image acquisition time was 200 ms using an Orca Flash 4.0 V2 camera (Hamamatsu Photonics, Hamamatsu City, JP). Specific TIRF imaging parameters are shown in Table 3.1.

3.3.3. Image Processing

All images were further processed in Fiji [236] and GIMP. To obtain bleaching time lines as shown in Fig. 3.9D, multiple fluorescence images were recorded over a time line and processed as an image stack. With Jython programming in Fiji, AuNR positions were detected with an intensity threshold. Furthermore, the pixel intensities at all AuNR positions were extracted for every image in the stack and saved as a matrix. In Python, the time line of each AuNR intensity was plotted. Exemplary time lines are shown in Fig. 3.9D.

For Fig. 3.10G and H, the software Gwyddion was used to remove an uneven parabolic background of the TIRF image with the feature "remove polynomial background" with a horizontal and vertical polynomial degree of two. For all IRM images, the contrast depends on the object's molecular mass, refractive index, and distance to the surface. For objects of the same mass and refractive index with different distances from the surface—e.g. a microtubule partially attached and partially extending into the channel—the following contrast is expected. Microtubule regions directly attached to the surface have black intensity gray levels. Intermediate gray levels correspond to ≈ 40 nm and white gray levels to ≈ 80 nm distance of the microtubule from the surface [101]. For IRM/TIRF overlays (Fig. 3.10D, H and Fig. 3.11D) the following pseudocolor scale was used to make colocalizations appear in white. First, the 256 IRM gray scale values were inverted. Second, the mean image gray value was chosen as a threshold. All gray values above the threshold were displayed as brightness values of green. Third, the threshold was added to gray values below the threshold and the resulting gray values were displayed as brightness values of cyan. Thus, microtubules directly attached to the surface (originally black) were displayed as bright green and microtubule parts that were not in direct contact with the surface (originally white) were displayed as cyan regions. Thereby, all AuNR-microtubule colocalizations appeared ideally in white.

These color conversions were performed with Jython scripting in Fiji. Kymographs were obtained and analyzed as described in Sect. 1.3.7.3.

3.3.4. Whispering-gallery-mode measurements

Whispering-gallery-mode measurements were performed during a 10 day long research visit in cooperation with Narima Eerqing (N.E.) at the "Nano and Quantum Sensing" group of Prof. Dr. Frank Vollmer (Living Systems Institute, University of Exeter, EX4 4QD, UK). PEM buffer, proteins, other assay ingredients, and MUTAB AuNRs were fabricated in the Cellular Nanoscience group (University of Tübingen, DE) as indicated in Sect. 1.3.5–1.3.6.1, except for the 2-[4-(2-hydroxyethyl)piperazin-1-yl]ethanesulfonic acid (HEPES, 1 M, pH 7.5) buffer and the APTES solution. GMPCPP-stabilized microtubules were polymerized as described in Sect. 1.3.5.2 but using the Ultima MAX-TL Ultracentrifuge (Beckman Coulter, Brea, CA). Spherical glass resonators (80 μm diameter) were fabricated by N.E. by melting a single mode optical fiber (SMF 28e, Corning). For the APTES functionalization, the resonator was dipped 10 s in 5 % APTES/acetone solution and sonicated 30 s in acetone to remove adsorbed polymers. As flow chambers were not compatible with the setup, a reusable measurement chamber was filled with buffer (PEM or HEPES) and further analytes had to be added successively. Different sequences of microtubule, AuNR and kinesin additions were tried. First, microtubules were added, either diluted 1:10 or 1:100 in PEM10 or HEPES buffer. Second, 0.005–5 nM kinesin Kip3 motors were added to microtubule incubated resonators. Kinesin experiments were performed either in motility buffer (Sect. 1.3.6.1) without the anti-fading mix (20 mM D-glucose, 250 nM glucose oxidase, 134 nM catalase) or in PEM or HEPES buffer with 1 mM adenosinetriphosphate only. Measurements were performed together with N.E. on a custom-built setup as described in Ref. [237].

3.4. Results & Discussion

3.4.1. CTAB AuNRs were covalently functionalized and charge stabilized with MUTAB

AuNRs were synthesized using a two-step seeding growth method employing CTAB as stabilizing agent [230] (Molecule 1 in Fig. 3.3A, see Sect. 3.3.1.1). TEM image analysis revealed AuNR dimensions of 43 ± 4 nm length and 17 ± 1 nm width resulting in an aspect ratio of 2.6 ± 0.3 (Fig. 3.3B top, mean $\pm$ SD, $N = 34$). The corresponding surface plasmon resonance was measured with a spectrofluorometer. A Gaussian fit of the longitudinal localized surface plasmon resonance (L-LSPR) in water resulted in a wavelength $\lambda_{H_2O} = 691.5 \pm 0.1$ nm (fit result $\pm$ SD, Fig. 3.3B bottom). Additionally, the TEM imaging with negative staining revealed an about 4 nm thick irregular layer covering the AuNR that was expected for a CTAB bilayer [238].

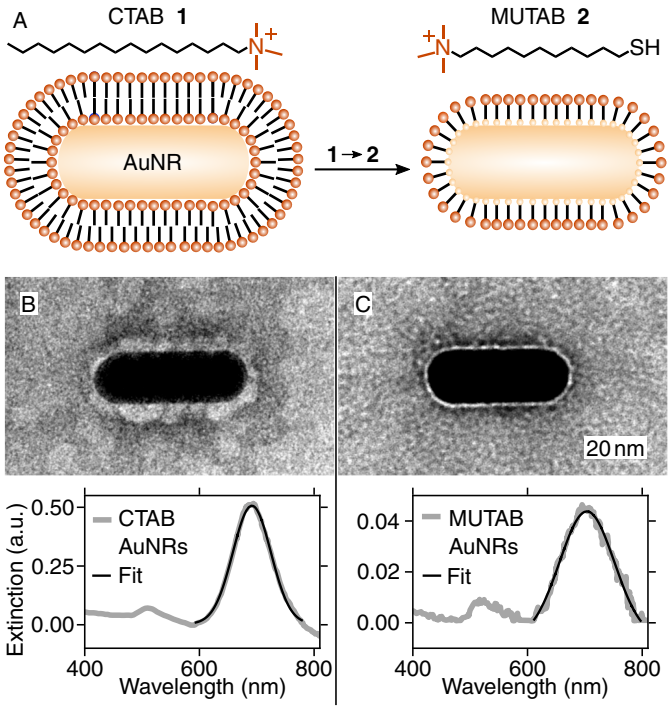

Figure 3.3.: (**A**) The gold nanorod (AuNR) coating is exchanged from an adsorbed CTAB (molecule 1) bilayer to a covalently bound cationic MUTAB (molecule 2) monolayer. Negative-stained TEM images reveal the CTAB (**B** top) and MUTAB (**C** top) coatings of the AuNRs. The corresponding extinction spectra are shown below (grey line, **B** and **C** bottom). For the Gaussian fit (black line) parameters see Appendix A.4

In agreement with the literature [189,239,240], the stability of the CTAB coated AuNRs depended strongly on the total CTAB concentration present in the solution and on the buffer conditions, that restricted dilution and biological applications.

To work with positively charged and stabilized AuNRs independent from the CTAB concentration and to generate a regular and thin coating, the adsorbed CTAB bilayer was replaced by a covalently bound cationic MUTAB monolayer (Fig. 3.3A) [189]. After the MUTAB functionalization, the LSPR spectrum had a lower intensity due to a reduced AuNR concentration. Furthermore, the L-LSPR maximum shifted to $\lambda_{H_2O} = 703.6 \pm 0.3\,\text{nm}$ (fit result $\pm$ SD, $\Delta\lambda$(MUTAB-CTAB) $= 12.1\,\text{nm}$, Fig. 3.3C bottom). This shift indicated a changed refractive index close to the gold surface. Instead of the thick irregular CTAB coating, the negative stained TEM images of the MUTAB AuNRs revealed a smooth $\approx 1\,\text{nm}$ thick layer around the AuNR that may be MUTAB (Fig. 3.3C top). Based on the chemical structure, the expected monolayer thickness is below 1 nm. While a sole reduction of layer thickness would be associated with a blue shift, the observed red shift may be attributed to the change of an adsorbed CTAB bilayer to a covalently bound MUTAB monolayer. Similar replacements of a CTAB bilayer with a covalent, thin monolayer have been reported to result in a red shift likewise [241]. As an alternative size measurement, DLS measurements were performed (exemplary measurement in Fig. 3.4A). The peak values provided by the measurement software were averaged. With DLS measurements, it was possible to detect a difference in the hydrodynamic diameter between CTAB and MUTAB AuNRs that was in agreement with the TEM analysis. The diameter of CTAB AuNRs was $51 \pm 8\,\text{nm}$

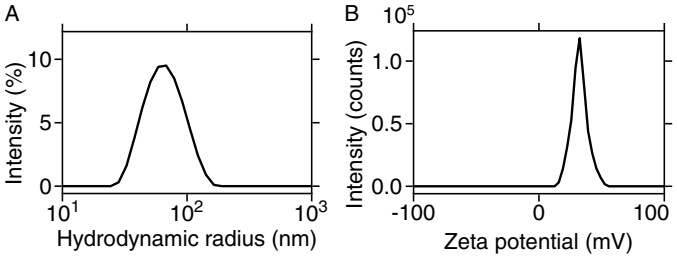

Figure 3.4.: (**A**) Intensity distribution of inferred hydrodynamic radius based on DLS of MUTAB AuNRs. (**B**) Zeta potential of a MUTAB AuNR colloid.

(mean ± SD, $N = 3$) and 8 nm larger (2×4 nm CTAB layer) than the MUTAB AuNRs diameter of 43 ± 1 nm (mean ± SD, $N = 3$). Additionally, zeta-potential measurements confirmed the positive surface charge and polycationic nature of the MUTAB AuNRs with a measured zeta potential of 31 ± 2 mV (Fig. 3.4B, mean ± SD, $N = 3$). Together, these results suggest that MUTAB AuNRs have a homogeneous, thin and stable polycationic coating suited for use under physiological buffer conditions [121].

3.4.2. MUTAB AuNRs plasmonically sensed microtubules

To investigate whether AuNRs interacted with microtubules and whether this interaction affected the plasmon resonance, AuNR extinction spectra were recorded using UV/Vis spectroscopy (Fig. 3.5). The overall signal-to-noise ratio (SNR) of the AuNRs was low and an increased noise beyond 750 nm originating from the device was apparent. The L-LSPR peak positions were estimated by fitting a Gaussian distribution. To reduce the systematic error introduced by the increased noise above 750 nm, the peaks were only fitted for lower wavelengths (see Appendix A.4). Compared to the CTAB AuNRs in water (black line Fig. 3.5A, $\lambda_{H_2O} = 698.0 \pm 0.7$ nm, fit result ± SD), CTAB AuNRs in PEM buffer (green line, $\lambda_{PEM} = 720.2 \pm 1.6$ nm, fit result ± SD) showed a L-LSPR red shift of $\Delta\lambda(\text{PEM-H}_2\text{O}) = 22.2$ nm. This shift appeared huge for the dilution in an aqueous buffer. Upon dilution in microtubule-PEM solution (blue line, $\lambda_{MTs} = 717.0 \pm 1.3$ nm, fit result ± SD), a further red shift would be expected for a functional LSPR sensor binding to microtubules. However, we did not observe such a shift for CTAB AuNRs.

In contrary, the MUTAB AuNR L-LSPR red shifted by different magnitudes upon dilution in PEM and microtubule-PEM solution (Fig. 3.5B). Compared to MUTAB AuNRs in water (black line, $\lambda_{H_2O} = 715.6 \pm 0.7$ nm, fit result ± SD), the L-LSPR of MUTAB AuNRs in PEM (green line, $\lambda_{PEM} = 719.8 \pm 1.2$ nm, fit result ± SD) was red-shifted by $\Delta\lambda(\text{PEM-H}_2\text{O}) = 4.2$ nm. The L-LSPR of MUTAB AuNRs diluted in microtubule-PEM solution ($\lambda_{MTs} = 761.6 \pm 2.1$ nm, fit result ± SD) was shifted further to the red by $\Delta\lambda(\text{MTs-PEM}) = 41.8$ nm. Note: After this shift, the L-LSPR wavelength was beyond the recommended measurement range of the device (220–750 nm). All peak positions should be considered as estimates due to the poor data and fit qualities (see Appendix A.4). Note that the L-LSPR positions measured for CTAB and MUTAB AuNRs in H_2O should be identical to the L-LSPR positions stated in Sect. 3.4.1 for the L-LSPRs shown in Fig. 3.3B. The discrepancies between these L-LSPR positions (about 10 nm) was most likely due to the increased SNR caused by further dilution (1:2) in water.

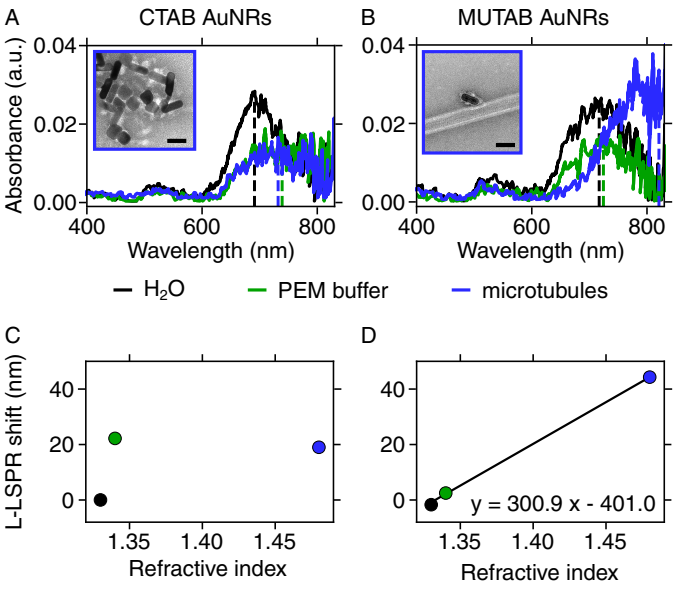

Figure 3.5.: Extinction spectra of (**A**) CTAB AuNRs and (**B**) MUTAB AuNRs diluted in water (black line), PEM buffer (green line) and microtubule-PEM dispersion (blue line). TEM images of the respective AuNR-microtubule dispersions are shown as small insets with a 25 nm scale bar. L-LSPR shifts of (**C**) CTAB AuNRs and (**D**) MUTAB AuNRs as a function of the refractive index. Note that the errorbars (SD of the fit) are smaller than the data points. The color scheme specified above applies to the data points. A linear fit is shown as a black line.

While the refractive indices of water and PEM were reported to be 1.33 and 1.34, respectively [97, 242, 243], the refractive index of tubulin is still discussed in the literature and ranges from values typical for proteins such as 1.48 to unusually high values of up to 2.90 [242–244]. For further calculations, the refractive index of microtubules was assumed to be 1.48 but may deviate [244]. From Eq. 3.2, a linear scaling of the L-LSPR shift with the refractive indices is expected but was not observed for the CTAB AuNRs (Fig. 3.5C). The unexpected L-LSPR shifts of the CTAB AuNRs and their insensitivity towards the microtubules may be explained by CTAB AuNR aggregation. This assumption was supported by TEM images of CTAB-AuNR-microtubule incubations (small inset in Fig. 3.5A) showing only CTAB-AuNR aggregates and no CTAB AuNRs interacting with microtubules. In these aggregates, the AuNRs maintained their shape and no bulk metal was formed. Therefore, the AuNRs remained plasmonically active but were packed closely together, with distances between that are comparable to the CTAB bilayer thickness. In this distance range, plasmonic coupling of the AuNRs is still expected and may cause the similar, large peak shifts observed for CTAB AuNRs in buffer and microtubule solution.

On the contrary, the MUTAB AuNR L-LSPRs shifted with the expected linear dependence on the refractive indices (Fig. 3.5D). A linear fit (black line) was used to determine the sensitivity of the AuNRs. The fit yielded $y = 300.9x - 401.0$. The calculated sensitivity of 300.9 nm/RIU was in agreement with literature reported sensitivities for comparable gold nanorods [245–248]. Especially with regard to the low SNR in general, the

additional noise beyond the official measurement limit of 750 nm and the incompletely recorded and fitted peaks, high errors are expected for the determined L-LSPR peak positions. The error-prone measurements, a possible underestimation of the refractive index of the microtubules and the few data points underlying the fit made the estimation of the sensitivity of the MUTAB AuNRs difficult.

Overall, the results suggested that the MUTAB AuNRs were functional LSPR sensors and able to detect microtubules. This was in agreement with the TEM images (small inset in Fig. 3.5B) where single AuNRs interacted with microtubules and rarely formed aggregates.

3.4.3. Fixed TEM assays suggested that MUTAB AuNRs bound to microtubules

To investigate whether the polycationic MUTAB AuNRs interacted with the negatively charged E-hooks (C-terminal regions of tubulins, see Sect. 1.2.3) located at the microtubule surface (Fig. 3.6A), MUTAB AuNRs were mixed with microtubules in physiological buffer and imaged with transmission electron microscopy (TEM, Fig. 3.6B-G). Most AuNRs colocalized with microtubules (Fig. 3.6B). The AuNRs were expected to bind with their long axis in parallel to the microtubule, as this orientation would maximize the interacting area (Fig. 3.6A). However, AuNRs bound in parallel were observed in only 12 % of the colocalizations ($N = 154$ AuNR-microtubule colocalizations in total, distributed over five batches, Fig. 3.6C) and another 12 % were tilted relative to the

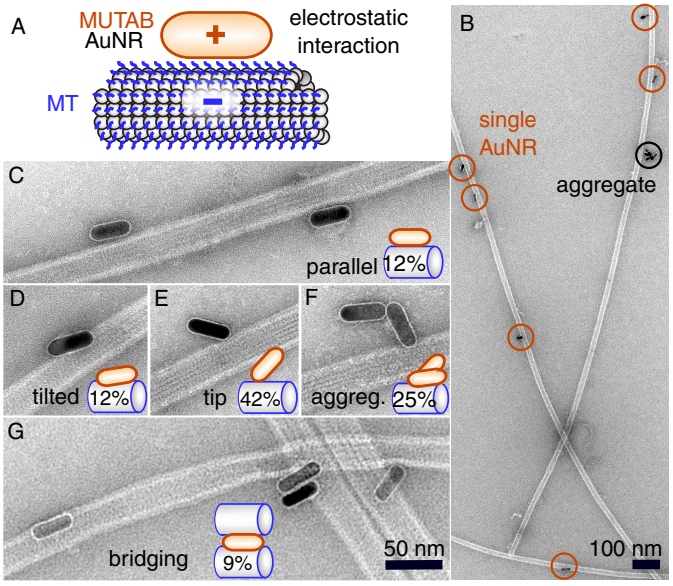

Figure 3.6.: (**A**) Proposed electrostatic attraction of the polycationic coating (brown) of a MUTAB AuNR (yellow) to the negatively charged E-hooks (blue) protruding from the microtubule (MT) surface. (**B**) Overview TEM image of microtubules decorated with AuNRs. (**C**)–(**G**) Close-up views of AuNR-microtubule colocalization sites with case percentages calculated from $N = 154$ colocalization sites distributed over five batches indicated in schematic insets. AuNRs were categorized to be parallel (**C**), tilted (**D**), tip-bound (**E**), aggregated (**F**) or crosslinking (**G**).

long axis of the microtubule (Fig. 3.6D). 42 % of all colocalizations were tip bound single AuNRs (Fig. 3.6E). The tip binding may have been preferred due to an electrostatic field enhancement at the rod tip within the negative potential of the microtubule surface. Furthermore, 25 % of the colocalizations were AuNR aggregates, containing more than one single AuNR (Fig. 3.6F). 41 % of these aggregates bridged two or more microtubules—potentially crosslinking them—comparable to the AuNR aggregate in the middle of Fig. 3.6G. Single AuNRs that bridged two or more microtubules accounted for 9 % of the overall colocalizations. Within the resolution of TEM images, AuNR binding sites occasionally showed small lattice defects, but it is unclear whether the defect was caused by the AuNR or was there before. Altogether, AuNRs colocalized with microtubules in different orientations and the data suggested that AuNR binding did not affect the microtubule structure [121].

3.4.4. MUTAB AuNRs prefered to bind microtubules over tubulin monomers in fixed TEM assays

Based on the TEM images, the interaction of MUTAB AuNRs with free tubulin mono- or oligomers may have been the reason for aggregate formation (Fig. 3.6F and 3.7A). Indeed, when MUTAB AuNRs were incubated with microtubules in a solution containing 200 nM free tubulin, the presence of colocalizing aggregates increased to 54 % ($N = 104$ counted colocalizations distributed over 2 batches). The remaining colocalizations were single AuNRs that were bound in 24 % of the cases in parallel, in 14 % bridging, in 6 % with the tip and in 2 % tilted. Most of the bridging AuNRs were parallel to the microtubule axis and intercalated between two microtubules (Fig. 3.7B). Possibly, the intermediate binding of the AuNRs induced microtubule bundling. Including the microtubule bridging AuNRs in the orientation percentages, 69 % of all single bound AuNRs were bound in parallel. This percentage is larger compared to the tubulin free samples, but in agreement with the initial expectation based on the maximized interaction area between AuNR and microtubule. The addition of depletion forces generated by free tubulin may explain why the parallel orientation was favoured. Interestingly, AuNRs still colocalized mainly with microtubules instead of with tubulin aggregates. 75 % ($N = 104$) of all AuNRs ($N_{total} = 138$) were bound to microtubules (exemplary images in Fig. 3.7A and B). This finding may support the proposed electrostatic interaction between polycationic AuNRs and negatively charged microtubules, as the collective negative electrostatic potential of the microtubule surface may be larger than that of the single tubulins or tubulin aggregates. Since AuNRs did bind microtubules selectively in a tubulin-crowded

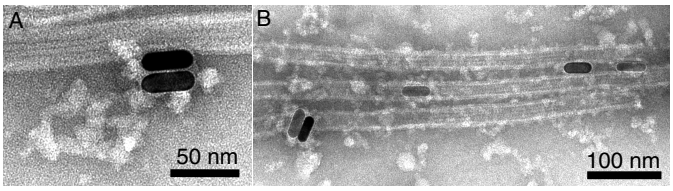

Figure 3.7.: (**A**) Close-up view of a AuNR cluster potentially held together by tubulin mono- or multimers. (**B**) Microtubule bundle surrounded by free tubulin but with colocalizing AuNRs.

environment, MUTAB AuNRs may also bind selectively to other negatively charged molecules, proteins or organelles *in vitro* and possibly also *in vivo*.

3.4.5. Microtubules were attached to glass surfaces via MUTAB AuNRs *in vitro*

To rule out that the colocalizations were TEM preparation and fixation artifacts, AuNRs were incubated with microtubules under physiological buffer conditions *in vitro* and imaged with IRM [101] (Fig. 3.8B). To this end, a MUTAB AuNR solution was incubated in clean microfluidic glass chambers. AuNRs attached to the negatively charged glass surface most likely due to electrostatic interactions. While microtubules interacted loosely with untreated glass surfaces, the addition of microtubule solution to an AuNR covered glass surface yielded microtubules that appeared stably bound to the surface via AuNRs during video observation (Fig. 3.8B). To fix the microtubules reliably to the surface, this assay required a high density of AuNRs. Therefore, this assay and was designed rather as a quick microtubule-AuNR interaction test.

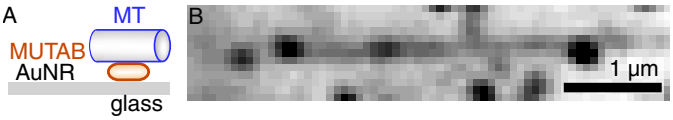

Figure 3.8.: Schematic (**A**) and IRM image (**B**) of microtubules bound to the glass surface via MUTAB AuNRs.

3.4.6. AuNRs were visualized using TIRF microscopy

To achieve a greater experimental flexibility and to introduce a selective marker, AuNRs were visualized via TIRF microscopy. As the so-far-used AuNRs were not plasmonically luminescent at the available TIRF excitation wavelength of 561 nm, two options were explored. First, AuNRs that were not plasmonically excitable with the TIRF laser were labeled with a fluorescent dye during the MUTAB functionalization. Second, plasmonically excitable AuNRs were MUTAB functionalized (Fig. 3.9A).

For the fluorescent labeling, a rhodamine B derivative (RH-PEG-SH, Molecule 3 in Fig. 3.9A) with a positive charge and a 3.4 kDa polyethylene glycol (PEG) linker with 21 nm contour length was chosen to prevent quenching by the AuNRs [155, 158, 213, 249, 250]. Due to the cationic nature of the rhodamine derivate, the rhodamine labeling had no effect on the measured zeta potential of 30 ± 5 mV (mean $\pm$ SD, $N = 3$). Most likely due to the rhodamine PEG linker, a small increase in the hydrodynamic radius of 49 ± 3 nm (mean $\pm$ SD, $N = 3$) was observed, based on DLS measurements. Compared to the unlabeled MUTAB AuNRs (grey line in Fig. 3.9C), the rhodamine labeled MUTAB AuNRs (RL-AuNRs) showed a small shoulder around the absorption maximum of the rhodamine derivate at 570 nm at the transverse LSPR peak. This shoulder was most likely due to the rhodamine labeling. Gaussian fits (see Appendix A.4) to the L-LSPRs revealed that the RL-AuNRs were red shifted by 7.2 nm compared to the unlabeled

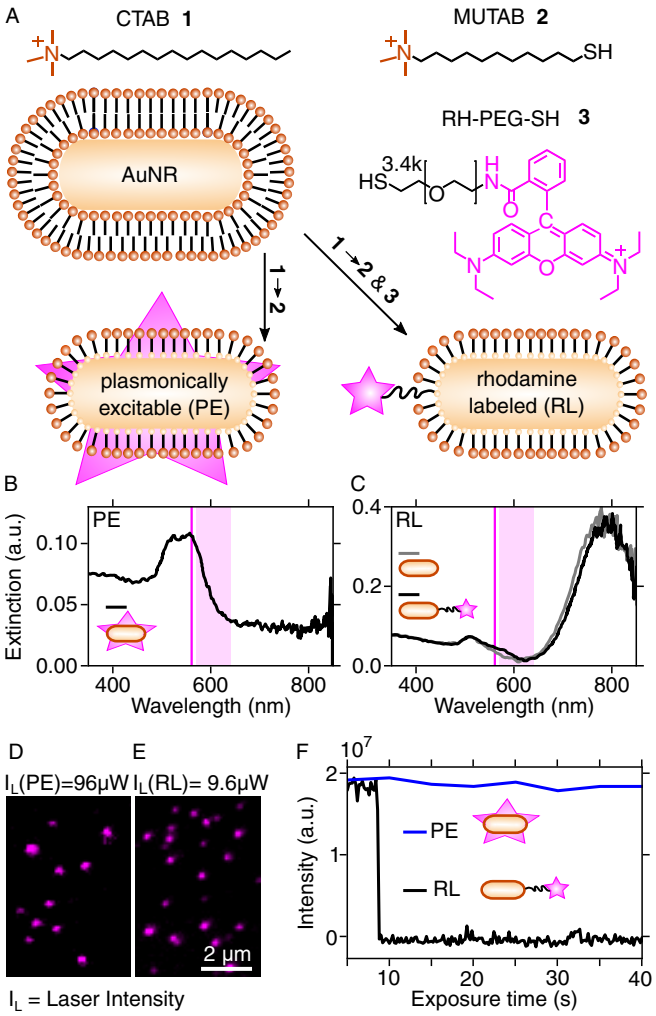

Figure 3.9.: (**A**) CTAB (Molecule 1) coated AuNRs are functionalized either with MUTAB (Molecule 2) when plasmonically excitable or with MUTAB and a rhodamine B derivate (Molecule 3) when plasmonically inactive at the excitation wavelength. Extinction spectra of MUTAB AuNRs that are plasmonically excitable (PE, black line in **B**) or plasmonically inactive (**C**). The laser excitation wavelength of 561 nm is indicated as a magenta line and the detection range as magenta box. Plasmonically inactive MUTAB AuNRs in (**C**) are either unlabeled (grey line) or rhodamine labeled (RL, black line). PE- and RL-MUTAB-AuNRs were visualized using TIRF microscopy (**D** and **E**). PE-AuNRs (blue line in **F**) did not bleach while RL-AuNRs (black line) bleached.

MUTAB AuNRs. This shift suggested that the L-LSPR was sensitive to the rhodamine label. As the rhodamine label was detected with a longitudinal plasmon mode, the label was most likely tip bound. In Fig. 3.9, the available laser excitation wavelength of 561 nm is marked as a vertical magenta line and the red channel, defined by the bandpass filter described in methods Sect. 3.3.2.2, as a magenta coloured box. The extinction spectra of the plasmonically excitable MUTAB AuNRs (PE-AuNRs) in water (black line in Fig. 3.9B) shows that the L-LSPR overlaps with the 561 nm laser (magenta line). Thus, the plasmon luminescence was expected in the red channel (magenta box). Indeed, both the RL-AuNRs and PE-AuNRs could be successfully imaged with TIRF microscopy (Fig. 3.9D and E). However, compared to the RL-AuNRs, the PE-AuNRs required a 10-fold higher excitation laser intensity for the same exposure time (200 ms, Fig. 3.9D and E) or longer exposure times for the same laser intensity (9.6 μW, Fig. 3.9F) to achieve luminescence intensities comparable to the RL-AuNRs. Furthermore, variations in brightness were observed among the individual AuNRs, that were most likely due to

the different orientations of the AuNRs relative to the polarized laser light [224,251,252]. Bleaching measurements (Fig. 3.9F) confirmed that the PE-AuNRs (blue line) did not blink or bleach while RL-AuNRs (black line) showed bleaching steps. 87 % ($N = 201$) of the bleaching steps observed for RL-AuNRs were single steps and 13 % were double steps, suggesting that most AuNRs were labeled with one fluorophore.

3.4.7. Fluorophore labeled AuNRs colocalized with microtubules *in vitro*

Next, I investigated whether it was possible to localize RL-AuNRs that were bound to microtubules *in vitro* and if the nonspecific interactions between these AuNRs and the surface could be minimized. First, I tested the microtubule immobilization assay based on hydrophobic interactions already described in Sect. 1.3.6.1 [113,253]. Antibodies were adsorbed to the surface and, afterwards, the remaining surface was blocked with Pluronic F127 (Fig. 3.10A). Subsequently, microtubules were attached to the surface and then incubated with RL-MUTAB AuNRs [121,254]. In this manner, the AuNR concentration could be optimized. In the IRM image, proteins or AuNRs located close to the surface appeared as dark signals due to destructive interference [101]. An elongated microtubule was visible with three colocalizing dark spots (Fig. 3.10B). As both, small microtubule fragments and impurities, generated dark, point-like IRM signals comparable to AuNRs, AuNRs could not be clearly identified. Thus, a simultaneous TIRF imaging of the rhodamine labels was performed (Fig. 3.10C). Two of the microtubule-bound dark IRM spots colocalized with the TIRF signals (Fig. 3.10D) and were identified as microtubule-bound AuNRs. The colocalizing dark spot visible in IRM but not in TIRF could be an impurity or an AuNR missing a rhodamine label. Overall, AuNRs bound microtubules under physiological buffer conditions *in vitro*, interacted only sparsely with the passivated surface and were reliably identified using simultaneous IRM and TIRF microscopy [121].

For WGM measurements, microtubule-bound AuNRs should attach close to the resonator surface to keep the AuNR antenna in the near-field of the resonator [158, 181–183]. However, antibody-attached microtubules were located about 15 nm above the surface according to Sect. 1.4.2. For an APTES monolayer, a coating thickness of about 1 nm is expected [255]. In Sect. 1.4.2 it was shown that the APTES attachment reduced the distance between microtubules and the surface partially, compared to antibody-attachement. At those areas where microtubules were located close to the APTES surface, the microtubule-bound AuNR nanoantenna may efficiently couple to a whispering-gallery mode. Therefore, the microtubule-AuNR assay was tested on APTES-functionalized surfaces (Fig. 3.10E–H). Due to the positive charge of the APTES surface and the MUTAB AuNRs, it was expected that the electrostatic interaction was repulsive between the two. To test whether AuNRs were repelled by the surface and only attracted by the microtubules, a high concentration of AuNRs was used. Microtubules were first bound to the surface and then incubated with rhodamine-MUTAB AuNRs that were concentrated 10-fold higher compared to Fig. 3.10B–D. As expected, the outline of a microtubule could be marked with a high AuNR decoration

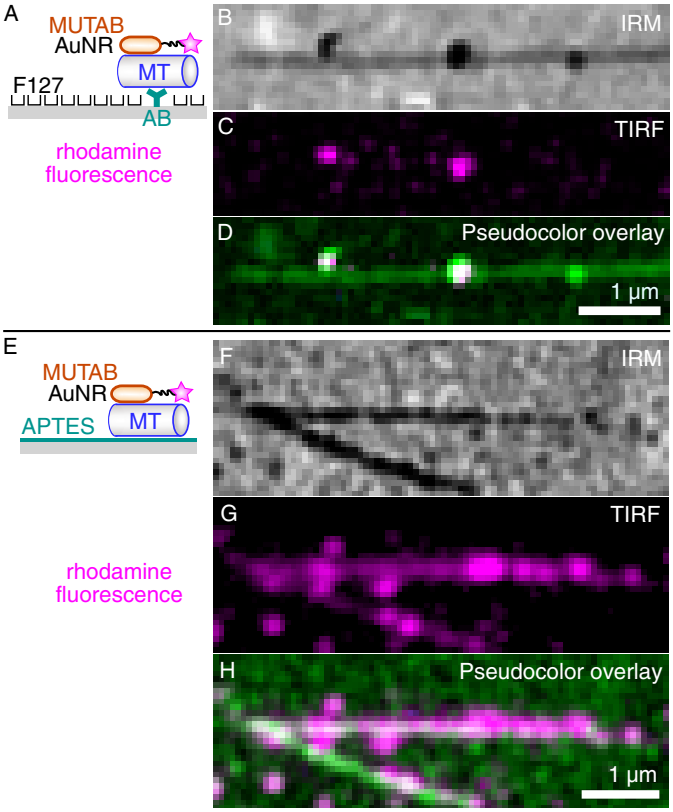

Figure 3.10.: (**A**) RL-MUTAB AuNRs were bound to a microtubule (blue) that was surface-bound via an antibody (AB, cyan) to a surface (gray) that was passivated with adsorbed Pluronic F127. (**B**) IRM, (**C**) TIRF and (**D**) IRM-pseudocolor-TIRF overlay image of single RL-MUTAB AuNRs bound to a single microtubule. (**E**) RL-MUTAB AuNRs attached to a microtubule (blue) bound to an APTES (cyan) coated surface (gray). (**F**) IRM, (**G**) TIRF and (**H**) IRM-pseudocolor-TIRF overlay image of multiple RL-MUTAB AuNRs bound to two single microtubules.

density (Fig. 3.10G and H). Taking a closer look at the IRM image (Fig. 3.10F), two microtubules were visible with a homogeneously grey contrast decorated by black spots. Based on TIRF images, these dark spots are most likely AuNRs (Fig. 3.10G). A high density of rhodamine labeled AuNRs marks the outline of the microtubules. However, not all dark areas in the IRM image appeared in the TIRF image as well. Potentially, these dark areas could be due to a rather inhomogeneous contrast of a microtubule on an APTES surface (see Sect. 1.4.2) or could indicate AuNRs bound in such close proximity, that their rhodamine labels are quenched by their neighbours. Importantly, most AuNRs were bound to microtubules and not to the remaining surface. Microtubule binding may have been favoured by the polycationic MUTAB AuNRs. Possibly, the few AuNRs that appeared attached to the surface were bound to microtubule fragments or individual tubulin molecules.

In summary, microtubules were directly attached to an APTES functionalized surface and their outline could be visualized in TIRF by colocalizing AuNRs [121].

3.4.8. Plasmonically excited AuNRs bound to microtubules were detected using TIRF microscopy

To be independent of fluorescent labels, have blink- and bleach-free probes, the plasmonically excitable MUTAB AuNRs (PE-AuNRs, Fig. 3.9) were incubated with APTES-attached microtubules (Fig. 3.11A). The exemplary microtubule visible in the IRM image of Fig. 3.11B was unevenly attached to the surface and was partially elevated tens of nanometers relative to the surface (white sections). The corresponding TIRF image (Fig. 3.11C) was acquired under the same imaging conditions as Fig. 3.10C and G, and shows the stimulated plasmon luminescence of PE-AuNRs. The IRM-pseudocolor-TIRF overlay (Fig. 3.11D) shows that PE-AuNRs also colocalized with microtubules. Therefore, they can be used as bleach- and blink-free microtubule probes. A closer look at the IRM image shows dot-like structures along the microtubule that were not visible in TIRF. Possibly, these could correspond to nonfluorescent impurities. Alternatively, not all microtubule-bound AuNRs were excited and imaged with the TIRF setup. This could be due to the different orientations of the AuNRs relative to the polarized laser light [224,251,252,256]. Additionally, the LSPR of the PE-AuNRs may have been shifted upon microtubule attachment to other spectral regions and therefore was neither excited nor detected with the setup. The magnitude of the L-LSPR shift may depend on the orientation of the AuNR to the microtubule, as well.

Overall, PE-AuNRs colocalized with microtubules and could—at least partially—be detected using IRM and TIRF [121].

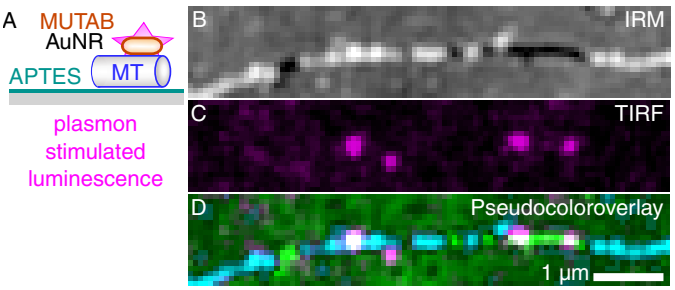

Figure 3.11.: (**A**) APTES (cyan) coated surfaces (gray) were incubated with microtubules (blue) and plasmonically excitable (PE, magenta star) MUTAB AuNRs. (**B**) IRM, (**C**) TIRF and (**D**) IRM-pseudocolor-TIRF overlay image of single PE MUTAB AuNRs bound to a single microtubule.

3.4.9. MUTAB AuNRs rarely colocalized with kinesin Kip3

To investigate, whether MUTAB AuNRs interacted strongly with kinesins, the kinesin Kip3 was incubated with microtubules (Fig. 3.12A). Upon Kip3 addition there was autofluorescence visible in the red channel. After a washing step, highly concentrated RL-AuNRs were added. The high concentration increased the chance that the red channel signals were due to AuNRs. Interestingly, Kip3 moved rather undisturbed along the microtubule (Fig. 3.12B), while the majority of the AuNRs diffused throughout the

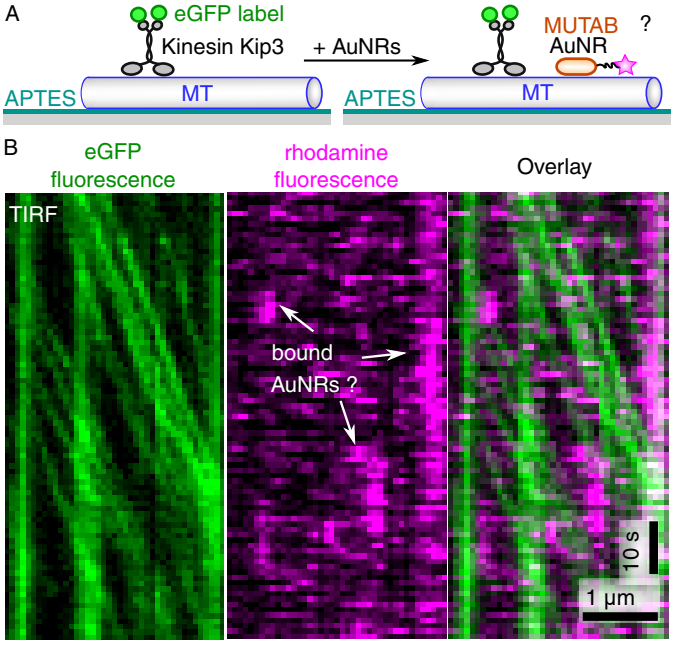

Figure 3.12.: (**A**) Schematic of the kinesin-AuNR-microtubule assay performed on an APTES functionalized surface. (**B**) Kymographs based on TIRF images showing the green fluorescence of eGFP-labeled kinesins and the magenta fluorescence of rhodamine-labeled AuNRs. Potentially, microtubule-bound AuNRs may be visible and are labeled with white arrows.

sample without binding. Note that the kymograph in Fig. 3.12B only shows 1D motion with a 1 s time resolution suited to image the Kip3 motion, while the AuNRs diffused much faster in 3D throughout the whole sample. Therefore, only short AuNR colocalization events were visible in the rhodamine channel of the kymograph. A stably bound AuNR shows up as a straight vertical line in a kymograph. Three different positions are indicated with white arrows that mark potential microtubule-bound AuNRs (Fig. 3.12B). The fluctuations in the horizontal axis either suggested that the AuNRs were loosely bound or were due to the superposition of the stably-bound AuNRs with diffusing AuNRs. However, due to the presence of autofluorescent contamination, single events could not be clearly related to AuNRs. MUTAB AuNRs rarely colocalized with microtubules within this assay which might suggest that ingredients of the kinesin assay disturbed the AuNR-microtubule interaction. Kinesins were not hindered by the presence of AuNRs. Bound AuNRs may have been bypassed by stepping sidewards on the microtubule lattice [235]. In summary, MUTAB AuNRs most likely did not interact strongly with kinesins beneficial for potential future whispering-gallery-mode measurements.

3.4.10. Whispering-gallery-mode measurements suggested unexpected surface properties of the resonator

The AuNR-microtubule assays on the whispering-gallery-mode resonator revealed many additional challenges. To begin with, APTES functionalization of the resonator surface resulted in a loss of sensing functionality. Most likely, the APTES solution already contained polymers. The deposition of large APTES polymers instead of monomers may have caused a strong mode broadening accompanied by the loss of the sensing func-

tionality. Furthermore, the addition of PEM buffer alone to a bare resonator caused a mode broadening and an increased noise level that made it difficult to perform measurements. Upon addition of other assay components, a rapid mode broadening and an increase of noise could be observed that finally resulted in the loss of the sensor functionality. Most likely, the solvents, buffers and ingredients had impurities that adsorbed at the sensor's surface and perturbed the mode. Using an unfunctionalized sensor and HEPES buffer, conventionally used for whispering-gallery-mode experiments, made it possible to observe a mode shift and broadening during the incubation with microtubules (Fig. 3.13A). Interestingly, the resonance wavelength shift $\Delta\lambda$ increased rapidly until a plateau was reached (Fig. 3.13A). This could possibly indicate, that the concentration of microtubules was high enough to cover the whole surface. After an initial fast increase, the peak broadened almost linearly (ΔFWHM, Fig. 3.13B). In a separate experiment, MUTAB-AuNRs dissolved in water were incubated to a bare and unfunctionalized resonator. Unexpectedly, the polycationic AuNRs did not bind to the surface but only shortly interacted with the resonator, as indicated by the peaks in Fig. 3.13C and D. As the resonator was fabricated from a glass fibre, the negative charge at neutral pH was expected to repel microtubules and attract the polycationic AuNRs. As the opposite behaviour was observed, it could potentially be that the laser-melted material had a positive net charge. Together, these observations suggested, that the surface chemistry of the resonator was different than expected.

Many challenges still need to be met. Microtubules need to bind stably, the remaining surface needs to be passivated sufficiently, the AuNRs need to colocalize with microtubules while being as close as possible to the resonators equatorial surface, and kinesins need to bypass the most sensitive near-field of the AuNRs. Throughout all functionalization steps, the resonator requires to remain functional and sensitive enough to detect single molecules such as kinesins and ATP. However, every binding molecule contributes to the broadening of the resonance peak and the reduction of the sensitivity of the sensor.

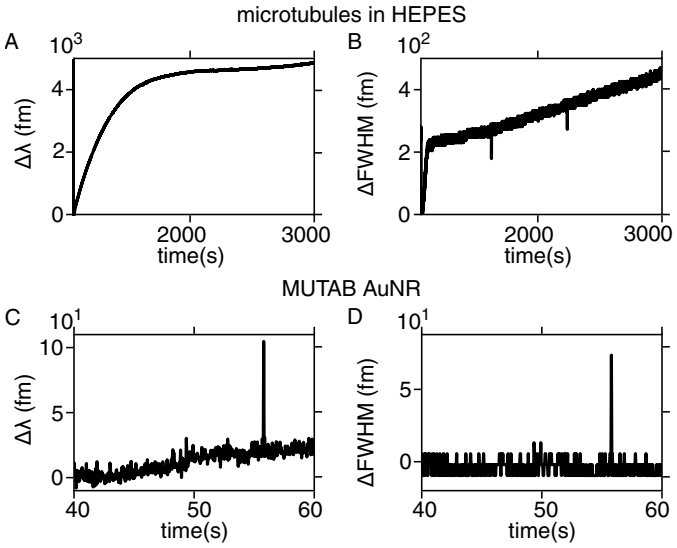

Figure 3.13.: Microtubules were incubated to a bare, unfunctionalized resonator which resulted in a resonance wavelength shift (**A**) and peak broadening (**B**). The incubation of polycationic MUTAB AuNRs to a bare resonator only caused short interaction events (**C** and **D**), indicating no longterm binding to the surface.

3.5. Conclusion & Outlook

Gold nanorods were synthesized and functionalized to generate charge-stabilized, polycationic MUTAB AuNRs (Fig. 3.3). These AuNRs did bind directly to microtubules under physiological buffer conditions in TEM and *in vitro* assays (Fig. 3.6–3.8 and Fig. 3.10–3.11). Thus, no protein coatings that would block the AuNRs' plasmonic near-field were necessary to mediate the interaction between AuNRs and microtubules. Thereby, the functionality of the AuNRs as LSPR sensor remained intact and refractive index changes, most likely due to microtubule binding, were observed (Fig. 3.5). TEM analysis revealed that the MUTAB AuNRs prefered to bind to microtubules over binding to free tubulin (Fig. 3.7). Furthermore, *in vitro* assays showed that the polycationic MUTAB AuNRs did not bind to positively charged APTES surfaces but specifically to the negatively charged microtubules (Fig. 3.10G and 3.11). Most likely, the AuNR-microtubule binding was due to electrostatic interactions. The AuNR binding orientations were further investigated using TEM images (Fig. 3.6 and 3.7B). In the free tubulin containing TEM samples, microtubule bundling with intercalated AuNRs was frequently observed and the amount of clusters increased most likely due to free tubulins that crosslinked AuNRs. In pure buffer without proteins, clustering was rarely observed due to the charge-stabilization of the polycationic AuNRs. Furthermore, high concentrations of AuNRs could be used to mark the outline of microtubules (Fig. 3.10). Considering the AuNRs' preference to bind to negatively charged microtubules, the AuNRs could potentially be used to mark other negatively charged molecules, proteins or organelles. While *in vitro* assays can be designed to contain only one negatively charged protein or organelle that can be specifically marked with the AuNRs, *in vivo* experiments would rather employ the AuNRs as negativity markers that would interact most with negatively charged surfaces. For the visualization of the AuNRs in TIRF, AuNRs were labeled with rhodamine (Fig. 3.9). To prevent quenching [155], the positively charged rhodamine derivate was coupled via a PEG linker to the AuNRs.

Furthermore, the plasmonic luminescence of the AuNRs could be excited and visualized in TIRF without fluorophore labels. The blink- and bleach-free plasmonic microtubule markers allowed the label-free longtime observation of microtubules via TIRF microscopy. However, comparing the IRM and TIRF images, it appeared likely that not all microtubule-bound plasmonic AuNRs could be visualized with the used TIRF settings. It would be interesting to excite the microtubule-bound AuNRs with different wavelengths and laser polarizations and compare their luminescence response. Potentially, the plasmonic near-field of the AuNRs could interact with other fluorescently labeled analytes such as kinesins moving along a microtuble. That would enable a colocalization with nm precision due to enhancement or quenching of the analytes dye [158].

The AuNRs could potentially serve as roadblocks to investigate how obstacles are overcome by microtubule-based motors [235,257–259]. When the motor, e.g. a kinesin, walks into the plasmonic near-field of the AuNR, a transient increase or decrease in fluorescence intensity might occur and correlate with a pause or slow down of the translocation

when the obstacle is bypassed. Preliminary measurements with the kinesin Kip3 and a high AuNR concentration did not show AuNR-Kip3 colocalizations. This is beneficial for the potential usage of AuNRs as roadblocks as it suggests that the kinesins may bypass AuNR obstacles without binding irreversibly. In the future, MUTAB AuNRs could potentially be utilized as nanoantennas enhancing the detection of whispering-gallery modes to allow insight into the molecular machinery of motor proteins. Preliminary measurements with a whispering-gallery mode resonator showed that the so far developed assays were not applicable to the resonator's surface and that most likely, a higher level of cleanliness would be required for further measurements. Also, to develop a functional microtubule-AuNR-kinesin assay for whispering-gallery-mode resonators, a better understanding of the surface properties of the resonator is required. It would be interesting to measure the zeta potential of the bare resonator surface to understand the observed microtubule attachment and MUTAB AuNR repulsion. A positive surface charge of the bare resonator would make a further APTES silanization unnecessary. Circumventing an APTES functionalization would be beneficial as this functionalization destroyed the resonator's sensor functionality. Alternatively, a vapour phase silanization of a nonpolymerizing silane would succeed in keeping the sensor intact. However, the best silanization and microtubule attachment strategy remains unclear. The challenge is to develop a microtubule-kinesin assay, in which microtubules are rigidly and directly fixed to the surface while keeping the sensing functionality intact. Additionally, the surface requires to be passivated against the binding of kinesin molecules. Any unspecific kinesin attachment would further broaden the mode and decrease the resonator's sensitivity. To develop a suited assay, frequent and regular testing of the assay components and resonator functionality would be required on site in Exeter.

4. Conclusion & Outlook

Kinesin-microtubule interactions are essential for biological processes such as cell division and cellular transport [1]. These interactions are typically investigated using surface-sensitive detection methods. To monitor the native interaction of kinesins and microtubules, a label-free detection is required. However, kinesins have only been detected when labeled with a fluorescent dye or nanoparticle. Since kinesins are large molecules, a label-free detection with interferometric scattering microscopy (iSCAT) may be envisioned. Alternatively, highly sensitive plasmonic near-fields of AuNRs may detect bypassing kinesins. In combination with whispering-gallery modes, these AuNR nanoantennas may sense even conformational changes of a kinesin and help to relate conformational with chemical changes. For an optimal detection via such surface-sensitive methods, high-quality surfaces offering a high SBR are required. Microtubule-kinesin assays yielding sufficiently high SBRs are complex and frequently show issues in reproducibility [6].

Therefore, I developed a reproducible glass surface hydrophobization procedure by combining a new plasma activation approach using PP holders with HMDS silanization (Chapter 1). XPS control measurements showed that the underlying plasma activation barely modified the chemical composition of the glass surface. Kinesin-single-molecule measurements confirmed that microtubules were rigidly attached to the surface with a high SBR and that the motility of the kinesin remained intact. Interestingly, surfaces hydrophobic by definition ($CA > 90\,deg$) were not required as stated by literature [18] but CAs of about 87 deg yielded optimal results. Compared to the original protocol, the amount of required solvents was reduced by a factor of 3, the active work time was reduced to a minimum, and reproducibility and surface quality had improved drastically. Therefore, the protocol was commonly used in our laboratory and is expected to be beneficial for other laboratories as well. Furthermore, it was shown that antibodies attached most likely in an upright orientation to the hydrophobic surfaces and that antibody-attached microtubules were located in average about 15 nm above the surface. Microtubule-attachment via APTES-silanized surfaces partially increased the microtubule contrast and partially reduced the microtubule-surface distance. The increased SBR may be beneficial for measurements requiring an optimized microtubule contrast, such as iSCAT measurements, or a closer microtubule-surface distance, such as WGM measurements.

Another way to increase the label-free contrast of a signal is to reduce the background by further data processing such as the iSCAT processing (Chapter 2). The ratiometric imaging incorporated into the iSCAT mode of a custom-written camera program re-

moved the static background of a sample such that the dynamic features were visible and more pronounced. Additionally, the direction of movement could be identified from the black-and-white pattern of the iSCAT signal. Thus, information about movement and direction could be recorded in a single image without the necessity to record multiple images over time. While conventionally, iSCAT is performed "blindly" as image postprocessing after the measurement, the real-time iSCAT imaging enables a direct optimization of the sample conditions while imaging. The program performed even faster than required for the detection of small proteins according to the literature [144]. Most likely, the program's performance will be sufficient to image single kinesin molecules. The combination of simultaneous IRM and iSCAT imaging will be useful, as static microtubules can be visualized in IRM and the dynamic kinesin movement will be visible in iSCAT. Probably, the illumination and detection paths of the setup will have to be optimized further until the desired sensitivities are achieved.

A label-free detection of kinesins with even higher sensitivities can be envisioned to be based on plasmonics. To bring the plasmonic near field of gold nanorod antennas close to "walking" kinesins, AuNRs were bound to microtubules. These AuNRs were MUTAB functionalized to bind the microtubules via electrostatic interactions. In this manner, no protein coatings to mediate the interaction between AuNRs and microtubules were necessary that would have blocked the sensitive plasmonic near-field of the AuNRs. Thereby, the functionality of the AuNRs as LSPR sensor remained intact and refractive index changes were observed, that were most likely due to microtubule binding. This microtubule-AuNR binding was confirmed via multiple TEM and *in vitro* assays under physiological buffer conditions. For TIRF visualization, rhodamine-labels were introduced or the plasmonic luminescence was excited. At high concentrations, microtubule outlines could be marked with AuNRs. The data suggested that MUTAB AuNRs could be used as bleach- and blink-free microtubule markers. Potentially, MUTAB AuNRs could also serve as negativity markers for other proteins or organelles. The MUTAB AuNRs have not been observed to interact with kinesins translocating along microtubules. Potentially, the kinesin Kip3 can bypass microtubule-bound AuNRs [235]. If such a Kip3-AuNR-microtubule assay was performed on a WGM resonator, a kinesin bypassing an AuNR potentially may be detected in future measurements. However, the so far developed assays could not yet be applied to the resonator's surface. The surface chemistry of the resonator was different than expected. The incubation of most chemicals and assay ingredients did destroy the sensing functionality when applied to the resonator. To develop a functional assay in the future, frequent experiments directly on the resonator setup are necessary.

In the future, the reproducible generation of high-quality surfaces is expected to enable more reproducible results for a variety of microtubule-kinesin experiments. The direct observation of unlabeled, single kinesins in iSCAT would offer a variety of possibilities. The motility parameters of an unlabeled, native kinesin may be studied for the first time. For a mass-calibrated iSCAT, the contrast of kinesins may be related to monomeric or multimeric states of kinesins without measurement artefacts such as bleaching or blink-

ing. Potentially, kinesins may be identified that dissociate from microtubules together with a kinesin-bound tubulin dimer or multimer. Such observations would help to develop models for essential processes such as microtubule aging or depolymerization. An even more sensitive detection based on AuNR nanoantennas and WGMS may enable the detection of conformational changes of a kinesin molecule. As such measurement techniques are able to detect single ions, the conformational changes of the kinesins may be related with the state of bound ATP. The relation of the ATP state and the conformational changes may improve the model of the kinesin stepping cycle.

A. Appendix

A.1. Significance of contact angle differences

Table A.1.: Significances of contact angle (CA) differences determined via ANOVA ($N = 432$, $F = 404$, $\alpha = 0.01$, confidence interval CI = 99 %) with Tukey HSD post hoc. CAs were measured for HMDS silanized glass surfaces with different preceding activations. The respective CA data can be found in Table A.3.

Group 1	**Group 2**	**Diff**	**p value**	**CI**
O_2	air	1.70	2.92E-5	[0.47–2.93]
O_2	$O_2 + TE$	3.60	6.69E-14	[2.41–4.79]
O_2	$N_2 + TE$	4.24	6.69E-14	[3.01–5.47]
O_2	$O_2 + PP$	9.23	6.69E-14	[8.01–10.46]
O_2	HCl	8.63	2.92E-5	[7.40–9.86]
O_2	air + PP	8.83	6.69E-14	[7.61–10.06]
O_2	air + TE	1.94	8.47E-7	[0.71–3.17]
air	$O_2 + TE$	5.30	6.69E-14	[4.17–6.44]
air	$N_2 + TE$	2.54	9.68E-13	[1.37–3.71]
air	$O_2 + PP$	7.53	6.69E-14	[6.34–8.70]
air	HCl	6.92	6.69E-14	[5.75–8.10]
air	air + PP	7.13	6.69E-14	[5.96–8.30]
air	air + TE	0.23	1.00	[-0.94–1.40]
$O_2 + TE$	$N_2 + TE$	7.84	6.69E-14	[6.71–8.98]
$O_2 + TE$	$O_2 + PP$	12.83	6.69E-14	[11.70–13.97]
$O_2 + TE$	HCl	12.23	6.69E-14	[11.09–13.36]
$O_2 + TE$	air + PP	12.43	6.69E-14	[11.30–13.57]
$O_2 + TE$	air + TE	5.54	6.69E-14	[4.40–6.67]
$N_2 + TE$	$O_2 + PP$	4.99	6.69E-14	[3.82–6.16]
$N_2 + TE$	HCl	4.39	6.69E-14	[3.21–5.56]
$N_2 + TE$	air + PP	4.59	6.69E-14	[3.42–5.76]
$N_2 + TE$	air + TE	2.31	1.43E-10	[1.13–3.48]
$O_2 + PP$	HCl	0.61	0.60	[-0.57–1.78]
$O_2 + PP$	air + PP	0.40	0.93	[-0.77–1.57]
$O_2 + PP$	air + TE	7.30	6.69E-14	[6.13–8.45]
HCl	air + PP	0.21	1.00	[-0.97–1.38]
HCl	air + TE	6.69	6.69E-14	[5.52–7.86]
air + PP	air + TE	6.90	6.69E-14	[5.73–8.07]

A.2. Contact angles

Table A.2.: Contact angles (CA) in degree, measured for different cleaning treatments performed in a clean room facility. Left and right CAs of 12 droplets were acquired for for 3 different samples per batch and 6 to 7 different batches per method. Mean ± SD (N).

No.	**HCl OTES**	**O_2 + TE OTES**	**HCl TMCS**	**O_2 + TE TMCS**	**HCl HMDS**	**O_2 + TE HMDS**
1	86.4 ± 2.8 (72)	72.3 ± 3.5 (72)	67.6 ± 4.5 (72)	28.4 ± 1.4 (50)	92.6 ± 0.7 (72)	61.4 ± 5.4 (62)
2	91.3 ± 1.2 (72)	85.7 ± 2.3 (72)	68.1 ± 4.0 (72)	45.9 ± 3.3 (72)	84.8 ± 1.5 (72)	78.6 ± 3.0 (72)
3	85.6 ± 0.9 (72)	78.8 ± 0.8 (72)	70.8 ± 3.8 (72)	69.7 ± 2.0 (72)	83.4 ± 0.8 (72)	84.1 ± 1.4 (72)
4	85.1 ± 1.0 (72)	80.6 ± 2.5 (72)	62.7 ± 3.6 (72)	39.6 ± 1.9 (72)	85.3 ± 0.8 (72)	82.6 ± 1.3 (72)
5	84.5 ± 2.0 (72)	77.3 ± 1.7 (72)	59.3 ± 1.7 (72)	37.8 ± 2.7 (72)	90.6 ± 1.2 (72)	73.5 ± 4.7 (72)
6	88.3 ± 1.2 (72)	85.2 ± 0.9 (72)	59.9 ± 2.5 (72)	57.3 ± 1.8 (72)	84.4 ± 1.3 (72)	82.3 ± 0.7 (72)
7	-	-	-	-	-	58.2 ± 11.5 (72)
All	86.9 ± 2.8 (432)	80.0 ± 5.1 (432)	64.7 ± 5.6 (432)	47.4 ± 13.5 (410)	86.9 ± 3.6 (432)	74.6 ± 11.1 (494)

Table A.3.: Contact angles (CA) in degree, measured for HMDS silanized glass surfaces that were treated with different plasmas. Left and right CAs of 12 droplets were acquired for 3 different samples per batch and 6 different batches per method. Mean ± SD (N).

No.	**O_2**	**Air**	**O_2 + PP**	**Air + PP**	**Air + TE**	**N_2 + TE**
1	76.7 ± 1.1 (72)	80.0 ± 1.6 (72)	90.1 ± 1.5 (72)	89.6 ± 2.2 (72)	79.8 ± 2.8 (72)	84.2 ± 1.3 (72)
2	79.7 ± 0.9 (72)	82.2 ± 1.4 (72)	89.1 ± 1.1 (72)	86.4 ± 2.5 (72)	78.9 ± 2.3 (72)	82.6 ± 1.3 (72)
3	78.7 ± 1.0 (72)	81.4 ± 0.8 (72)	89.7 ± 1.2 (72)	86.3 ± 3.4 (72)	79.8 ± 1.7 (72)	82.6 ± 1.1 (72)
4	79.3 ± 0.9 (72)	80.0 ± 0.8 (72)	88.3 ± 1.5 (72)	87.1 ± 1.6 (72)	77.8 ± 1.6 (72)	82.7 ± 1.1 (72)
5	76.7 ± 1.5 (72)	77.2 ± 1.0 (72)	85.1 ± 1.6 (72)	87.6 ± 1.0 (72)	82.6 ± 1.5 (72)	78.8 ± 1.5 (72)
6	-	78.8 ± 1.6 (72)	82.6 ± 2.1 (72)	85.4 ± 1.0 (72)	82.3 ± 3.9 (72)	84.0 ± 0.9 (72)
All	78.2 ± 1.7 (360)	80.0 ± 2.1 (432)	87.5 ± 3.1 (432)	87.1 ± 2.5 (432)	80.2 ± 3.0 (432)	82.5 ± 2.2 (432)

A.3. Fitting of XPS peaks

Table A.4.: Gaussian fit parameters for Si 2p peaks recorded via XPS. Fit parameter ± SD.
$f(x; A, \mu, \sigma, C) = Ae^{-(\frac{x-\mu}{2\sigma})^2} + C$

Sample	A (counts/s)	μ (eV)	σ (eV)	C (counts/s)
untreated	28665.3 ± 9.4	102.5 ± 0.1	0.9 ± 0.1	571.7 ± 5.4
air	27811.2 ± 8.6	102.7 ± 0.1	0.9 ± 0.1	539.7 ± 5.0
air + PP	27662.4 ± 8.8	102.7 ± 0.1	0.9 ± 0.1	406.7 ± 5.1

Table A.5.: Skewed Gaussian fit parameters for XPS O 1s peaks. Fit parameter ± SD.
$f(x; A, \mu, \sigma, \gamma, C) = \frac{A}{\sigma\sqrt{2\pi}} e^{-(\frac{x-\mu}{2\sigma})^2}(1 + erf(\frac{\gamma(x-\mu)}{\sigma\sqrt{2}})) + C$.

Sample	A (counts/s)	μ (eV)	σ (eV)	γ (eV)	C (counts/s)
untreated	31523.1 ± 0.1	532.7 ± 0.2	1.4 ± 0.2	-1.3 ± 0.3	31523.1 ± 15.3
air	423281.5 ± 0.1	532.9 ± 0.2	1.3 ± 0.1	-1.3 ± 0.3	31192.8 ± 222.0
air + PP	437368.4 ± 0.1	532.9 ± 0.2	1.4 ± 0.2	-1.3 ± 0.3	31540.8 ± 15.0

As the skewed Gaussian fits did not inform about the peak center, Gaussian fits were performed additionally. To determine the peak center properly with a simple Gaussian, the fit region had to be reduced.

Table A.6.: Gaussian fit parameters for O 1s peaks recorded via XPS. Fit parameter ± SD.
$f(x; A, \mu, \sigma, C) = Ae^{-(\frac{x-\mu}{2\sigma})^2} + C$.

Sample	A (counts/s)	μ (eV)	σ (eV)	C (counts/s)
untreated	95078.5 ± 0.1	532.0 ± 0.1	0.7 ± 0.3	113280.1 ± 0.1
air	83203.2 ± 0.1	532.2 ± 0.1	0.6 ± 0.3	118200.8 ± 0.1
air + PP	74010.0 ± 0.1	532.2 ± 0.1	0.6 ± 0.3	129296.4 ± 0.1

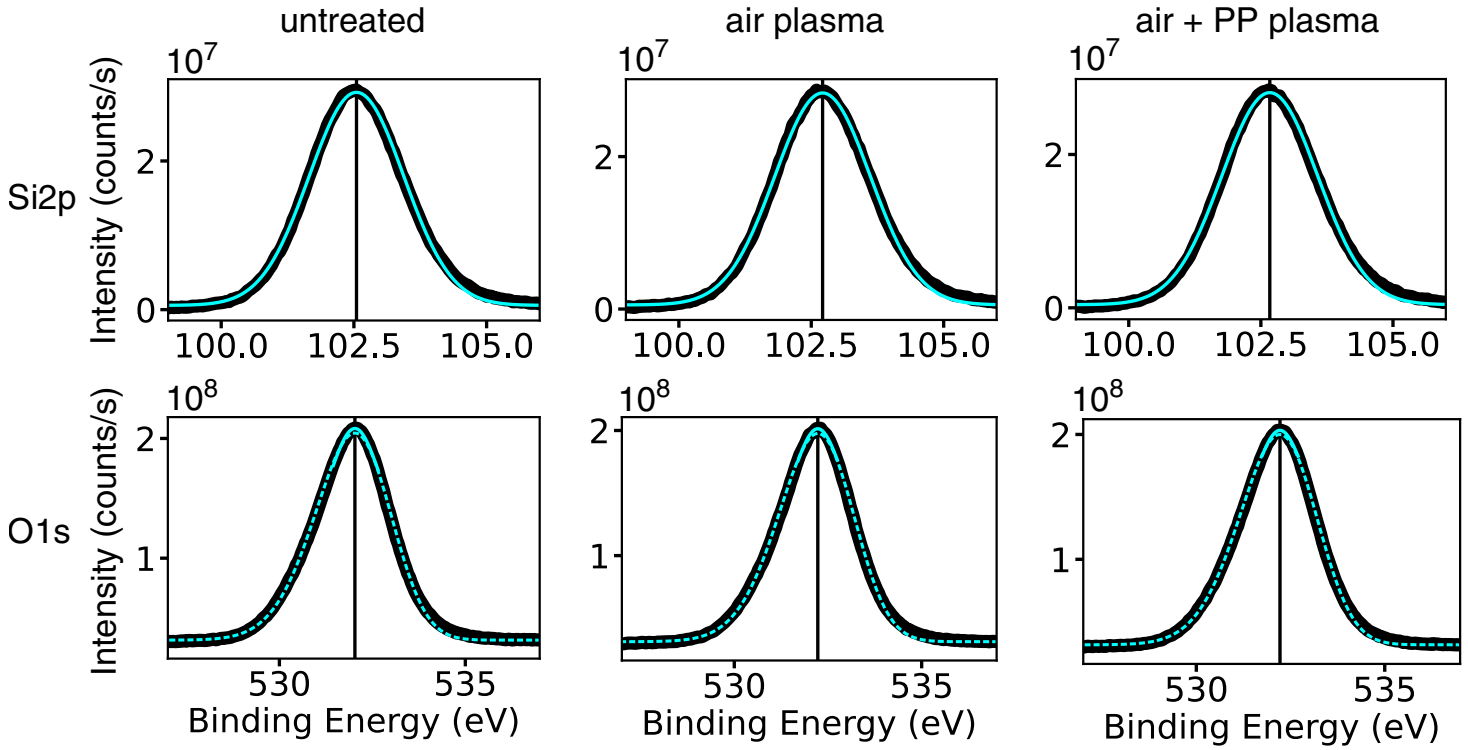

Figure A.1.: Peaks (solid black line), Gaussian fits (solid cyan line), and skewed Gaussian fits (dashed cyan line) of the untreated (left), air plasma (middle) and air + PP plasma (right) treated glass surfaces. Si 2p peaks are shown in the upper and O 1s peaks in the lower row. The peak center determined by the respective Gaussian is indicated by a vertical black line.

A.4. Fitting of L-LSPR peaks

Table A.7.: Gaussian fit parameters for UV/Vis extinction spectra L-LSPR peaks of CTAB AuNRs (C) and MUTAB AuNRs (M) in water (H_2O), PEM buffer (PEM) or PEM-microtubule solution (MTs). Rhodamine labeled AuNRs are indicated with RL. Batches (B) 1 and 2 contain differently shaped AuNRs. Therefore, only measurements within one batch are directly comparable. Note that the results for the undiluted and 1:2 diluted C and M H_2O AuNRs should be the same but appear different possibly due to the increased SNR caused by the dilution. Fit parameter $\pm$ SD.
$(x; A, \mu, \sigma, C) = Ae^{-(\frac{x-\mu}{2\sigma})^2} + C$

B	dil	**Sample**	A (a.u.)	μ (nm)	σ (nm)	C (a.u.)
1	-	C H_2O	0.50 ± 0.05	691.5 ± 0.3	33.1 ± 0.5	0.003 ± 0.055
1	-	M H_2O	0.05 ± 0.03	703.6 ± 0.5	47.6 ± 1.2	-0.006 ± 0.032
1	1:2	C H_2O	0.03 ± 0.03	698.0 ± 0.7	44.4 ± 1.5	-0.001 ± 0.032
1	1:2	C PEM	$0.02, \pm 0.01$	720.2 ± 1.6	56.5 ± 4.6	-0.002 ± 0.001
1	1:2	C MTs	0.02 ± 0.01	717.0 ± 1.3	65.8 ± 10.4	-0.005 ± 0.004
1	1:2	M H_2O	0.03 ± 0.01	715.6 ± 0.7	67.4 ± 4.6	-0.009 ± 0.003
1	1:2	M PEM	0.02 ± 0.01	719.8 ± 1.2	72.4 ± 13.7	-0.008 ± 0.006
1	1:2	M MTs	0.02 ± 0.01	761.6 ± 2.1	41.7 ± 1.7	0.001 ± 0.001
2	-	M H_2O	0.37 ± 0.08	783.3 ± 0.8	60.1 ± 1.2	-0.002 ± 0.084
2	-	M RL H2O	0.29 ± 0.05	790.5 ± 0.9	58.4 ± 1.0	0.014 ± 0.055

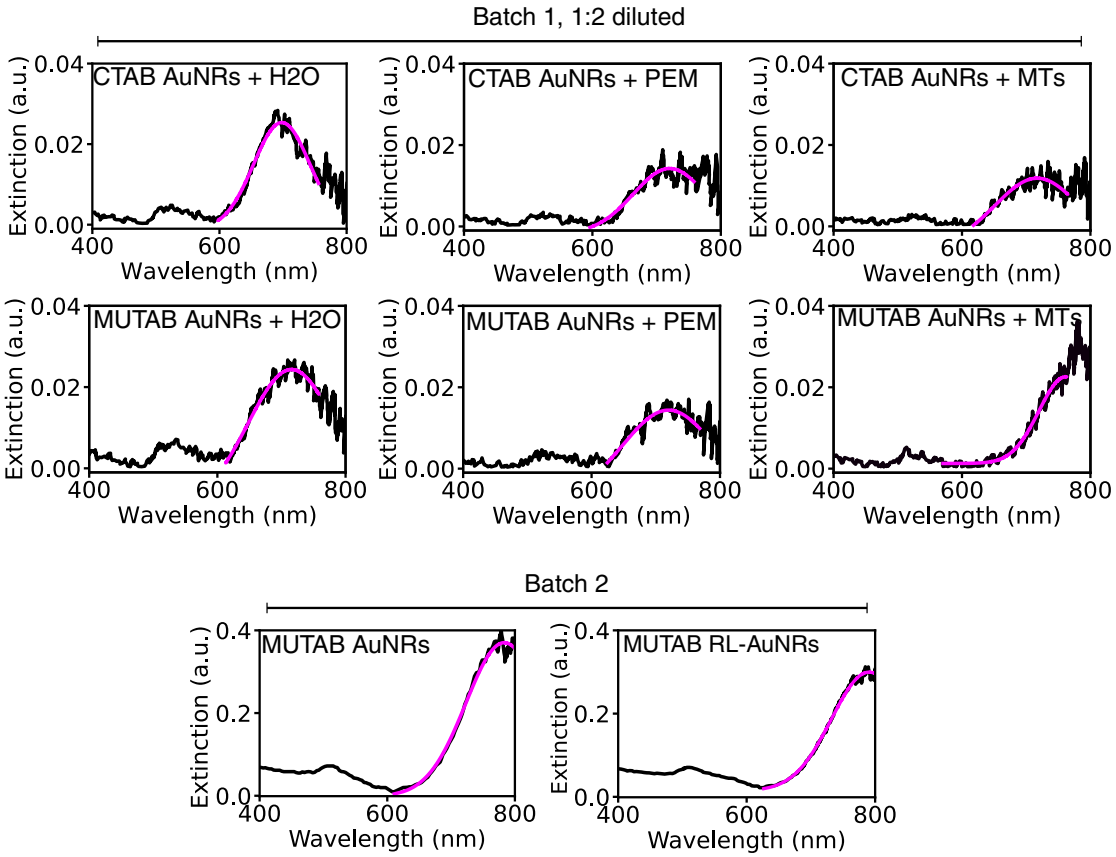

Figure A.2.: UV/Vis extinction spectra (black line) and fits (magenta line) of CTAB and MUTAB AuNRs. Batch 1 and Batch 2 contain differently shaped AuNRs. Therefore, only measurements within one batch are directly comparable. For data and fits of undiluted CTAB and MUTAB AuNRs in H_2O, see Fig. 3.3. Note that the recommended measurement range of the device was 220–750 nm. Thus, increased noise is visible above 750 nm. This noise was very pronounced for the 1:2 diluted samples due to the low overall signal to noise ratio. To reduce the systematic error introduced by this noise, the higher wavelengths were excluded from the fits of the 1:2 diluted AuNRs.

Contributions

Porcine brain tubulin was purified by Anita Jannasch, Michael Bugiel, Shu-Yao Leong. Yeast Kinesin-8 (Kip3-eGFP-His6) was purified by Mayank Chugh. Rat kinesin-1 (truncated rk430-eGFP-His6) was purified by Benedikt Fischer and Shu-Yao Leong. Truncated RAD52 was prepared by Maria Kharlamova. The Fiji-overlay tool used for overlaying IRM and TIRF images was written by Mohammed Abdosamadi. The original Fiji-SBR-analysis tool and Python script was written by Steve Simmert and Gero Hermsdorf. The synthesis protocol for gold nanorods was introduced by Swathi Sudhakar and the AuNRs in Fig. 3.3 were synthesized together with her. Practical student Aylin Kayacik helped synthesize AuNRs. Practical student Fabian Strauß helped synthesize and functionalize AuNRs. The sample presented in Fig. 3.10A was prepared and imaged by Fabian Strauß. TEM images were recorded by York Stierhof in the ZMBP electron microscopy facility. The chemical hexamethyldisilazane was introduced by Carolina Carrasco Pulido. XPS measurements and analysis were performed in cooperation with Dustin Quinones and Prof. Heiko Peisert of the "Interfaces of Organic Semiconductors" group (University of Tübingen, DE). The measurements of RAD52 in Fig. 2.9 were performed by Sandro Münch. Whispering-gallery-mode measurements and analysis was performed in cooperation with Narima Eerqing and Prof. Frank Vollmer (Living Systems Institute, University of Exeter, UK). Erik Schäffer provided the first version of the Cassie's equation derived fit function.

Publications

Published

- Viktoria Wedler, Fabian Strauß, Swathi Sudhakar, Gero Lutz Hermsdorf, York Dieter Stierhof and Erik Schäffer. Polycationic gold nanorods as multipurpose *in vitro* microtubule markers. Nanoscale Advances. 2, 4003, 2020.
- Viktoria Wedler, Dustin Quinones, Heiko Peisert and Erik Schäffer. A quick and reproducible silanization method using plasma activation for hydrophobicity-based kinesin-single-molecule-fluorescence-microscopy assays. Chemistry - A European Journal. 28(64), e202202036, 2022.
- Interferenzreflexionsmikroskop und Verfahren zum Analysieren einer Probe. Sandro Münch, Tom Stumpp, Viktoria Wedler, Anita Jannasch und Erik Schäffer. Patent Anmeldung 01.11.2022 DE 10 2022 128 899.4

List of Figures

List of Tables

List of Abbreviations

ANOVA analysis of variance

APTES aminopropyl-triethoxysilane

ATP adenosine triphosphate

AuNR gold nanorod

BE binding energy

C carbon

C 1s carbon 1s orbital

CA contact angle

CCD charge-coupled device

CH Switzerland

CH_3 methyl

CMOS complementary metal oxide semiconductor

CO carbon monoxide

CO_2 carbon dioxide

CPU central processing unit

CTAB cetyltrimethylammonium bromide

DE Germany

DIC differential interference contrast

DLS dynamic light scattering

E glutamic acid

eGFP green fluorescent protein

EGTA egtazic acid

EM electromagnetic

Exp exposure times

F fluorine

F-127 Pluronic F-127

F 1s fluorine 1s orbital

F KLL fluorine KLL Auger orbital

FWHM full width half maximum

GDP guanosine diphosphate

GMPCPP guanosine-5'-[(α,β)-methyleno]triphosphate

GTP guanosine triphosphate

H_2O water

H_2O_2 hydrogen peroxide

HCl hydrochloric acid

HEPES 2-[4-(2-hydroxyethyl)piperazin-1-yl]ethanesulfonicacid

His6 hexa-histidine tag

HMDS hexamethyldisilazane

HSD honestly significant difference

INA illumination numerical aperture

IRM interference reflection microscopy

iSCAT interferometric scattering

JP Japan

K potassium

K 2p potassium 2p orbital

KE kinetic energy

Kip3 motor protein Kinesin-8, yeast, Kip3-eGFP-His6

KOH potassium hydroxide

L-LSPR longitudinal localized surface plasmon resonance

LED light-emitting diode

LSPR localized surface plasmon resonance

LT Lithuania

MAP microtubule associated protein

$MgCl_2$ magnesium chloride

MT microtubule

MUTAB (11-mercaptoundecyl)-N,N,N-trimethylammonium bromide

N_2 nitrogen gas

Na sodium

Na 1s sodium 1s orbital

Na KLL sodium KLL Auger orbital

O oxygen

O_2 oxygen gas

O 1s oxygen 1s orbital

O KLL oxygen KLL Auger orbital

OH hydroxy

OTES octadecyl-triethoxysilane

PE-AuNRs plasmonically excitable AuNRs

PEG polyethylene glycol

PEM PEM buffer, 80 mM PIPES, 1 mM EGTA, 1 mM $MgCl_2$, pH = 6.9

PEM-T PEM buffer with 1 % Paclitaxel

PEM10 10 % PEM buffer in water

PIPES piperazine-N,N-bis(2-ethanesulfonic acid)

PP polypropylene

R residue

RAM random access memory

RF radio frequency

RL-AuNRs rhodamine-labeled AuNRs

ROI region of interest

SBR signal-to-background ratio

SD standard deviation

Si silicon

Si 2p silicon 2p orbital

Si 2s silicon 2s orbital

sLED superluminescent light-emitting diode

SNR signal-to-noise ratio

T-LSPR transverse localized surface plasmon resonance

TEM transmission electron microscopy

TES triethoxysilane

Ti titanium

TIRF total interference reflection fluorescence

TIRFM TIRF microscopy

TMCS trimethylchlorosilane

TRIS tris(hydroxymethyl)aminomethan

US United States of America

UV/Vis ultraviolet / visible light

WGM whispering gallery mode

XPS x-ray photoelectron spectroscopy

Zn zinc

Zn 2p zinc 2p orbital

List of Symbols

T	temperature
k	Boltzmann constant
e	elementary charge
I	intensity
d_p	penetration depth
z	vertical position
n	refractive index
h	height
λ	wavelength
S	intensity correction factor
D	interference amplitude
ν	frequency of electromagnetic radiation
Φ_{spec}	spectrometer work function
d	thickness
a	area fraction
Θ	contact angle
N	number
N_{MT}	number of kinesins attached to microtubules
N_T	total number of kinesins
N_S	number of kinesins nonspecifically attached to surface
Bkg	background signal
α	significance level of ANOVA test
p	p-value of Tukey post-hoc analysis
CI	confidence interval of Tukey post-hoc analysis
x	position
y	function of x
A	amplitude
μ	center of Gaussian function
σ	standard deviation
m	slope
λ_D	Debye length
d_{glass}	glass surface reference
d_S	distance from glass surface to silane monolayer surface
d_{ABv}	distance from glass surface to upper end of vertically oriented antibody

d_{ABh}	distance from glass surface to upper end of horizontally oriented antibody
f	frame
Av	average of frames f
I_{AvPx}	average pixel intensity
FR_{max}	maximal frame rate
t	time
r	radius
N_p	number of polarizable elements
χ	shape factor
ϵ	dielectric function
λ_{max}	position of the LSPR peak
d_a	adsorbate layer thickness
l_d	decay length of plasmonic EM-field
Q	quality factor, energy loss of a WGM
ω	resonance frequency
λ_{H2O}	L-LSPR wavelength of AuNRs in water
λ_{PEM}	L-LSPR wavelength of AuNRs in PEM buffer

Bibliography

[1] M Schliwa and G Woehlke. Molecular motors. *Nature*, 422(6933):759–765, 2003.

[2] J Howard, AJ Hudspeth, and RD Vale. Movement of microtubules by single kinesin molecules. *Nature*, 342(6246):154–158, 1989.

[3] J Gelles, BJ Schnapp, and Sheetz MP. Tracking kinesin-driven movements with nanometre-scale precision. *Nature*, 331(6155):450–453, 1988.

[4] SM Block, LSB Goldstein, and BJ Schnapp. Bead movement by single kinesin molecules studied with optical tweezers. *Nature*, 348(6299):348–352, 1990.

[5] MP Nicholas, L Rao, and A Gennerich. An improved optical tweezers assay for measuring the force generation of single kinesin molecules. In *Mitosis*, pages 171–246. Springer, 2014.

[6] M Szkop, B Kliszcz, and AA Kasprzak. A simple and reproducible protocol of glass surface silanization for TIRF microscopy imaging. *Anal. Biochem.*, 549:119–123, 2018.

[7] S Sudhakar, TJ Jachowski, M Kittelberger, A Maqbool, GL Hermsdorf, MK Abdosamadi, and E Schäffer. Supported solid lipid bilayers as a platform for single-molecule force measurements. *Nano Lett.*, 19(12):8877–8886, 2019.

[8] RD Vale, TS Reese, and MP Sheetz. Identification of a novel force-generating protein, kinesin, involved in microtubule-based motility. *Cell*, 42(1):39–50, 1985.

[9] J Howard, AJ Hunt, and S Baek. Assay of microtubule movement driven by single kinesin molecules. *Meth. Cell Biol.*, 39:137–147, 1993.

[10] DD Hackney and W Jiang. Assays for kinesin microtubule-stimulated ATPase activity. *Kinesin Protocols*, pages 65–71, 2001.

[11] T Duke, TE Holy, and S Leibler. "Gliding assays" for motor proteins: a theoretical analysis. *Phys. Rev Lett.*, 74(2):330, 1995.

[12] B Nitzsche, V Bormuth, C Bräuer, J Howard, L Ionov, J Kerssemakers, T Korten, C Leduc, F Ruhnow, and S Diez. Studying kinesin motors by optical 3d-nanometry in gliding motility assays. *Meth. Cell Biol.*, 95:247–271, 2010.

[13] WJ Walter, V Beránek, E Fischermeier, and S Diez. Tubulin acetylation alone does not affect kinesin-1 velocity and run length in vitro. *PloS one*, 7(8):e42218, 2012.

[14] F Ruhnow, D Zwicker, and S Diez. Tracking single particles and elongated filaments with nanometer precision. *Biophys. J.*, 100(11):2820–2828, 2011.

[15] V Varga, J Helenius, K Tanaka, AA Hyman, TU Tanaka, and J Howard. Yeast kinesin-8 depolymerizes microtubules in a length-dependent manner. *Nat. Cell Biol.*, 8(9):957–962, 2006.

[16] J Helenius, G Brouhard, Y Kalaidzidis, S Diez, and J Howard. The depolymerizing kinesin MCAK uses lattice diffusion to rapidly target microtubule ends. *Nature*, 441(7089):115–119, 2006.

[17] E Schäffer, SF Nørrelykke, and J Howard. Surface forces and drag coefficients of microspheres near a plane surface measured with optical tweezers. *Langmuir*, 23(7):3654–3665, 2007.

[18] WG Hirst, C Kiefer, MK Abdosamadi, E Schäffer, and S Reber. In vitro reconstitution and imaging of microtubule dynamics by fluorescence and label-free microscopy. *STAR protocols*, 1(3):100177, 2020.

[19] JB Brzoska, IB Azouz, and F Rondelez. Silanization of solid substrates: a step toward reproducibility. *Langmuir*, 10(11):4367–4373, 1994.

[20] AG Lambert, DJ Neivandt, RA McAloney, and PB Davies. A protocol for the reproducible silanization of mica validated by sum frequency spectroscopy and atomic force microscopy. *Langmuir*, 16(22):8377–8382, 2000.

[21] M Zhu, MZ Lerum, and W Chen. How to prepare reproducible, homogeneous, and hydrolytically stable aminosilane-derived layers on silica. *Langmuir*, 28(1):416–423, 2012.

[22] ML Hair and CP Tripp. Alkylchlorosilane reactions at the silica surface. *Colloids Surf. A Physicochem. Eng.*, 105(1):95–103, 1995.

[23] LH Shaffer and EM Flanigen. The hydrolysis of alkyl and aryl chlorosilanes. ii. rates and mechanism of hydrolysis in homogeneous solution. *J. Phys. Chem.*, 61(12):1595–1600, 1957.

[24] SD Chandradoss, AC Haagsma, YK Lee, J-H Hwang, J-M Nam, and C Joo. Surface passivation for single-molecule protein studies. *J. Vis.*, (86):e50549, 2014.

[25] M Ušaj, L Moretto, V Vemula, A Salhotra, and A Månsson. Single molecule turnover of fluorescent ATP by myosin and actomyosin unveil elusive enzymatic mechanisms. *Communications biology*, 4(1):1–12, 2021.

[26] L Pasternak and Y Paz. Low-temperature direct bonding of silicon nitride to glass. *RSC Adv.*, 8(4):2161–2172, 2018.

[27] JJ Cras, CA Rowe-Taitt, DA Nivens, and FS Ligler. Comparison of chemical cleaning methods of glass in preparation for silanization. *Biosens. Bioelectron.*, 14(8-9):683–688, 1999.

[28] V Dugas and Y Chevalier. Surface hydroxylation and silane grafting on fumed and thermal silica. *J. Colloid Interf. Sci.*, 264(2):354–361, 2003.

[29] S Fiorilli, P Rivolo, E Descrovi, C Ricciardi, L Pasquardini, L Lunelli, L Vanzetti, C Pederzolli, B Onida, and E Garrone. Vapor-phase self-assembled monolayers of aminosilane on plasma-activated silicon substrates. *J. Colloid Interface Sci.*, 321(1):235–241, 2008.

[30] LT Zhuravlev. The surface chemistry of amorphous silica. Zhuravlev model. *Colloids Surf. A Physicochem. Eng.*, 173(1-3):1–38, 2000.

[31] HE Bergna and WO Roberts. *Colloidal silica: fundamentals and applications*, volume 131. CRC Press, 2005.

[32] PJ Yorke. Xxv. researches on silica. *Philos. Trans. R. Soc. Lond.*, (147):533–542, 1857.

[33] OW Flörke, HA Graetsch, F Brunk, L Benda, S Paschen, HE Bergna, WO Roberts, WA Welsh, C Libanati, M Ettlinger, et al. Silica. *Ullmann's Encycl. Ind. Chem.*, 2000.

[34] JE Shelby. *Introduction to glass science and technology*. Royal Society of Chemistry, 2020.

[35] CA Burkhard, EG Rochow, HS Booth, and J Hartt. The present state of organosilicon chemistry. *Chem. Rev.*, 41(1):97–149, 1947.

[36] S Pawlenko. *Organosilicon chemistry*. Walter de Gruyter, 2011.

[37] EG Rochow. Introduction to silicone chemistry. *Trans. Electrochem. Soc.*, 90(1):303, 1946.

[38] AJ O'Lenick, LLC Siltech, and G Dacula. Basic silicone chemistry–a review. *Silicone Spect.*, pages 1–23, 2009.

[39] SK Brown, MR Sim, MJ Abramson, and CN Gray. Concentrations of volatile organic compounds in indoor air–a review. *Indoor air*, 4(2):123–134, 1994.

[40] C Yang, G Wang, Z Lu, J Sun, J Zhuang, and W Yang. Effect of ultrasonic treatment on dispersibility of Fe_3O_4 nanoparticles and synthesis of multi-core Fe_3O_4/SiO_2 core/shell nanoparticles. *J. Mater. Chem.*, 15(39):4252–4257, 2005.

[41] N Sakai, R Wang, A Fujishima, T Watanabe, and K Hashimoto. Effect of ultrasonic treatment on highly hydrophilic TiO_2 surfaces. *Langmuir*, 14(20):5918–5920, 1998.

[42] A Henglein. Sonochemistry: historical developments and modern aspects. *Ultrasonics*, 25(1):6–16, 1987.

[43] FR Duke and TW Haas. The homogeneous base-catalyzed decomposition of hydrogen peroxide. *J. Phys. Chem.*, 65(2):304–306, 1961.

[44] RL Siegrist, M Crimi, and TJ Simpkin. *In situ chemical oxidation for groundwater remediation*, volume 3. Springer Science & Business Media, 2011.

[45] LM Fischer, M Tenje, AR Heiskanen, N Masuda, J Castillo, A Bentien, J Émneus, MH Jakobsen, and A Boisen. Gold cleaning methods for electrochemical detection applications. *Microelectron. Eng.*, 86(4-6):1282–1285, 2009.

[46] JG Croissant, Y Fatieiev, and NM Khashab. Degradability and clearance of silicon, organosilica, silsesquioxane, silica mixed oxide, and mesoporous silica nanoparticles. *Adv. Mater.*, 29(9):1604634, 2017.

[47] D Bossert, DA Urban, M Maceroni, L Ackermann-Hirschi, L Haeni, P Yajan, M Spuch-Calvar, B Rothen-Rutishauser, L Rodriguez-Lorenzo, A Petri-Fink, et al. A hydrofluoric acid-free method to dissolve and quantify silica nanoparticles in aqueous and solid matrices. *Sci. Rep.*, 9(1):1–12, 2019.

[48] PB Hauwiller. Environmentally friendly cleaning processes for metal surfaces. *Environm. Compl. Surf. Treatm. Mater. Aerospace Applic.*, 97(23480):1–31, 1997.

[49] MYA Mollah, R Schennach, J Patscheider, S Promreuk, and DL Cocke. Plasma chemistry as a tool for green chemistry, environmental analysis and waste management. *J. Hazard. Mater.*, 79(3):301–320, 2000.

[50] H Conrads and M Schmidt. Plasma generation and plasma sources. *Plasma Sources Sci. Technol.*, 9(4):441, 2000.

[51] P Krüger, R Knes, and J Friedrich. Surface cleaning by plasma-enhanced desorption of contaminants (PEDC). *Surf. Coat. Technol.*, 112(1-3):240–244, 1999.

[52] K Ono, N Nakazaki, H Tsuda, Y Takao, and K Eriguchi. Surface morphology evolution during plasma etching of silicon: Roughening, smoothing and ripple formation. *J. Phys. D: Appl. Phys.*, 50(41):414001, 2017.

[53] M Martin and G Cunge. Surface roughness generated by plasma etching processes of silicon. *J. Vac. Sci. Technol., B: Microelectron. Nanometer Struct.–Process., Meas., Phenom.*, 26(4):1281–1288, 2008.

[54] JD Le Grange, JL Markham, and CR Kurkjian. Effects of surface hydration on the deposition of silane monolayers on silica. *Langmuir*, 9(7):1749–1753, 1993.

[55] SP Zhdanov and AV Kiselev. The chemical structure of quartz and silica gel surfaces and their hydration. *Russ. J. Phys. Chem. A*, 31(10):2213–2223, 1957.

[56] FD Osterholtz and ER Pohl. Kinetics of the hydrolysis and condensation of organofunctional alkoxysilanes: a review. *J. Adhes. Sci. Technol*, 6(1):127–149, 1992.

[57] P van der Voort and EF Vansant. Silylation of the silica surface a review. *J. Liq. Chromatogr. Relat.*, 19(17-18):2723–2752, 1996.

[58] SV Slavov, AR Sanger, and KT Chuang. Mechanism of silation of silica with hexamethyldisilazane. *J. Phys. Chem. B*, 104(5):983–989, 2000.

[59] GL Witucki. A silane primer: chemistry and applications of alkoxy silanes. *J. Coat. Technol.*, 65:57–57, 1993.

[60] AP Kalra, BB Eakins, SD Patel, G Ciniero, V Rezania, K Shankar, and JA Tuszynski. All wired up: An exploration of the electrical properties of microtubules and tubulin. *ACS Nano*, 14(12):16301–16320, 2020.

[61] T Hawkins, M Mirigian, MS Yasar, and JL Ross. Mechanics of microtubules. *J. Biomech.*, 43(1):23–30, 2010.

[62] HP Erickson and ET O'Brien. Microtubule dynamic instability and GTP hydrolysis. *Annu. Rev. Biophys. Biomol. Struct.*, 21(1):145–166, 1992.

[63] PT Tran, RA Walker, and ED Salmon. A metastable intermediate state of microtubule dynamic instability that differs significantly between plus and minus ends. *J. Cell Biol.*, 138(1):105–117, 1997.

[64] T Mitchison and M Kirschner. Dynamic instability of microtubule growth. *Nature*, 312(5991):237–242, 1984.

[65] E-M Mandelkow, E Mandelkow, and RA Milligan. Microtubule dynamics and microtubule caps: a time-resolved cryo-electron microscopy study. *J. Cell Biol.*, 114(5):977–991, 1991.

[66] JB Olmsted and GG Borisy. Ionic and nucleotide requirements for microtubule polymerization in vitro. *Biochem.*, 14(13):2996–3005, 1975.

[67] SW Manka and CA Moores. The role of tubulin–tubulin lattice contacts in the mechanism of microtubule dynamic instability. *Nat. Struct. Mol. Biol.*, 25(7):607–615, 2018.

[68] AA Hyman, S Salser, DN Drechsel, N Unwin, and TJ Mitchison. Role of GTP hydrolysis in microtubule dynamics: information from a slowly hydrolyzable analogue, GMPCPP. *Mol. Biol. Cell*, 3(10):1155–1167, 1992.

[69] NK Pryer, RA Walker, VP Skeen, BD Bourns, MF Soboeiro, and ED Salmon. Brain microtubule-associated proteins modulate microtubule dynamic instability in vitro. real-time observations using video microscopy. *J. Cell Sci.*, 103(4):965–976, 1992.

[70] PB Schiff, J Fant, and SB Horwitz. Promotion of microtubule assembly in vitro by taxol. *Nature*, 277(5698):665–667, 1979.

[71] I Arnal and RH Wade. How does taxol stabilize microtubules? *Curr. Biol.*, 5(8):900–908, 1995.

[72] L Serrano, J De La Torre, RB Maccioni, and JS Avila. Involvement of the carboxyl-terminal domain of tubulin in the regulation of its assembly. *Proc. Natl. Acad. Sci. U.S.A*, 81(19):5989–5993, 1984.

[73] S Kotani, G Kawai, S Yokoyama, and H Murofushi. Interaction mechanism between microtubule-associated proteins and microtubules. a proton nuclear magnetic resonance analysis on the binding of synthetic peptide to tubulin. *Biochemistry*, 29(43):10049–10054, 1990.

[74] N Isozaki, S Ando, T Nakahara, H Shintaku, H Kotera, E Meyhöfer, and R Yokokawa. Control of microtubule trajectory within an electric field by altering surface charge density. *Sci. Rep.*, 5(1):1–8, 2015.

[75] N Isozaki, H Shintaku, H Kotera, TL Hawkins, JL Ross, and R Yokokawa. Control of molecular shuttles by designing electrical and mechanical properties of microtubules. *Sci. Robot.*, 2(10), 2017.

[76] NA Baker, D Sept, S Joseph, MJ Holst, and JA McCammon. Electrostatics of nanosystems: application to microtubules and the ribosome. *Proc. Natl. Acad. Sci. U.S.A*, 98(18):10037–10041, 2001.

[77] N Hirokawa, Y Noda, and Y Okada. Kinesin and dynein superfamily proteins in organelle transport and cell division. *Curr. Opin. Cell Biol.*, 10(1):60–73, 1998.

[78] N Hirokawa, Y Noda, Y Tanaka, and S Niwa. Kinesin superfamily motor proteins and intracellular transport. *Nat. Rev. Mol. Cell Biol.*, 10(10):682–696, 2009.

[79] DR Drummond. Regulation of microtubule dynamics by kinesins. In *Seminars in cell & developmental biology*, volume 22, pages 927–934. Elsevier, 2011.

[80] DD Hackney. Evidence for alternating head catalysis by kinesin during microtubule-stimulated ATP hydrolysis. *Proc. Natl. Acad. Sci. U.S.A*, 91(15):6865–6869, 1994.

[81] SP Gilbert, MR Webb, M Brune, and KA Johnson. Pathway of processive ATP hydrolysis by kinesin. *Nature*, 373(6516):671–676, 1995.

[82] W Hua, EC Young, ML Fleming, and J Gelles. Coupling of kinesin steps to ATP hydrolysis. *Nature*, 388(6640):390–393, 1997.

[83] H Miki, Y Okada, and N Hirokawa. Analysis of the kinesin superfamily: insights into structure and function. *Trends Cell Biol.*, 15(9):467–476, 2005.

[84] DC Turner, C Chang, K Fang, SL Brandow, and DB Murphy. Selective adhesion of functional microtubules to patterned silane surfaces. *Biophys. J.*, 69(6):2782–2789, 1995.

[85] TB Brown and WO Hancock. A polarized microtubule array for kinesin-powered nanoscale assembly and force generation. *Nano Lett.*, 2(10):1131–1135, 2002.

[86] MC Tarhan, D Collard, C Bottier, R Yokokawa, M Hosogi, G Hashiguchi, and H Fujita. Isolation and manipulation of single microtubule by silicon microtweezers. In *Proc. of μTAS*, pages 862–864, 2008.

[87] WH Liang, Q Li, KMR Faysal, SJ King, A Gopinathan, and J Xu. Microtubule defects influence kinesin-based transport in vitro. *Biophys. J.*, 110(10):2229–2240, 2016.

[88] ME Wiseman and CW Frank. Antibody adsorption and orientation on hydrophobic surfaces. *Langmuir*, 28(3):1765–1774, 2012.

[89] L-C Xu and CA Siedlecki. Effects of surface wettability and contact time on protein adhesion to biomaterial surfaces. *Biomaterials*, 28(22):3273–3283, 2007.

[90] RG Couston, MW Skoda, S Uddin, and CF van der Walle. Adsorption behavior of a human monoclonal antibody at hydrophilic and hydrophobic surfaces. In *MAbs*, volume 5, pages 126–139. Taylor & Francis, 2013.

[91] L-J Cheng, M-T Kao, E Meyhöfer, and LJ Guo. Highly efficient guiding of microtubule transport with imprinted CYTOP nanotracks. *Small*, 1(4):409–414, 2005.

[92] MN Fernandez, DM Beltramo, AC Alonso, and HS Barra. Conversion of hydrophilic tubulin into a hydrophobic compound. evidence for the involvement of membrane proteins. *Mol. Cell. Biochem.*, 170(1):1–8, 1997.

[93] C Gell, V Bormuth, GJ Brouhard, DN Cohen, S Diez, CT Friel, J Helenius, B Nitzsche, H Petzold, J Ribbe, et al. Microtubule dynamics reconstituted in vitro and imaged by single-molecule fluorescence microscopy. *Meth. Cell Biol.*, 95:221–245, 2010.

[94] KN Fish. Total internal reflection fluorescence (TIRF) microscopy. *Curr. Protoc. Cytom*, 50(1):12–18, 2009.

[95] ML Martin-Fernandez, CJ Tynan, and SED Webb. A 'pocket guide' to total internal reflection fluorescence. *J. Microsc.*, 252(1):16–22, 2013.

[96] Medishop. *https://www.lms-lab.de/en-gb/brand-haemacytom.cover-glass-f.count.chamb.ivd-24x24x0-4-mm-723014*, (2022-01-14, 14:00).

[97] DR Lide. *CRC handbook of chemistry and physics*, volume 85. CRC press, 2004.

[98] J Vörös. The density and refractive index of adsorbing protein layers. *Biophys. J.*, 87(1):553–561, 2004.

[99] VA Barr and SC Bunnell. Interference reflection microscopy. *Curr. Protoc. Cell Biol.*, 45(1):4–23, 2009.

[100] L Limozin and K Sengupta. Quantitative reflection interference contrast microscopy (RICM) in soft matter and cell adhesion. *Chem. Phys. Chem.*, 10(16):2752–2768, 2009.

[101] S Simmert, MK Abdosamadi, G Hermsdorf, and E Schäffer. LED-based interference-reflection microscopy combined with optical tweezers for quantitative three-dimensional microtubule imaging. *Opt. Express*, 26(11):14499–14513, 2018.

[102] M Mahamdeh and J Howard. Implementation of interference reflection microscopy for label-free, high-speed imaging of microtubules. *J. Vis.*, (150):e59520, 2019.

[103] FA Stevie and CL Donley. Introduction to x-ray photoelectron spectroscopy. *J. Vac. Sci. Technol. A: Vac. Surf. Films*, 38(6):063204, 2020.

[104] M Mahamdeh and E Schäffer. Optical tweezers with millikelvin precision of temperature-controlled objectives and base-pair resolution. *Opt. Express*, 17(19):17190, 2009.

[105] TJ Fellers and MW Davidson. Microscopy basics: coverslip correction. *https://www.microscopyu.com/microscopy-basics/coverslip-correction*, (27.2.2021, 08:40).

[106] Medishop. *https://www.medishop.de/sitemap/Deckglaeser-18-x-18-100-Stck.html*, (2020-11-27, 12:00).

[107] The geyer shop. *https://shop.thgeyer-lab.com/erp/catalog/search/search.action;jsessionid=D08B0D8DAC9E7A5D3F5FDCCAAEF14795?model.query=MENZEL*, (2020-11-27, 12:00).

[108] AR Heiskanen, CF Spégel, N Kostesha, T Ruzgas, and J Emnéus. Monitoring of saccharomyces cerevisiae cell proliferation on thiol-modified planar gold microelectrodes using impedance spectroscopy. *Langmuir*, 24(16):9066–9073, 2008.

[109] Ronny Löffler. Instrument scientist at LISA+ facility, University of Tübingen, 2018.

[110] A Kawai and J Kawakami. Characterization of SiO_2 surface treated by HMDS vapor and O_2 plasma with AFM tip. *J. Photopolym. Sci. Technol.*, 16(5):665–668, 2003.

[111] DM Walba, CA Liberko, E Korblova, M Farrow, TE Furtak, BC Chow, DK Schwartz, AS Freeman, K Douglas, SD Williams, et al. Self-assembled monolayers for liquid crystal alignment: simple preparation on glass using alkyltrialkoxysilanes. *Liq. Cryst.*, 31(4):481–489, 2004.

[112] KH Choi, JP Bourgoin, S Auvray, D Esteve, GS Duesberg, S Roth, and M Burghard. Controlled deposition of carbon nanotubes on a patterned substrate. *Surf. Sci.*, 462(1-3):195–202, 2000.

[113] M Chugh, M Reißner, M Bugiel, E Lipka, A Herrmann, B Roy, S Müller, and E Schäffer. Phragmoplast orienting kinesin-2 is a weak motor switching between processive and diffusive modes. *Biophys. J.*, 115(2):375–385, 2018.

[114] ABD Cassie. Contact angles. *Discuss. Faraday Soc.*, 3:11–16, 1948.

[115] MR Nejadnik, ALJ Olsson, PK Sharma, HC van der Mei, W Norde, and HJ Busscher. Adsorption of pluronic F-127 on surfaces with different hydrophobicities probed by quartz crystal microbalance with dissipation. *Langmuir*, 25(11):6245–6249, 2009.

[116] JJ Yeh and I Lindau. Atomic subshell photoionization cross sections and asymmetry parameters: 1 z 103. *At. Data Nucl. Data Tables*, 32(1):1–155, 1985.

[117] I Zgura, R Moldovan, CC Negrila, S Frunza, VF Cotorobai, L Frunza, et al. Surface free energy of smooth and dehydroxylated fused quartz from contact angle measurements using some particular organics as probe liquids. *J. Optoelectron. Adv. Mater*, 15:627–634, 2013.

[118] LD Eske and DW Galipeau. Characterization of SiO_2 surface treatments using AFM, contact angles and a novel dewpoint technique. *Colloids Surf. A Physicochem. Eng.*, 154(1-2):33–51, 1999.

[119] AU Alam, MMR Howlader, and MJ Deen. The effects of oxygen plasma and humidity on surface roughness, water contact angle and hardness of silicon, silicon dioxide and glass. *J. Micromech. Microeng.*, 24(3):035010, 2014.

[120] K Terpilowski and D Rymuszka. Surface properties of glass plates activated by air, oxygen, nitrogen and argon plasma. *Glass Phys. Chem.*, 42(6):535–541, 2016.

[121] V Wedler, F Strauß, S Sudhakar, GL Hermsdorf, Y-D Stierhof, and E Schäffer. Polycationic gold nanorods as multipurpose in vitro microtubule markers. *Nanoscale Adv.*, 2(9):4003–4010, 2020.

[122] AV Krasnoslobodtsev and SN Smirnov. Effect of water on silanization of silica by trimethoxysilanes. *Langmuir*, 18(8):3181–3184, 2002.

[123] WJ Herzberg, JE Marian, and T Vermeulen. The receding contact angle. *J. Colloid Interface Sci.*, 33(1):164–171, 1970.

[124] ML Hair and W Hertl. Reactions of chlorosilanes with silica surfaces. *J. Phys. Chem.*, 73(7):2372–2378, 1969.

[125] ML Hair and W Hertl. Reaction of hexamethyldisilazane with silica. *J. Phys. Chem.*, 75(14):2181–2185, 1971.

[126] W Petasch, B Kegel, H Schmid, K Lendenmann, and HU Keller. Low-pressure plasma cleaning: a process for precision cleaning applications. *Surf. Coat. Technol.*, 97(1-3):176–181, 1997.

[127] S Ahmed, A Aitani, F Rahman, A Al-Dawood, and F Al-Muhaish. Decomposition of hydrocarbons to hydrogen and carbon. *Appl. Catal. A: Gen.*, 359(1-2):1–24, 2009.

[128] D Sprenger, H Bach, W Meisel, and P Gütlich. XPS study of leached glass surfaces. *J. Non-Cryst. Solids*, 126(1-2):111–129, 1990.

[129] E Metwalli, D Haines, O Becker, S Conzone, and Carlo G Pantano. Surface characterizations of mono-, di-, and tri-aminosilane treated glass substrates. *J. Colloid Interface Sci.*, 298(2):825–831, 2006.

[130] M Schlosser and D Michel. About the "physiological size" of fluorine substituents: comparison of sensorially active compounds with fluorine and methyl substituted analogues. *Tetrahedron*, 52(1):99–108, 1996.

[131] DL Coy, M Wagenbach, and J Howard. Kinesin takes one 8-nm step for each ATP that it hydrolyzes. *J. Biol. Chem.*, 274(6):3667–3671, 1999.

[132] LJ Harris, E Skaletsky, and A McPherson. Crystallographic structure of an intact IgG1 monoclonal antibody. *J. Mol. Biol.*, 275(5):861–872, 1998.

[133] AC Greene, M Bachand, A Gomez, MJ Stevens, and GD Bachand. Interactions regulating the head-to-tail directed assembly of biological janus rods. *Chem. Commun.*, 53(32):4493–4496, 2017.

[134] JN Israelachvili. *Intermolecular and surface forces*. Academic press, 2015.

[135] Y Gu and D Li. The ζ-potential of glass surface in contact with aqueous solutions. *J. Colloid Interf. Sci.*, 226(2):328–339, 2000.

[136] SH Behrens and DG Grier. The charge of glass and silica surfaces. *J. Chem. Phys.*, 115(14):6716–6721, 2001.

[137] T Kim, M-T Kao, EF Hasselbrink, and E Meyhöfer. Nanomechanical model of microtubule translocation in the presence of electric fields. *Biophys. J.*, 94(10):3880–3892, 2008.

[138] A Ciorîtă, M Bugiel, S Sudhakar, E Schäffer, and A Jannasch. Single depolymerizing and transport kinesins stabilize microtubule ends. *Cytoskeleton*, 78(5):177–184, 2021.

[139] Y-W Kuo and J Howard. In vitro reconstitution of microtubule dynamics and severing imaged by label-free interference reflection microscopy. *arXiv preprint arXiv:2107.01501*, 2021.

[140] G Cappello, M Badoual, A Ott, J Prost, and L Busoni. Kinesin motion in the absence of external forces characterized by interference total internal reflection microscopy. *Phys. Rev. E*, 68(2):021907, 2003.

[141] T Korten, B Nitzsche, C Gell, F Ruhnow, C Leduc, and S Diez. Fluorescence imaging of single kinesin motors on immobilized microtubules. In *Single Molecule Analysis*, pages 121–137. Springer, 2011.

[142] K Lindfors, T Kalkbrenner, P Stoller, and V Sandoghdar. Detection and spectroscopy of gold nanoparticles using supercontinuum white light confocal microscopy. *Phys. Rev. Lett.*, 93(3):037401, 2004.

[143] RW Taylor and V Sandoghdar. Interferometric scattering (iscat) microscopy and related techniques. In *Label-Free Super-Resolution Microscopy*, pages 25–65. Springer, 2019.

[144] G Young, N Hundt, D Cole, A Fineberg, J Andrecka, A Tyler, A Olerinyova, A Ansari, EG Marklund, MP Collier, et al. Quantitative mass imaging of single biological macromolecules. *Science*, 360(6387):423–427, 2018.

[145] PE Rischitor, S Konzack, and R Fischer. The Kip3-like kinesin KipB moves along microtubules and determines spindle position during synchronized mitoses in aspergillus nidulans hyphae. *Eukaryot. Cell*, 3(3):632–645, 2004.

[146] CV Sindelar and D Liu. Tracking down kinesin's achilles heel with balls of gold. *Biophys. J.*, 112(12):2454, 2017.

[147] J Ortega-Arroyo and P Kukura. Interferometric scattering microscopy (iSCAT): new frontiers in ultrafast and ultrasensitive optical microscopy. *Phys. Chem. Chem. Phys.*, 14(45):15625–15636, 2012.

[148] D Cole, G Young, A Weigel, A Sebesta, and P Kukura. Label-free single-molecule imaging with numerical-aperture-shaped interferometric scattering microscopy. *ACS Photonics*, 4(2):211–216, 2017.

[149] Tom Stumpp. Optimized interference reflection microscopy for high-contrast imaging of microtubules. Master's thesis, Zentrum für Molekularbiologie der Pflanzen, Universtät Tübingen, Auf der Morgenstelle 32, Deutschland, 2021.

[150] Aylin Kayacik. Optimized LED-based interference reflection microscopy for microtubule imaging. Master's thesis, Zentrum für Molekularbiologie der Pflanzen, Universtät Tübingen, Auf der Morgenstelle 32, Deutschland, 2019.

[151] Sandro Münch. Single molecule detection using interferometric scattering microscopy. Master's thesis, Zentrum für Molekularbiologie der Pflanzen, Universtät Tübingen, Auf der Morgenstelle 32, Deutschland, 2022.

[152] GL Hermsdorf, SA Szilagyi, S Rösch, and E Schäffer. High performance passive vibration isolation system for optical tables using six-degree-of-freedom viscous damping combined with steel springs. *Rev. Sci. Instrum.*, 90(1):015113, 2019.

[153] A Shinohara, M Shinohara, T Ohta, S Matsuda, and T Ogawa. Rad52 forms ring structures and co-operates with RPA in single-strand DNA annealing. *Genes Cells*, 3(3):145–156, 1998.

[154] W Kagawa, H Kurumizaka, R Ishitani, S Fukai, O Nureki, T Shibata, and S Yokoyama. Crystal structure of the homologous-pairing domain from the human Rad52 recombinase in the undecameric form. *Mol. Cell*, 10(2):359–371, 2002.

[155] A. Sperling, GP Rivera, F Zhang, M Zanella, and WJ Parak. Biological applications of gold nanoparticles. *Chem. Soc. Rev.*, 37(9):1896–1908, 2008.

[156] H Chen, L Shao, Q Li, and J Wang. Gold nanorods and their plasmonic properties. *Chem. Soc. Rev.*, 42:2679–2724, 2013.

[157] MB Mohamed, V Volkov, S Link, and MA El-Sayed. The 'lightning' gold nanorods: fluorescence enhancement of over a million compared to the gold metal. *Chem. Phys. Lett.*, 317(6):517–523, 2000.

[158] S Khatua, PMR Paulo, H Yuan, A Gupta, P Zijlstra, and M Orrit. Resonant plasmonic enhancement of single-molecule fluorescence by individual gold nanorods. *ACS Nano*, 8(5):4440–4449, 2014.

[159] P Zijlstra, PMR Paulo, and M Orrit. Optical detection of single non-absorbing molecules using the surface plasmon resonance of a gold nanorod. *Nat. Nanotechnol.*, 7(6):379–382, 2012.

[160] MD Baaske and F Vollmer. Optical observation of single atomic ions interacting with plasmonic nanorods in aqueous solution. *Nat. Photonics*, 10(11):733, 2016.

[161] S Rosenblum, Y Lovsky, L Arazi, F Vollmer, and B Dayan. Cavity ring-up spectroscopy for ultrafast sensing with optical microresonators. *Nat. Commun.*, 6(1):6788, 2015.

[162] JR Heath. Size-dependent surface-plasmon resonances of bare silver particles. *Phys. Rev. B*, 40(14):9982, 1989.

[163] S Link and MA El-Sayed. Spectral properties and relaxation dynamics of surface plasmon electronic oscillations in gold and silver nanodots and nanorods. *J. Phys. Chem. B*, 103(40):8410–8426, 1999.

[164] C Sönnichsen and AP Alivisatos. Gold nanorods as novel nonbleaching plasmon-based orientation sensors for polarized single-particle microscopy. *Nano Lett.*, 5(2):301–304, 2005.

[165] KE Sawin and JM Scholey. Motor proteins in cell division. *Trends Cell Biol.*, 1(5):122–129, 1991.

[166] RD Vale and RA Milligan. The way things move: looking under the hood of molecular motor proteins. *Science*, 288(5463):88–95, 2000.

[167] A Ramaiya, B Roy, M Bugiel, and E Schäffer. Kinesin rotates unidirectionally and generates torque while walking on microtubules. *Proc. Natl. Acad. Sci.*, 114(41):10894–10899, 2017.

[168] S Sudhakar, MK Abdosamadi, TJ Jachowski, M Bugiel, A Jannasch, and E Schäffer. Germanium nanospheres for ultraresolution picotensiometry of kinesin motors. *Science*, 371(6530), 2021.

[169] V Jacobsen, P Stoller, C Brunner, V Vogel, and V Sandoghdar. Interferometric optical detection and tracking of very small gold nanoparticles at a water-glass interface. *Opt. Express*, 14(1):405–414, Jan 2006.

[170] G Wang, W Sun, Y Luo, and N Fang. Resolving rotational motions of nano-objects in engineered environments and live cells with gold nanorods and differential interference contrast microscopy. *J. Am. Chem. Soc.*, 132(46):16417–16422, 2010.

[171] J Won Ha, W Sun, G Wang, and N Fang. Differential interference contrast polarization anisotropy for tracking rotational dynamics of gold nanorods. *Chem. Commun.*, 47:7743–7745, 2011.

[172] A Jannasch, V Bormuth, M Storch, J Howard, and E Schäffer. Kinesin-8 is a low-force motor protein with a weakly bound slip state. *Biophys. J.*, 104(11):2456–2464, 2013.

[173] KJ Mickolajczyk, NC Deffenbaugh, J Ortega Arroyo, J Andrecka, P Kukura, and WO Hancock. Kinetics of nucleotide-dependent structural transitions in the kinesin-1 hydrolysis cycle. *Proc. Natl. Acad. Sci. U. S. A.*, 112(52):E7186–E7193, 2015.

[174] H Isojima, R Iino, Y Niitani, H Noji, and M Tomishige. Direct observation of intermediate states during the stepping motion of kinesin-1. *Nat. Chem. Biol.*, 12(4):290–297, 2016.

[175] M Mahamdeh, S Simmert, A Luchniak, E Schäffer, and J Howard. Label-free high-speed wide-field imaging of single microtubules using interference reflection microscopy. *J. Microsc.*, 272(1):60–66, 2018.

[176] S Behrens, W Habicht, J Wu, and E Unger. Tubulin assemblies as biomolecular templates for nanostructure synthesis: from nanoparticle arrays to nanowires. *Surf. Interface Anal.*, 38(6):1014–1018, 2006.

[177] JC Zhou, Y Gao, AA Martinez-Molares, X Jing, D Yan, J Lau, T Hamasaki, CS Ozkan, M Ozkan, E Hu, et al. Microtubule-based gold nanowires and nanowire arrays. *Small*, 4(9):1507–1515, 2008.

[178] JC Zhou, X Wang, M Xue, Z Xu, T Hamasaki, Y Yang, K Wang, and B Dunn. Characterization of gold nanoparticle binding to microtubule filaments. *Mater. Sci. Eng. C*, 30(1):20–26, 2010.

[179] C Rosano, P Arosio, and M Bolognesi. The x-ray three-dimensional structure of avidin. *Biomol. Eng.*, 16(1-4):5–12, 1999.

[180] M Reth. Matching cellular dimensions with molecular sizes. *Nat. Immunol.*, 14(8):765, 2013.

[181] M N'Gom, S Li, G Schatz, R Erni, A Agarwal, N Kotov, and TB Norris. Electron-beam mapping of plasmon resonances in electromagnetically interacting gold nanorods. *Phys. Rev. B*, 80(11):113411, 2009.

[182] X Wang, Y Li, H Wang, Q Fu, J Peng, Y Wang, J Du, Y Zhou, and L Zhan. Gold nanorod-based localized surface plasmon resonance biosensor for sensitive detection of hepatitis B virus in buffer, blood serum and plasma. *Biosens. Bioelectron.*, 26(2):404–410, 2010.

[183] MD Baaske, MR Foreman, and F Vollmer. Single-molecule nucleic acid interactions monitored on a label-free microcavity biosensor platform. *Nat. Nanotechnol.*, 9(11):933–939, 2014.

[184] J Gigault, TJ Cho, RI MacCuspie, and VA Hackley. Gold nanorod separation and characterization by asymmetric-flow field flow fractionation with UV-Vis detection. *Anal. Bioanal. Chem.*, 405(4):1191–1202, 2013.

[185] R Cortesi, E Esposito, E Menegatti, R Gambari, and C Nastruzzi. Effect of cationic liposome composition on in vitro cytotoxicity and protective effect on carried DNA. *Int. J. Pharm.*, 139(1-2):69–78, 1996.

[186] H Takahashi, Y Niidome, T Niidome, K Kaneko, H Kawasaki, and S Yamada. Modification of gold nanorods using phosphatidylcholine to reduce cytotoxicity. *Langmuir*, 22(1):2–5, 2006.

[187] S Lee, LJE Anderson, CM Payne, and JH Hafner. Structural transition in the surfactant layer that surrounds gold nanorods as observed by analytical surface-enhanced Raman spectroscopy. *Langmuir*, 27(24):14748–14756, 2011.

[188] Y Okada and N Hirokawa. Mechanism of the single-headed processivity: diffusional anchoring between the K-loop of kinesin and the C terminus of tubulin. *Proc. Natl. Acad. Sci.*, 97(2):640–645, 2000.

[189] L Vigderman, P Manna, and ER Zubarev. Quantitative replacement of cetyl trimethylammonium bromide by cationic thiol ligands on the surface of gold nanorods and their extremely large uptake by cancer cells. *Angew. Chem. Int. Ed.*, 51(3):636–641, 2012.

[190] ML Brongersma and PG Kik. *Surface plasmon nanophotonics*, volume 131. Springer, 2007.

[191] KA Willets and RP Van Duyne. Localized surface plasmon resonance spectroscopy and sensing. *Annu. Rev. Phys. Chem.*, 58:267–297, 2007.

[192] J Yguerabide and EE Yguerabide. Light-scattering submicroscopic particles as highly fluorescent analogs and their use as tracer labels in clinical and biological applications: Ii. experimental characterization. *Anal. Biochem.*, 262(2):157–176, 1998.

[193] S Link and MA El-Sayed. Shape and size dependence of radiative, non-radiative and photothermal properties of gold nanocrystals. *Int. Rev. Phys. Chem.*, 19(3):409–453, 2000.

[194] T Neuman, C Huck, J Vogt, F Neubrech, R Hillenbrand, J Aizpurua, and A Pucci. Importance of plasmonic scattering for an optimal enhancement of vibrational absorption in SEIRA with linear metallic antennas. *J. Phys. Chem. C*, 119(47):26652–26662, 2015.

[195] K Aslan, JR Lakowicz, and CD Geddes. Plasmon light scattering in biology and medicine: new sensing approaches, visions and perspectives. *Curr. Opin. Chem. Biol.*, 9(5):538–544, 2005.

[196] K Park, S Biswas, S Kanel, D Nepal, and RA Vaia. Engineering the optical properties of gold nanorods: independent tuning of surface plasmon energy, extinction coefficient, and scattering cross section. *J. Phys. Chem. C*, 118(11):5918–5926, 2014.

[197] G Mie. Beiträge zur Optik trüber Medien, speziell kolloidaler Metallösungen. *Ann. Phys.*, 330(3):377–445, 1908.

[198] LS Jung, CT Campbell, TM Chinowsky, MN Mar, and SS Yee. Quantitative interpretation of the response of surface plasmon resonance sensors to adsorbed films. *Langmuir*, 14(19):5636–5648, 1998.

[199] E Dulkeith, T Niedereichholz, TA Klar, J Feldmann, G Von Plessen, DI Gittins, KS Mayya, and F Caruso. Plasmon emission in photoexcited gold nanoparticles. *Phys. Rev. B*, 70(20):205424, 2004.

[200] Y Fang, W-S Chang, B Willingham, P Swanglap, S Dominguez-Medina, and S Link. Plasmon emission quantum yield of single gold nanorods as a function of aspect ratio. *ACS Nano*, 6(8):7177–7184, 2012.

[201] A Mooradian. Photoluminescence of metals. *Phys. Rev. Lett.*, 22(5):185, 1969.

[202] K Imura, T Nagahara, and H Okamoto. Plasmon mode imaging of single gold nanorods. *J. Am. Chem. Soc.*, 126(40):12730–12731, 2004.

[203] OP Varnavski, MB Mohamed, MA El-Sayed, and T Goodson. Relative enhancement of ultrafast emission in gold nanorods. *J. Phys. Chem. B*, 107(14):3101–3104, 2003.

[204] RA Farrer, FL Butterfield, VW Chen, and JT Fourkas. Highly efficient multiphoton-absorption-induced luminescence from gold nanoparticles. *Nano Lett.*, 5(6):1139–1142, 2005.

[205] MR Beversluis, A Bouhelier, and L Novotny. Continuum generation from single gold nanostructures through near-field mediated intraband transitions. *Phys. Rev. B*, 68(11):115433, 2003.

[206] A Bouhelier, R Bachelot, G Lerondel, S Kostcheev, P Royer, and GP Wiederrecht. Surface plasmon characteristics of tunable photoluminescence in single gold nanorods. *Phys. Rev. Lett.*, 95(26):267405, 2005.

[207] A Gaiduk, M Yorulmaz, and M Orrit. Correlated absorption and photoluminescence of single gold nanoparticles. *Chem. Phys. Chem.*, 12(8):1536–1541, 2011.

[208] P Nordlander, C Oubre, E Prodan, K Li, and MI Stockman. Plasmon hybridization in nanoparticle dimers. *Nano Lett.*, 4(5):899–903, 2004.

[209] PK Jain and MA El-Sayed. Plasmonic coupling in noble metal nanostructures. *Chem. Phys. Lett.*, 487(4-6):153–164, 2010.

[210] T-S Deng, J Parker, Y Yifat, N Shepherd, and NF Scherer. Dark plasmon modes in symmetric gold nanoparticle dimers illuminated by focused cylindrical vector beams. *J. Phys. Chem. C*, 122(48):27662–27672, 2018.

[211] F Tam, GP Goodrich, BR Johnson, and NJ Halas. Plasmonic enhancement of molecular fluorescence. *Nano Lett.*, 7(2):496–501, 2007.

[212] G Schneider, G Decher, N Nerambourg, R Praho, MHV Werts, and M Blanchard-Desce. Distance-dependent fluorescence quenching on gold nanoparticles ensheathed with layer-by-layer assembled polyelectrolytes. *Nano Lett.*, 6(3):530–536, 2006.

[213] KA Kang, J Wang, JB Jasinski, and S Achilefu. Fluorescence manipulation by gold nanoparticles: from complete quenching to extensive enhancement. *J. Nanobiotechnology*, 9(1):1–13, 2011.

[214] S Neretina, W Qian, EC Dreaden, MA El-Sayed, RA Hughes, JS Preston, and P Mascher. Exciton lifetime tuning by changing the plasmon field orientation with

respect to the exciton transition moment direction: CdTe-Au core-shell nanorods. *Nano Lett.*, 9(3):1242–1248, 2009.

[215] T Ming, L Zhao, H Chen, KC Woo, J Wang, and H-Q Lin. Experimental evidence of plasmophores: plasmon-directed polarized emission from gold nanorod–fluorophore hybrid nanostructures. *Nano Lett.*, 11(6):2296–2303, 2011.

[216] GR Bourret, T Ozel, M Blaber, CM Shade, GC Schatz, and CA Mirkin. Long-range plasmophore rulers. *Nano Lett.*, 13(5):2270–2275, 2013.

[217] A Hakonen and N Strömberg. Plasmonic nanoparticle interactions for high-performance imaging fluorosensors. *Chem. Commun.*, 47(12):3433–3435, 2011.

[218] A Hakonen. Fluorescence ratiometric properties induced by nanoparticle plasmonics and nanoscale dye dynamics. *Sci. World J.*, 2013, 2013.

[219] CS Yun, A Javier, T Jennings, M Fisher, S Hira, S Peterson, B Hopkins, NO Reich, and GF Strouse. Nanometal surface energy transfer in optical rulers, breaking the FRET barrier. *J. Am. Chem. Soc.*, 127(9):3115–3119, 2005.

[220] E Dulkeith, M Ringler, TA Klar, J Feldmann, A Munoz Javier, and WJ Parak. Gold nanoparticles quench fluorescence by phase induced radiative rate suppression. *Nano Lett.*, 5(4):585–589, 2005.

[221] JR Lakowicz, K Ray, M Chowdhury, H Szmacinski, Y Fu, J Zhang, and K Nowaczyk. Plasmon-controlled fluorescence: a new paradigm in fluorescence spectroscopy. *Analyst*, 133(10):1308–1346, 2008.

[222] CJ Murphy, LB Thompson, DJ Chernak, JA Yang, ST Sivapalan, SP Boulos, J Huang, AM Alkilany, and PN Sisco. Gold nanorod crystal growth: From seed-mediated synthesis to nanoscale sculpting. *Curr. Opin. Colloid Interface Sci.*, 16(2):128–134, 2011.

[223] AV Ermushev, BV Mchedlishvili, and Oleĭ. Surface enhancement of local optical fields and the lightning-rod effect.

[224] J Pérez-Juste, I Pastoriza-Santos, LM Liz-Marzán, and P Mulvaney. Gold nanorods: synthesis, characterization and applications. *Coord. Chem. Rev.*, 249(17-18):1870–1901, 2005.

[225] Lord Rayleigh. Cxii. the problem of the whispering gallery. *The London, Edinburgh, and Dublin Philosophical Magazine and Journal of Science*, 20(120):1001–1004, 1910.

[226] DL Creedon, Y Reshitnyk, W Farr, JM Martinis, TL Duty, and ME Tobar. High Q-factor sapphire whispering gallery mode microwave resonator at single photon energies and millikelvin temperatures. *Appl. Phys. Lett.*, 98(22):222903, 2011.

[227] LK Ausman and GC Schatz. Whispering-gallery mode resonators: Surface enhanced Raman scattering without plasmons. *J. Chem. Phys.*, 129(5):054704, 2008.

[228] MR Foreman, JD Swaim, and F Vollmer. Whispering gallery mode sensors. *Adv. Opt. Photonics*, 7(2):168–240, 2015.

[229] F Vollmer and S Arnold. Whispering-gallery-mode biosensing: label-free detection down to single molecules. *Nature methods*, 5(7):591–596, 2008.

[230] B Nikoobakht and MA El-Sayed. Preparation and growth mechanism of gold nanorods (NRs) using seed-mediated growth method. *Chem. Mater.*, 15(10):1957–1962, 2003.

[231] L Reimer. *Transmission electron microscopy: physics of image formation and microanalysis*, volume 36. Springer, 2013.

[232] Jeol. *https://www.jeolusa.com/NEWS-EVENTS/Press-Releases/jeol-demonstrates-new-jem-1400plus-120kv-transmission-electron-microscope-for-high-contrast-cryotem-and-stem-applications*, (2022-04-01, 10:00).

[233] AB Maunsbach and BA Afzelius. *Biomedical electron microscopy: Illustrated methods and interpretations*. Elsevier, 1998.

[234] RC Burghardt and R Droleskey. Transmission electron microscopy. *Current Protoc. Microbiol.*, 3(1):2B–1, 2006.

[235] M Bugiel, E Böhl, and E Schäffer. The kinesin-8 Kip3 switches protofilaments in a sideward random walk asymmetrically biased by force. *Biophys. J.*, 108(8):2019–2027, 2015.

[236] J Schindelin, I Arganda-Carreras, E Frise, V Kaynig, M Longair, T Pietzsch, S Preibisch, C Rueden, S Saalfeld, B Schmid, J-Y Tinevez, DJ White, V Hartenstein, K Eliceiri, P Tomancak, and A Cardona. Fiji: an open-source platform for biological-image analysis. *Nat. Methods*, 9(7):676–82, 2012.

[237] N Eerqing, S Subramanian, J Rubio, T Lutz, H-Y Wu, J Anders, C Soeller, and F Vollmer. Comparing transient oligonucleotide hybridization kinetics using DNA-PAINT and optoplasmonic single-molecule sensing on gold nanorods. *ACS Photonics*, 8(10):2882–2888, 2021.

[238] P Jun and Z HU. Simulation of CTAB bilayer adsorbed on Au (100), Au (110), and Au (111) surfaces: structure stability and dynamic properties. *J. Univ. Chin. Acad. Sci.*, 2017.

[239] F Barbero, OH Moriones, NG Bastús, and V Puntes. Dynamic equilibrium in the cetyltrimethylammonium bromide–Au nanoparticle bilayer, and the consequent impact on the formation of the nanoparticle protein corona. *Bioconjug. Chem.*, 30(11):2917–2930, 2019.

[240] R Becker, B Liedberg, and P-O Käll. CTAB promoted synthesis of Au nanorods–temperature effects and stability considerations. *J. Colloid Interface Sci.*, 343(1):25–30, 2010.

[241] J Casas, M Venkataramasubramani, Y Wang, and L Tang. Replacement of cetyltrimethylammoniumbromide bilayer on gold nanorod by alkanethiol crosslinker for enhanced plasmon resonance sensitivity. *Biosens. Bioelectron.*, 49:525–530, 2013.

[242] O Krivosudskỳ, P Dráber, and M Cifra. Resolving controversy of unusually high refractive index of a tubulin. *Europhys. Lett.*, 117(3):38003, 2017.

[243] JR Guzman-Sepulveda, R Wu, AP Kalra, M Aminpour, JA Tuszynski, and A Dogariu. Tubulin polarizability in aqueous suspensions. *ACS omega*, 4(5):9144–9149, 2019.

[244] ME Kandel, KW Teng, PR Selvin, and G Popescu. Label-free imaging of single microtubule dynamics using spatial light interference microscopy. *ACS Nano*, 11(1):647–655, 2017.

[245] G Lu, L Hou, T Zhang, W Li, J Liu, P Perriat, and Q Gong. Anisotropic plasmonic sensing of individual or coupled gold nanorods. *J. Phys. Chem. C*, 115(46):22877–22885, 2011.

[246] GJ Nusz, AC Curry, SM Marinakos, A Wax, and A Chilkoti. Rational selection of gold nanorod geometry for label-free plasmonic biosensors. *ACS nano*, 3(4):795–806, 2009.

[247] H Chen, X Kou, Z Yang, W Ni, and J Wang. Shape-and size-dependent refractive index sensitivity of gold nanoparticles. *Langmuir*, 24(10):5233–5237, 2008.

[248] H Chen, L Shao, KC Woo, T Ming, H-Q Lin, and J Wang. Shape-dependent refractive index sensitivities of gold nanocrystals with the same plasmon resonance wavelength. *J. Phys. Chem. C*, 113(41):17691–17697, 2009.

[249] US Raikar, VB Tangod, BM Mastiholi, and VJ Fulari. Fluorescence quenching using plasmonic gold nanoparticles. *Opt. Commun.*, 284(19):4761–4765, 2011.

[250] Z Ma, DN LeBard, SM Loverde, KA Sharp, ML Klein, DE Discher, and TH Finkel. TCR triggering by pMHC ligands tethered on surfaces via poly (ethylene glycol) depends on polymer length. *PLoS One*, 9(11):e112292, 2014.

[251] W-S Chang, JW Ha, LS Slaughter, and S Link. Plasmonic nanorod absorbers as orientation sensors. *Proc. Natl. Acad. Sci. U.S.A.*, 107(7):2781, 2010.

[252] H Chen, L Shao, T Ming, KC Woo, YC Man, J Wang, and H-Q Lin. Observation of the Fano resonance in gold nanorods supported on high-dielectric-constant substrates. *ACS Nano*, 5(8):6754–6763, 2011.

[253] E Schäffer, SF Nørrelykke, and J Howard. Surface forces and drag coefficients of microspheres near a plane surface measured with optical tweezers. *Langmuir*, 23(7):3654–3665, 2007.

[254] F Strauss. Experiment performed during a practical. Data not evaluated or used previously, University of Tübingen, March 2019.

[255] P Siqueira, Denise F, G Wenz, P Schunk, and T Schimmel. An improved method for the assembly of amino-terminated monolayers on SiO_2 and the vapor deposition of gold layers. *Langmuir*, 15(13):4520–4523, 1999.

[256] H Ma, PM Bendix, and LB Oddershede. Large-scale orientation dependent heating from a single irradiated gold nanorod. *Nano Lett.*, 12(8):3954–3960, 2012.

[257] T Korten and S Diez. Setting up roadblocks for kinesin-1: mechanism for the selective speed control of cargo carrying microtubules. *Lab Chip*, 8(9):1441–1447, 2008.

[258] IA Telley, P Bieling, and T Surrey. Obstacles on the microtubule reduce the processivity of kinesin-1 in a minimal in vitro system and in cell extract. *Biophys. J.*, 96(8):3341–3353, 2009.

[259] M Bugiel and E Schäffer. Three-dimensional optical tweezers tracking resolves random sideward steps of the kinesin-8 Kip3. *Biophys. J.*, 115(10):1993–2002, 2018.

Acknowledgements

First, I want to thank Erik Schäffer for the position in his group, the supervision and thoughts he invested in my projects. Second, I want to thank Anita Jannasch, a driving force in the lab, for being always supportive and there in any case of need. Also I want to thank Anita Jannasch and Sebastian Kenzler for proofreading and Erik Schäffer and Monika Fleischer for correcting and assessing the quality of this thesis. Additionally, I want to thank Hauke Drechsler for providing feedback on many figures. I want to thank Swathi Sudhakar, for introducing the gold nanorods synthesis Also I want to thank Maria Kharlamova and Michael Bugiel for being great collegues also always very helpful. Furthermore, I want to thank Gero Hermsdorf for being always helpful concerning questions of his setup or similar issues. Mohammad Kazem Abdosamadi I want to thank for his help in setup, Fiji tools or lab related questions. Also I want to thank Benedikt Fischer, Mayank Chugh, Shu Yao Leong and Anita Jannasch for their work on purifying the proteins we commonly use in the lab and the last setup-builders I got to know, Gero Hermsdorf and Steve Simmert for developing the microscopes and tweezers. Furthermore, I want to thank Prof. Schnepf for the availability to use the zeta sizer and Sebastian Kenzler and Tanja Kunz for their help concerning questions in their lab. Furthermore, I want to thank the LISA+ instrument scientists for their support and advice concerning the LISA+ instruments and facility. Also I want to thank Prof. Vollmer for offering the possibility to perform whispering-gallery modes in his lab in Exeter and Narima Eerquing for investing time into the measurements. Next I want to thank Prof. Peisert for the possibility to measure XPS spectra in his group and giving advice and Dustin Quinones for performing the measurements and helping with the data analysis. Finally, I want to thank all the pratical, bachelor and master students and Hiwis working on projects adressed and not addressed in this thesis. Aylin Kayacik and Fabian Strauß I want to thank for participating on the gold nanorod project. Anusha Hiremath and Pasupathi Rajendran I want to thank for working on other projects such as the silicon and germanium particles. Christoph Kerzscher, Leonard Simeonov, and Tobias Krauss I want to thank for great work on the thermophoresis project. Aylin Kayacik, Sandro Münch and Tom Stumpp I want to thank for working on the Skadi setup used for iSCAT imaging.